IADC-13-11
September 2018

Inter-Agency Space Debris Coordination Committee

Spacecraft Component Vulnerability for Space Debris Impact

Issued by IADC Working Group 3

Action Item 31.3

Table of Contents

Revision History

Issue	Revision	Date	Reason for Revision
0	1	15 May 2014	Issue of doc. v0.1 during WG Session 3.1&3.2&4.1 of IADC32
0	2	01 Apr 2015	Template modification
0	3	05 Aug 2017	Chap. 2 (Akahoshi), Chap. 3 (Christiansen, Schäfer) Chap. 4 (Christiansen), Chap. 5 (Schäfer) Chap. 8 (Christiansen), Chap. 9 (Pang) Chap. 10 (Christiansen)
0	4	10 Jul 2017	Chap. 6 (Higashide), Chap. 8 (Higashide)
0	5	08 Aug 2017	Chap. 1 (Francesconi), Scope (Higashide) Distribute for WG3 reviewing
0	6	31 Aug 2017	Chap. 6 (Nikanpour)
0	7	11 Sep 2017	Chap. 1, 8, 10,11 (Schäfer) Format revision (Higashide)
1	0	17 Nov 2017	Title change, Minor corrections Submitted to SG

List of Authors

Chapter	Author	Affiliation
1 Risk Assessment for Spacecraft	F. Schäfer	Fraunhofer EMI
2 Solar Array	Y. Akahoshi	KIT
3 Cables	E. Christiansen	NASA
	F. Lyons	NASA
	J. E. Miller	NASA
	J. Read	NASA
	F. Schäfer	Fraunhofer EMI
4 Battery	E. Christiansen	NASA
	J. E. Miller	NASA
5 Electronic Box	F. Schäfer	Fraunhofer EMI
6 Structure / Effect of Material Degradation	M. Higashide	JAXA
	D. Nikanpour	CSA
	I. Telichev	Univ. Manitoba
7 MLI	E. Christiansen	NASA
	M. Higashide	JAXA
	J. E. Miller	NASA
8 Pressure Vessel	B. Pang	HIT
	F. Schäfer	Fraunhofer EMI
9 Transparent Materials	E. Christiansen	NASA
10 Fluid Line	F. Schäfer	Fraunhofer EMI
11 Examples of Risk Assessment Method	A. Francesconi	Univ. Padova
	F. Schäfer	Fraunhofer EMI

List of Affiliations

Affiliation	Description
CSA	Canadian Space Agency
Fraunhofer EMI	Fraunhofer Institute for High-Speed Dynamics, Ernst-Mach-Institut, Germany
HIT	Harbin Institute of Technology, China
JAXA	Japan Aerospace Exploration Agency
KIT	Kyushu Institute of Technology, Japan
NASA	National Aeronautics and Space Administration
Univ. Manitoba	University of Manitoba, Canada
Univ. Padova	University of Padova, Italy

Scope

This document is a specific report about spacecraft component vulnerability. To understand space debris and micro meteoroid impact risks of spacecraft, it is necessary to know impact conditions which cause component failures. The aim of this report is to summarize knowledges about spacecraft component vulnerability against debris impacts that have been investigated by IADC Working Group 3 (Protection) members.

To know spacecraft vulnerability, following properties are important: 1) shielding effect of structure, 2) vulnerability of equipments, 3) failure mode of components. This document shows those for each typical components. Since this report shows only outline of research results, references of each chapter are useful to help understanding details.

1 Risk Assessment for Spacecraft

Micrometeoroid and space debris impacts may reduce the reliability and functionality of spacecraft components. Impacts may impair the successful completion of a mission. Hence the vulnerabilities of spacecraft to impacts from meteoroid and space debris particles have to be understood and the associated risks for spacecraft need to be analyzed for each mission.

From the early years of space exploration, spacecraft designers have used probabilistic approaches to assess the risks from impacts to missions and used this information to design for impact protection [1-1]. These works were driven by the need to protect crewed missions. Micrometeoroid and space debris protection for human exploration spacecraft is designed to reduce the damage that would endanger the survivability of the crew. Requirements are met when the micrometeoroid and space debris protection system and operational techniques for the spacecraft meet or exceed the required minimum acceptable risk for loss-of-mission and/or loss-of-crew. For crewed missions, spacecraft flight rules have been implemented to operate in orientations that reduce impact risks to the maximum extent possible. Some programs have a requirement to monitor the effects of impacts with on-board sensors. Other spacecraft programs, particularly atmospheric return vehicles, have requirements to detect damage to particularly sensitive or high-risk areas of the vehicles for micrometeoroid and space debris damage, and, in the case of crewed vehicles, to carry repair kits to provide a means to patch critical impact damages to thermal protection system materials and/or pressure shell.

For satellite missions, requirements with regards to particle impacts are less demanding, since no crews are involved. Risk assessment is performed as part of the reliability analysis, to understand the probability of failure of spacecraft components and their effect on the overall mission success.

In order to understand the threats and effects of particle impacts on spacecraft, environmental debris models and micrometeoroid flux models have been developed. These provide particle flux information such as size, impact direction and relative impact velocity with respect to a spacecraft surface.

A specific class of damage equations, Ballistic Limit Equations (BLEs), have been developed exploiting the results from impact tests and numerical simulations with hydrocodes to predict the particle sizes causing failure of structure walls and spacecraft components as a function of impact speed, impact angle, particle density and target parameters (thickness, materials of construction, etc.).

By combining flux data, damage equations and spacecraft geometry, risk assessment of the spacecraft can be performed. This methodology is sketched in Fig. 2.1-1. Risk assessment can be used to identify zones and areas of the spacecraft that are the “risk drivers” that control the impact risk. Options can be evaluated to reduce risk and meet micrometeoroid and space debris protection requirements. The effect of using debris shields to reduce the risk of failure can be analyzed as well as component redundancy principles as a means of passive protection of the spacecraft.

Risk analysis tools and codes apply the above-mentioned debris environment models and the damage equations in order to estimate satellite structure penetration rates. Some codes use algorithms that are suitable to compute the damage to components behind the spacecraft structure wall. These codes are capable to assess the consequences of space debris and meteoroid impacts with a high accuracy, allowing to identify the weak points of a spacecraft design with great detail.

The output of the codes is a quantification of the overall mission risk from impacts. Suitable risk figures are, for example:

- the overall probability of failure (PF), or
- the probability of no penetration (PNP), or
- the reliability.

In this document, a few risk assessment tools are described. For more information on risk assessment, refer to the Protection Manual [1-2].

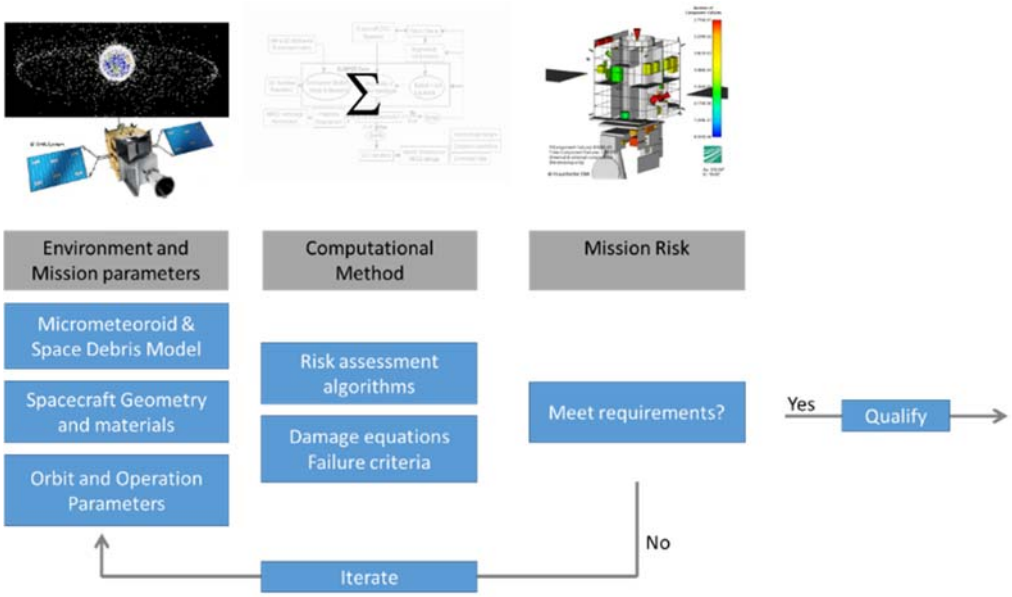

Fig. 2.1-1 Generic risk assessment methodology

A core element of risk assessment codes is the methodology for performing the damage assessment. There are different ways to perform damage assessments; some codes rely on using BLE's, others use analytical equations. All methods have in common that they are based on laboratory experiments or at least are calibrated using laboratory experiments. Besides the damages equations, the failure modes of the corresponding component have to be known in view of defining the failure criteria within the risk assessment codes. These failure modes and the corresponding threshold criteria are also defined in laboratory experiments. A few examples:

- Pressure tanks can merely leak or catastrophically burst after an impact. In both cases the tanks lose their function i.e. lose pressure. The threshold impact conditions for achieving these two different failure types are different, and they depend also on the tank's overpressure with regards to the ambient pressure. In the case of leakage caused by a small hole, the mission may lose redundancy but still may compete its mission goals. In the case of a rupture, most likely the mission will be terminated immediately. Depending on the type of risk assessment to be performed, one or another failure mode will be selected.
- In crewed modules, penetrations into the pressurized modules will lead to a depress event, as well as internal effects such as high-speed fragment release into the interior

of the crew modules, light-flash, heat and possibility of fire and release of gases/liquids depending on the internal equipment that is damaged.

- Cables can experience different types of failures. Experimentally the following modes have been observed: temporary failure (e. g., voltage spikes or temporary shorts), permanent failure (e. g., from severing or arching). The experimentally observed threshold impact conditions for both failure types are quite different.

Hence, it is of crucial importance for risk assessment to know the impact conditions which cause component failures. This report summarizes knowledges about spacecraft component vulnerability against debris impacts that have been investigated by IADC Working Group 3 (Protection) members in laboratory experiments. Each component has different damage thresholds and failure modes, which are reported. Still, this report can only compile the outlines of research results. For more details, please refer to the references listed at the end of each chapter.

[1-1] NASA SP-8042 (1970), Meteoroid Damage Assessment, Space Vehicle Design Criteria (Structures), May 1970.

[1-2] Protection Manual v7

2 Solar Array

2.1 Damage Mode

In recent years, a solar array of a spacecraft has become larger with the voltage higher because a spacecraft needs a large amount of power in requests from an advanced mission. Therefore the risk of a space debris impact and discharge on the solar array is increasing because the number of small space debris such as ejecta is increasing [2-1]. Space debris impact to the solar array causes not only mechanical damage such as destruction of a solar cell and insulation layer but also electrical damage due to local high density plasma induced by impact energy [2-2]. This plasma can lead to arcing between solar cells or cell and substrate on the solar array [2-3]. In the worst case, Joule heating of arcing can carbonize insulation layer and create permanent short-circuit path [2-4]. This phenomena is called “Permanent Sustained Arc“ (PSA).

2.2 Impact Experiments and Numerical Simulations / KIT

2.2.1 Summary of Conditions and Results

Dicharge experiments due to hypervelocity impact have been done since 2005 in Kyushu Institute of Technology. The typical experimental configuration of hypervelocity impact tests is shown in Fig. 2.2-1, where the two-stage light gas gun installed at Laboratory of Spacecraft Environmental Interaction Engineering (La SEINE) in Kyushu Institute of Technology was used. The projectile was Al2017 sphere which was 3 mm in diameter. The ambient pressure in the test chamber is 4×10^{-2} Pa. Solar array coupon composed of silicon cell is shown in Fig. 2.2-2, where cell and coverglass are 100 um in thickness, and the substrate is made of CFRP Al honeycomb sandwich. Solar array coupon can simulate the condition of power generation with connection to the external circuit as shown in Fig. 2.2-3. The external circuit consisted of quick response constant current (CC) power supply, resistor and constant voltage (CV) power supply [2-5]. The resistor simulates load resistance of a spacecraft. The output of CC power supply simulates that of a string of solar array. The CV power supply simulates the voltage which is maintained by the other strings of solar array when discharge occurs on the string. The voltage of the CV power supply was set 1 V lower than that of CC power supply. CRD power supply composed of constant current regulation diodes and voltage source was used as quick response CC power supply [2-6]. The current probe 1 (Cp1) measured current of circuit which simulate the output of a string of the solar array. The current probe 2 (Cp2) measured current which flow to resistance. The current probe 3 (Cp3) measured discharge current between the cell and substrate. The voltage probe measured string voltage. Triple probe [2-7] was set at a distance of 100 mm from the front of the solar array coupon to measure electron temperature and density of plasma created by hypervelocity impact. The configuration of the triple probe is shown in Fig. 2.2-4. The probe was made of coated copper wire. The diameter and exposed length oft he probe were 2 mm and 20 mm, respectively, where the near part of the tip of the probe was insulated by Kapton tape. The electron temperature T_e [eV] and density N_e [m^{-3}] can be calculated by V_2, V_3 and the following equations. The electron temperature is obtained from Eqs. 2.2-1 and 2.2-2.

$$\frac{I_1 + I_2}{I_1 + I_3} = \frac{1 - \exp(-\phi_{d2})}{1 - \exp(-\phi_{d3})} \tag{2.2-1}$$

$$I_1 = I_2 + I_3 \tag{2.2-2}$$

where $\phi_{d2} = eV_{d2}/\kappa T_e$, $\phi_{d3} = eV_{d3}/\kappa T_e$, e is elementary electric charge and κ is Boltzmann constant. Finally, electron density can be calculated by following equations.

$$I_1 = \frac{I_3 - I_2 \exp(-\phi_{\Delta V})}{1 - \exp(-\phi_{\Delta V})} \tag{2.2-3}$$

$$N_e = \left[(M)^{1/2} / S\right] I_i f_1(\phi_{d2}) \tag{2.2-4}$$

$$f_1(\phi_{d2}) = 1.05 \times 10^{15} (T_e)^{-1/2} \left[\exp(\phi_{d2}) - 1\right]^{-1} \tag{2.2-5}$$

Here M [g] is ion mass, S [mm^2] is surface area of the probe and I_i [μA] is ion current. In this study, V_{d2} = 3 [V], V_{d3} = 18 [V] and the resistance was 0.25-10 [k].

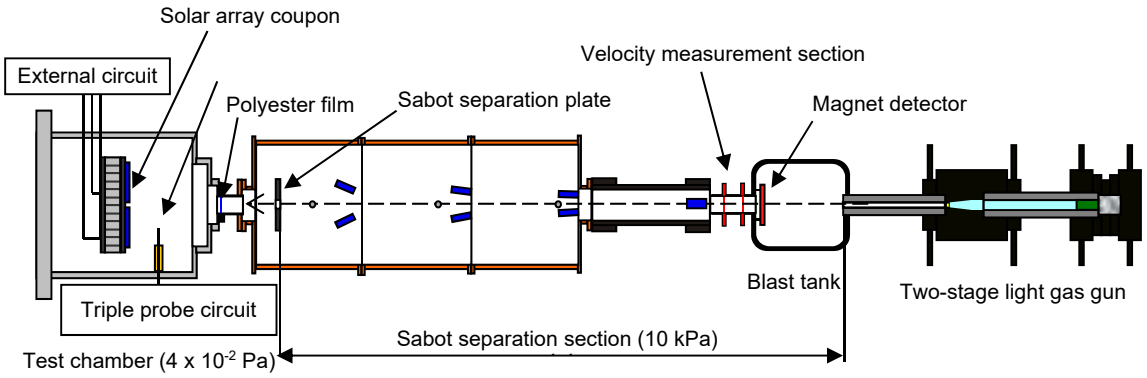

Fig. 2.2-1 Experimental setup of hypervelocity impact test

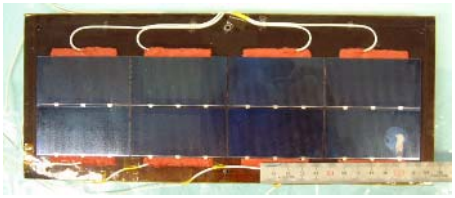

(a) Front view

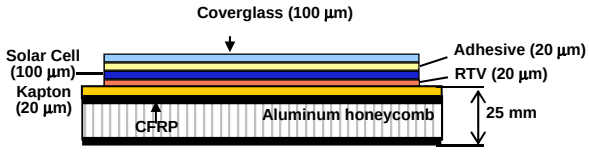

(b) Cross section

Fig. 2.2-2 Solar array coupon

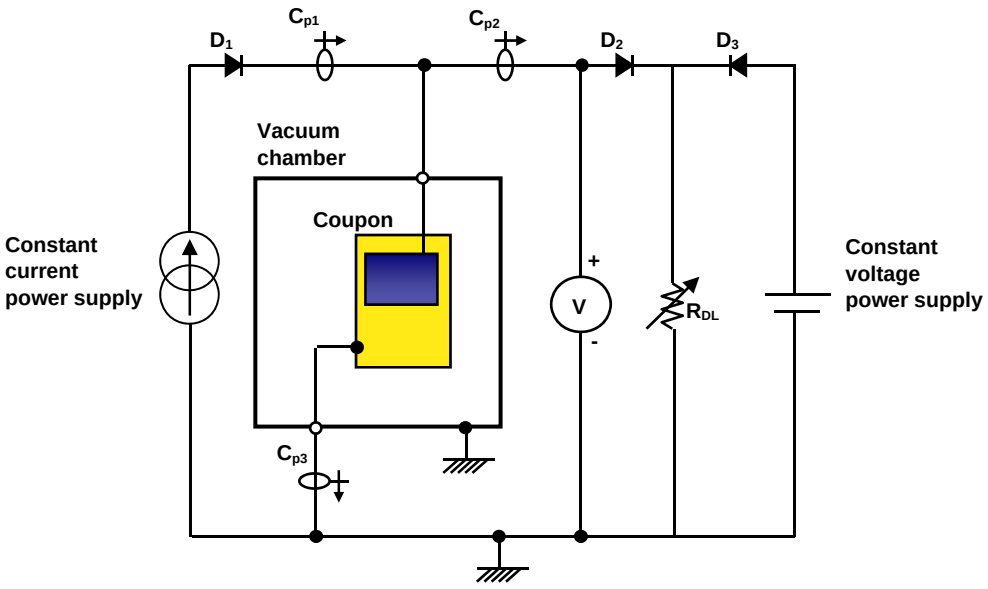

Fig. 2.2-3 External circuit

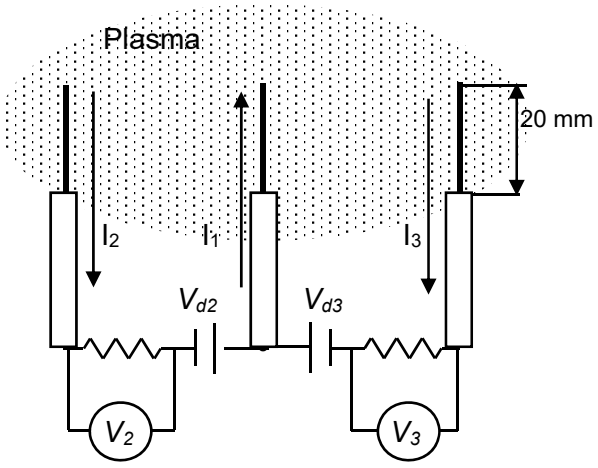

Fig. 2.2-4 Triple probe circuit

2.2.2 Details

Hypervelocity impact tests were conducted in the impact velocity of mainly approximately 4 km/s and several different velocities. The measurement results of electron density and temperature of plasma created by impact depend on measurement point and time because the plasma diffuses from impact point. Therefore, the solution of the advection-diffusion equation was defined as fitting curve to time history of electron density at the measurement point on the assumption that plasma diffusion can be represented by that solution, which is following formula.

$$N_e = \frac{n_e}{(4\pi Dt)^{3/2}} \exp\left[-\frac{(r-Ut)^2}{4Dt}\right] \qquad (2.2\text{-}6)$$

where t is elapsed time since impact, N_e is electron density, and r is distance from impact point to measurement point of the triple probe. The fitting parameters, which are electron number n_e diffusion coefficient D and advection velocity U can be obtained by the curve fitting. The example of measurement results of electron density with the fitting curve and electron temperature are shown in Fig. 2.2-5, respectively. The time at the drop of the string voltage on the external circuit due to short-circuit between the cell and substrate in the penetration process of the Al sphere into the solar array coupon was set to 0 s. In this example, n_e = 1.80x10^{15} electrons, D = 64.7 m^2/s, and U = 5.81 km/s were obtained by the curve fitting. The electron temperature at the time when the electron density is maximum value on the fitting curve is adopted as representative value because diffusion into vacuum is isothermal expansion. In this example, electron temperature was 1.7 eV at time of 13.7 usec after impact when the electron density was maximum value of 1.22x10^{17} m^{-3}. These values of electron temperature and density were higher than plasma environment in low earth orbit, which were 0.09 eV and 1x10^{11} m^{-3}, respectively [2-8]. Test results about discharge are distinguished by the following definitions. Primary arc (PA) is discharge just after impact. Temporary Sustained Arc (TSA) is discharge that discharge current measured by Cp3 equals to circuit current measured by Cp1 for over 2 usec. Permanent Sustained Arc (PSA) is that there is permanent short-circuit path after hypervelocity impact test.

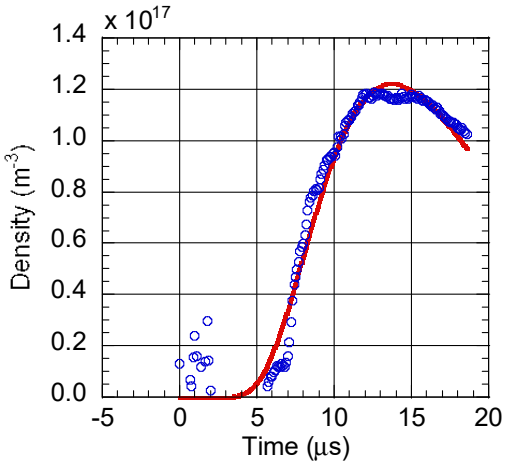

Fig. 2.2-5 Electron density

The test results are shown in Table 2.2-1. The results of discharge which are arranged on voltage and current condition of external circuit are shown in Fig. 2.2-6. The results of a longer duration of discharge are shown in Fig. 2.2-6, where there are various results in the same condition of voltage and current setting. In the case that impact velocity was around 4 km/s, PSA occurred under the conditions that voltage was 182 V and current was 2.4 A and more. In the other impact velocity, although there were few tests conditions of voltage and current, PSA occurred under 133 V & 4.8 A and 182 V & 4.8 A with the impact velocity of about 2.1 km/s and under 182 V & 4.8 A with the impact velocity of around 4.7 km/s. These results confirm hypervelocity impact causes PSA on a solar array.

Table 2.2-1 Discharge Results due to Hypervelocity Impact Test

Voltage (V)	Current (A)	Impact Velocity (km/s)	Discharge	Electron Number (10^{13} electrons)	Electron Temperature (eV)	Diffusion Coefficient (m^2/s)	Advection Velocity (km/s)
84	2.4	3.78	PA	180	1.74	64.7	5.81
	3.6	3.68	TSA	45.4	2.63	15.9	4.14
	4.8	3.52	PA	163	1.77	54.1	4.74
133	3.6	3.72	TSA	194	1.71	53.9	5.50
		4.02	TSA	295	2.07	58.3	4.52
	4.8	2.08	PSA	3.74	1.04	6.18	2.12
		2.85	PA	30.8	1.06	27.2	3.63
		3.74	TSA	350	1.85	74.2	4.14
		3.85	TSA	154	1.46	57.8	5.52
		4.82	PA	892	2.86	104	6.14
182	1.2	3.95	PA	259	2.10	54.7	5.46
	2.4	3.81	PSA	129	1.50	42.3	5.78
	3.6	3.74	PSA	185	2.37	39.0	4.55
	4.8	2.14	PSA	3.08	1.37	5.15	1.95
		3.76	PSA	233	1.76	51.3	5.72
		4.65	PSA	643	2.93	95.3	6.23

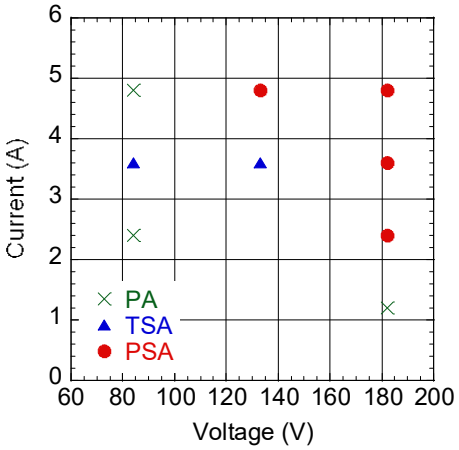

Fig. 2.2-6 Test results about discharge

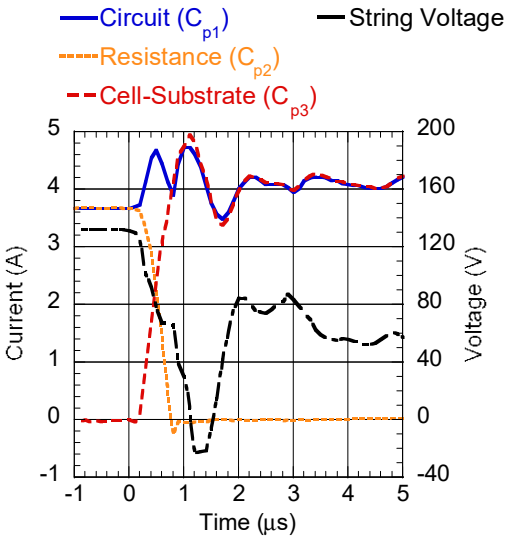

Fig. 2.2-7 Current and voltage of onset of arcing

The typical example of the voltage and current waveforms of the external circuit is shown in Fig. 2.2-7. Applied voltage and current were 133 V and 3.6 A, respectively, and impact velocity was 4.02 km/s. It took the circumference of largest dimension of the Al sphere approximately 0.4 usec to pass through the cell. The plasma created by hypervelocity impact sustained discharge between the cell and substrate after the perforation. Collision of ions into substrate, which is cathode, generates neutral gas and secondary electrons while plasma diffuses. Thermionic emission occurs due to local temperature rise of the substrate caused by ion collision depending on conditions. The electrons generated by those processes ionize the neutral gas and the arcing can be sustained by the new ions and electrons after diffusion of plasma created by impact. If the arcing stops before insulation layer is carbonized by Joule heating, this arcing is TSA, if not, PSA occurs. Therefore, ion current density which is collected by the substrate at the impact point plays a vital role in the occurrence of sustained

arc. This ion current density can be calculated by Eqs. 2.2-6 and 2.2-7 using the number of electrons, electron temperature, diffusion coefficient and advection velocity, which were shown in Table 2.2-1.

$$i_i = \exp\left(\frac{1}{2}\right) eN_e \sqrt{\frac{\kappa Te}{m_i}} \tag{2.2-7}$$

Here i_i is ion current density and m_i is ion mass. The calculation results at 1 ns after impact are plotted on Fig. 2.2-8 as a function of impact velocity. These results can be fitted by power law with index of 2.0, which is shown following.

$$i_i = (6.7 \times 10^6) \times v^{2.0} \tag{2.2-8}$$

where v is impact velocity. Therefore, the ion current density is proportional to kinetic energy of the projectile. In the tests, the impact velocities were low in comparison with that of debris in low earth orbit, which is 10 km/s on an average. However, because the ion current density which is collected by the substrate at the impact point is proportional to kinetic energy, it is considered that higher velocity impact can trigger PSA.

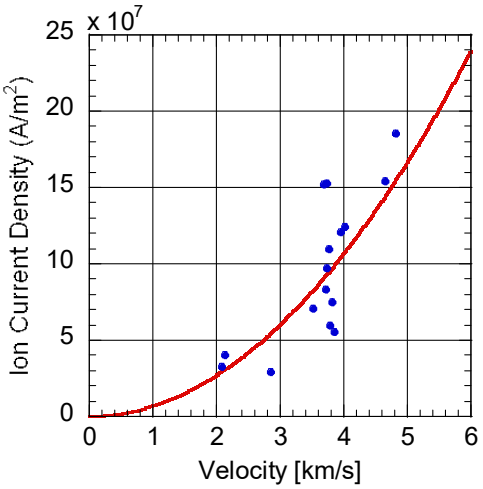

Fig. 2.2-8 Ion current density at impact point

In this section, hypervelocity impact tests using comparatively large size projectile which was 3 mm Al sphere were conducted to evaluate possibility of PSA due to the plasma created by debris impact. As a result, it was concluded that hypervelocity impact can lead to PSA on a solar array. The plasma created by hypervelocity impact was measured by triple probe and the electron number, electron temperature, diffusion coefficient and advection velocity were obtained using the solution of the advection-diffusion equation. The ion current density which is collected by the substrate at the impact point can be calculated from these parameters. The calculation results shows that the ion current density is proportional to kinetic energy of projectile.

2.3 Recommendation for MMOD risk reduction

In order to reduce MMOD risk, the number of small debris should be reduced. It is important that the current situation of small debris distribution is measured using new impact sensors which are proposed by JAXA & IHI or NASA. Most of contribution to small debris

could be thought to be ejecta. So then a selection of surface material should be discussed in order to reduce ejecta.

2.4 References

[2-1] FUKUSHIGE Shinya, AKAHOSHI Yasuhiro, KITAZAWA Yukihito, GOKA Tateo, “Comparison of Debris Environment Models; ORDEM2000, MASTER2001 and MASTER2005”, IHI ENGINEERING REVIEW, VOL.40, No.1 February 2007, pp. 31-41.

[2-2] Gerhard Drolshagen, “Hypervelocity Impact Effects on Spacecraft”, Proceedings of the Meteoroids 2001 Conference, ESA Publication Division, 2001, pp. 533–544.

[2-3] S. Fukushige, Y. Akahoshi, K. Watanabe, T. Harano, Y. Machida, N. Furusawa, T. Koura, S. Hosoda, M. Cho, and S. Harada, “Hypervelocity Impact Test to Solar Array for Evaluation of Possibility of Sustained Arc”, Proceedings of the 25th International Symposium on Space Technology and Science, 2006, pp. 1356–1361.

[2-4] I. Katz, “Mechanism for Spacecraft Charging Initiated Destruction of Solar Arrays in GEO”, AIAA, 36th Aerospace Science Meeting, Reno, 1998, pp. 98-1002.

[2-5] D. Payan, D. Schwander and J.P. Catani, “Risks of low voltage arcs sustained by the photovoltaic power of a satellite solar array during an electrostatic discharge. Solar Array Dynamic Simulator”, 7th Spacecraft Charging Technology Conference, 2001.

[2-6] Kazuhiro Toyoda, Seiji Aso, Tokuro Kyoku, Tomoki Kitamura, and Mengu Cho, “Proposal of a Current Regulative Diode for Power Supply in Sustained Arc Test”, 9th Spacecraft Charging Technology Conference, ISSN 1349-113X, JAXA-SP-05-001E, August 2005, pp. 123-131.

[2-7] S. Chen and T. Sekiguchi, “Instantaneous Direct- Display System of Plasma Parameters by Means of Triple Probe”, Journal of Applied Physics, August 1965, pp. 2363–2375.

[2-8] Alan C. Tribble, “The Space Environment Implications for Spacecraft Design”, Princeton University Press, 1995, p.114.

3 Cables

3.1 Damage Mode

Laboratory tests suggest that cables have to be mechanically damaged to show signs of failure. Failure is understood as temporary or permanent disruption of data transmission or power supply with the cables involved.

1) In cases when no damage to the cable insulation or just dust deposits on the cables were observed, the cables performed without performance degradation. Signal distortion less than 1 % of the nominal signal value is judged as no failure.
2) In case of one or more craters in the insulation that were energetic enough to penetrate the insulation layer and reach the cable conductor, the signal transmission was impaired, e. g. temporarily disrupted. This failure mode includes damages such as insulation partial removing from the cable, i.e., the conductor was visible. A power cable transmission error was assumed if the signal rose or dropped above or below 20 % of its nominal value with at least a 1 µs duration. A data cable transmission error was assumed if a data transmission error was encountered with at least a 1 µs duration. An RF cable transmission error was assumed if the signal rose or dropped above or below 20 % of its nominal value with at least 10 µs duration.
3) When cables were partially or completely severed, the cable was no longer functional (i.e. not capable of performing its assigned task) due to either a short circuit or a destroyed (=severed) conductor. This mode causes permanent failure.

3.2 Impact Experiments and Numerical Simulations / EMI

At ESTEC, the data transmission degradation within electrical harness from hypervelocity impacts on harnesses was studied.

Electrical harnesses can claim large areas of the interior surface of satellite structure walls.

The total weight of the harnesses can amount to several percent of the overall spacecraft weight. Harnesses are vulnerable because only thin insulation layers protect the wires. Furthermore, harnesses are often located just behind the satellite structure walls. An impacting particle that penetrates the spacecraft structure is shattered into many small fragments that are dispersed over a large area. These fragments may hit and damage electrical harnesses.

The harness tested in [3-1][3-2] consisted of power cables, Raychem Spec 44, 18 AWG, twisted-pair data cables, Raychem Spec 44, 20 AWG, and one radiofrequency (RF) cable specification Sucoflex 103 from Huber & Suhner, transmitting a 9.35 GHz signal. The cables were bound together and routed in loops to increase the probability of fragment impact on the cables, as shown in Fig. 3.2-1. They were spaced approx. 10 mm from a 1.5 mm thick Al 7075 witness plate.

The harness was placed at a stand-off S_1 of 10 and 100 mm behind an aluminum honeycomb sandwich panel with multi-layer insulation. The sandwich panel consisted of 0.41 mm thick Al 2024 T3 face-sheets and a 35 mm thick Al honeycomb core (specification 2.0-3/16-07P-5056-MIL-C-7438G). Multi-Layer-Insulation (MLI) with an areal density of 0.447 kg/m^2 was placed on top of the sandwich panel (i.e., space-facing).

Each of the three power cable pairs was connected to a 30 VDC power supply on one side and a 200 Ω resistor on the other side (simulating the electrical load). Voltage drop at both the power supply and the resistor was measured individually for all cable pairs. For the data cables a pseudo-random bit stream was generated, and differential data transmission technique was used. For power and data cables, the nominal input voltage and the output voltage were monitored to quantify the impact effect.

The RF cable was connected to a 9.35 GHz oscillator with a power output of approx. + 20 dBm on one side and a crystal detector on the other side. The voltage drop at the crystal detector provides a means of detection of the degradation of the RF cable.

Table 3.2-1 summarizes a series of experiments published in [3-2]. S1 – stand-off between rear side of structure wall and cable, v0 – impact velocity, dP – projectile diameter, Mech. – mechanical damage ('none' = no damage to cable insulation, dust deposits possible; 'craters' = one or more craters in insulation (insulation may or may not be perforated); 'insul.' = insulation partially removed from cable (the conductor is visible); 'severed' = cable (partially) severed with at least one conductor completely cut.), Electr. - electrical performance ('none' = signal distortion less than 1 % of nominal value; 'dist'd' = signal distortion, but no transmission error; 'error' =signal transmission error encountered, but no degradation; 'e.+deg.' = signal transmission error encountered and cable degraded; 'failure' = cable no longer working due to either a short circuit or a destroyed conductor. A power cable transmission error was assumed if the signal rose or dropped above or below 20 % of its nominal value with at least a 1 µs duration. A data cable transmission error was assumed if a data transmission error was encountered with at least a 1 µs duration. An RF cable transmission error was assumed if the signal rose or dropped above or below 20 % of its nominal value with at least 10 µs duration.)

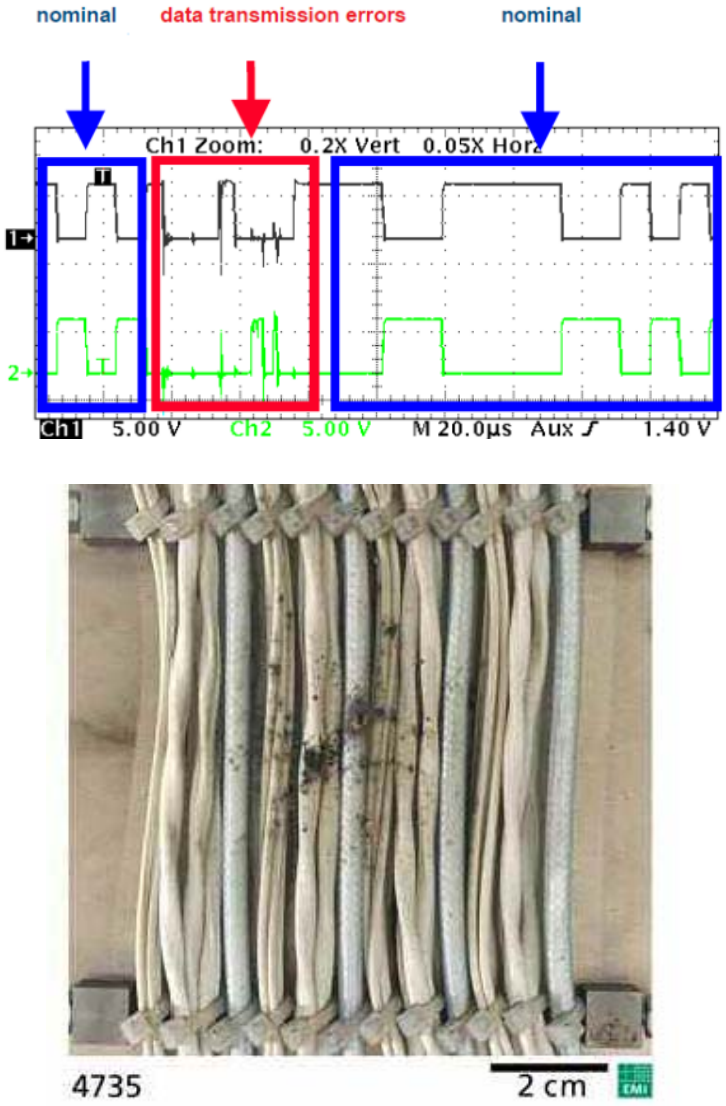

Fig. 3.2-1 Impact test on operating harness placed behind satellite structure wall (H/C SP = Honeycomb Sandwich panel). Top: Differential signal recorded during impact. "T" denotes the projectile impact on the honeycomb sandwich panel. Bottom: Impact damages on harness [3-2].

Table 3.2-1 Summary of HVI experiments on harness and results (aluminium projectiles, perpendicular impact)

Exp.	S_1	v_0	d_P	Power Cables		Data Cables		RF Cable	
	(mm)	(km/s)	(mm)	Mech.	Electr.	Mech.	Electr.	Mech.	Electr.
4728	10	6.42	2.0	none	None	none	none	craters	none
4732	10	6.55	2.5	insul.	dist'd	severed	failure	craters	dist'd
4731	100	6.53	2.5	insul.	Error	craters	error	craters	dist'd
4727	100	6.77	3.0	insul.	dist'd	insul.	failure	craters	dist'd
4736	100	6.78	4.0	insul.	Error	insul.	failure	insul.	e.+deg.
4738	100	7.70	2.0	none	None	craters	none	craters	none
4734	100	7.59	2.5	craters	None	insul.	error	craters	dist'd
4733	100	7.68	3.0	insul.	error	craters	dist'd	insul.	error

Fig. 3.2-1 shows an example of the recorded data during an impact test on a data cable transmitting data using the differential transmission method. Up to several tens of microseconds after the impact, temporary data transmission errors are observable, followed by nominal operation of the cables afterwards. More severe impact damages up to permanent failure of the cable (e.g. from severing or short-circuit) are obtained when larger or faster projectiles are used. It was found that increasing the stand-off distance between structure wall and harness reduces the probability of cable failure. Therefore, harnesses should be moved away from structure walls or alternatively, protective fabrics such as Nextel™[1] or Kevlar™, should be wrapped around the harness, as was done by NASA for ISS harnesses routed outside the manned modules.

3.3 Impact Experiments and Numerical Simulations / NASA

3.3.1 Summary of Conditions and Results

With kilometers of wire cable runs on the exterior of the International Space Station (ISS), assessing and reducing failure of cables due to micrometeoroid and orbit debris (MMOD) impact has been a focus for ISS mission support. Two failure mechanisms for cables have been identified: open circuits due to severing the conductors within the cable, and short circuits due to connection between hot and return conductors, or between the conductors and grounded components such as ground shields within the cable itself or with grounded structure that the cable is attached to. While there are many types of cables, the cable configurations that have been evaluated to the greatest extent by personnel in the NASA Johnson Space Center (JSC) Hypervelocity Impact Technology (HVIT) group are primary and secondary power cables, and coaxial cables and twisted pair cables that typically carry data.

Hypervelocity impact tests supported the HVIT risk assessments for these cables. These tests were performed with aluminum and steel spherical projectiles accelerated to 7-8 km/s by the two-stage light-gas gun launchers at the Remote Hypervelocity Test Laboratory at NASA White Sands Test Facility (WSTF).

3.3.2 Details

3.3.2.1 Impact Experiments

Twenty-five (25) impact tests were performed on the ISS primary power supply cables, 12 into a coaxial cable assembly and 97 into ISS twisted-pair data handling cables. Representative test articles are shown in Fig. 3.3-1.

[1] Nextel is a trademark of 3M Company, and Kevlar is a trademark of E. I. du Pont de Nemours and Company.

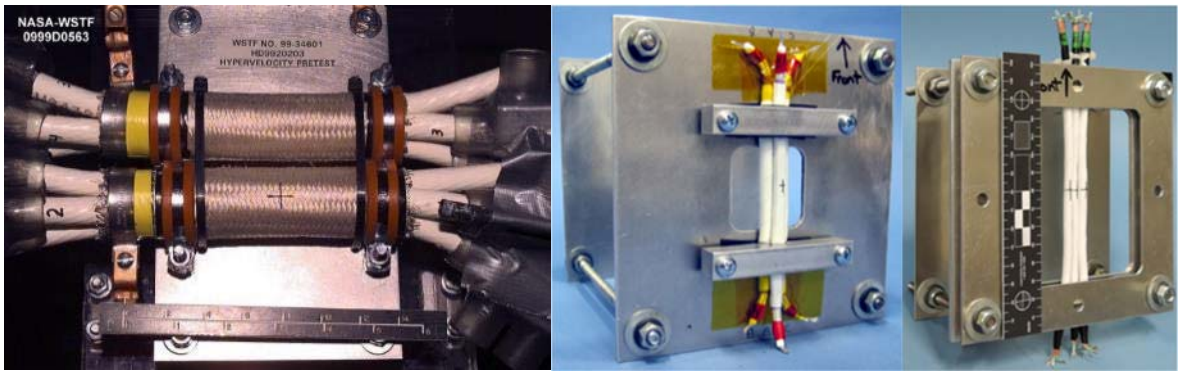

Fig. 3.3-1 ISS power supply cable (left), the co-axial cable (center) and the twisted pair data handling cable (right) experimental articles

The ISS primary power supply cables are composed of 2 pairs of copper 0 AWG conductors (positive and return; i.e., 4 conductors per cable) with filler cord in the gaps between the conductors. Each conductor is insulated with a 1 mm thick layer of Teflon. The conductors and filler cords are wrapped with a conducting braided wire mesh which provides MMOD protection as well as serving as a co-axial grounded layer. The entire assembly is wrapped in a braided glass cloth and is approximately 5 cm in diameter as shown schematically in Fig. 3.3-2. Tests with these cables were performed energized (with operationally rated current and voltage levels) and non-energized. With energized cable tests, electronic circuitry was included to emulate electronics on ISS that protect downstream equipment from power surges. This was done to make the testing as realistic as possible and to evaluate the destructive potential of discharge arcs if they occurred during the tests.

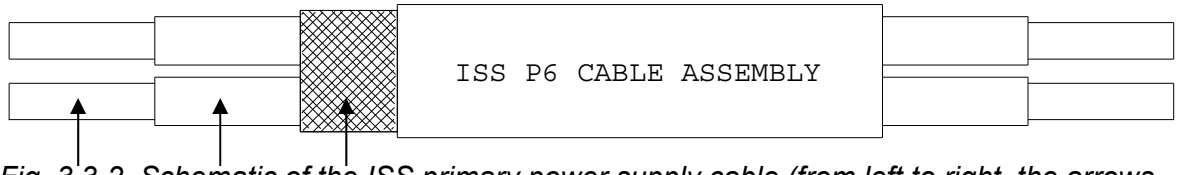

Fig. 3.3-2 Schematic of the ISS primary power supply cable (from left to right, the arrows point to the conductor, insulation and stainless steel overbraid)

The ISS co-axial cable surrogate used in the tests is a commercial Cobham FA19X coaxial cable shown schematically in Fig. 3.3-3. The cable has an outer diameter of 4.8 mm with a perfluoroalkoxy alkane (PFA) Teflon jacket and wrapped with 0.029 g/cm2 beta-cloth. The beta-cloth is spirally wrapped with an overlap of 50%, 67% and 75% (two-, three- or four-layer) around each individual cable (different overwrap levels were considered in the tests).

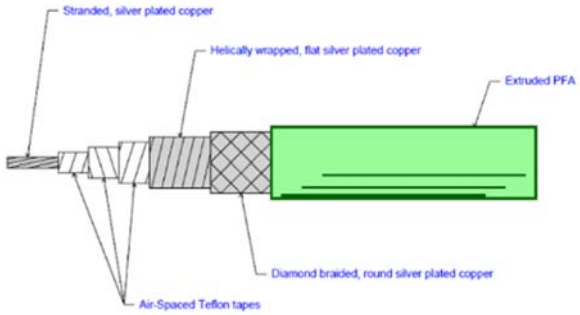

Fig. 3.3-3 Schematic of an ISS co-axial cable

The twisted-pair data cables consists of two 22 AWG stranded conductors with nominal diameters of 0.76mm, covered with tetrafluoroethylene (TFE) insulation such that the nominal diameter of the finished basic wire is 1.32mm. The wires are twisted, along with two 0.889mm diameter fillers inside a tight fitting braided copper shield and covered with a fluorinated ethylene propylene (FEP) jacket having a nominal outer diameter of 3.759mm. The cable is wrapped with beta-cloth using a 50% overwrap (two-layers).

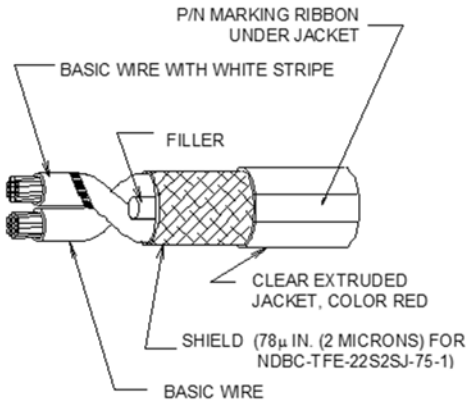

Fig. 3.3-4 Schematic of the ISS data handling twisted-pair cable

3.3.2.2 Experimental Conditions and Results

Primary Power Cables

Table 3.3-1 summarizes results from several of the impact tests on ISS primary power cables [3-3]. These tests were with aluminum 2017-T4 spherical projectiles. All but one of these tests occurred directly on the cables. Other tests positioned the power cables at a distance behind beta-cloth shrouds and/or other protective hardware as exists in locations on ISS (the majority of tests on the primary power lines are not reported here due to space limitations). In some tests single cables were tested. In others, pairs of side-by-side cables were tested to represent cable runs on ISS. If arcing occurred due to a short that developed because of the test, a cable failure was recorded due to a short. However, none of these tests resulted in a failure due to an open circuit (i.e., no conductors were completely severed). The circuit breakers that are part of the system on-orbit would protect downstream equipment if cable failures occurred from shorts/arcing, and it is possible that if a short occurred on-orbit, it may be possible to bring the system back on-line eventually, if the short was cleared or burned free. The results of the tests indicated that the cable shorts can occur with aluminum projectiles between 2.38 mm and 3.175mm diameter at 6.9 km/s. Impact

angle was not a major variable in results of these tests, but the location of the impact on the cable can make a major difference. The cable in test HD9920190 survived a 3.57mm diameter impact which occurred at a location on the cable containing fillers between conductors (there was damage to the conductors in this test, but the impact initially occurred in a region of the cable with fillers), whereas other similar impacts which occurred on the conductors failed the cable by shorting.

Table 3.3-1 Results of ISS Power Supply Cable Tests

HVIT Test #	Projectile Diameter (mm)	Impact Obliquity (°)	Impact Speed (km/s)	Test Result (cable damage measurements represent the extent of damage to the conductors within the cable; damage to the outer layers of the cable are typically much larger than the conductor damage)
HD9920188	2.38	0	6.9	No arc. Cable survived. Cable damage: 14.5mm x 7mm diameter by 11mm deep crater.
HD9920203	3.57	60	5.7	Cable short. 43.5 ms arc sustained after impact (250 A). Cable damage: 15mm x 11mm diameter by 9.8mm deep. Exterior of cable surrounding impact is burnt brown color.
HD9920190	3.57	0	6.6	No arc. Cable survived. Cable damage: 17.5mm x 17mm by 13.2mm deep crater.
HD9920211	3.175	0	6.9	Cable short. (Note, 2 beta-cloth layers located 15cm in front of cable). 34.5 ms arc sustained after impact (250A). Cable damage: multiple 3mm diameter craters.
HD9920197	3.57	45	6.6	Cable short. 178.5 ms arc sustained after impact (275A). Cable damage: 18mm x 17mm diameter by 11.1mm deep crater. SS braid shows extensive melting around impact crater. High speed video shows fire burning in area of fillers. Exterior around impact is a dark burnt color.
HD9920198	3.57	0	6.0	Cable short. 52.5 ms arc sustained after impact (275A). Cable damage: 21mm x 11mm by 11.3mm deep crater. Exterior around impact is burnt brown color.
HD9920212	1.984	45	6.9	No arc. Cable survived.

Co-Axial Cables

Results of NASA hypervelocity testing on co-axial cable are given in Table 3.3-2 [3-4]. Spherical aluminum (Al 2017-T4) and stainless steel (440C) projectiles were used in the tests. Cables failed by shorts between the conductor and overbraid. No open circuits were caused by the tests. Impact angle did not make a large difference in test results. Aluminum projectiles larger than 0.58mm diameter and steel projectiles larger than 0.50mm caused coaxial cable failure at nominal velocity of 7 km/s.

Table 3.3-2 Results of ISS Coaxial Cable Tests

HVIT Test #	Projectile Material	Projectile Diameter (mm)	Impact Obliquity (°)	Impact Speed (km/s)	Test Result
HITF13021	Al 2017-T4	0.793	7.15	0	Open Circuit = No Shorts = Yes, between Conductor and braiding
HITF13022	Al 2017-T4	0.583	6.94	0	Open Circuit = No Shorts = Yes, between Conductor and braiding
HITF13023	Al 2017-T4	0.395	7.05	0	Open Circuit = No Shorts = No
HITF13024	Al 2017-T4	0.478	7.11	0	Open Circuit = No Shorts = No
HITF13025	440C SS	0.500	6.88	0	Open Circuit = No Shorts = Yes, between Conductor and braiding
HITF13026	440C SS	0.380	6.98	0	Open Circuit = No Shorts = No
HITF13027	440C SS	0.402	6.97	45	Open Circuit = No Shorts = No
HITF13028	440C SS	0.496	7.01	45	Open Circuit = No Shorts = Yes, between Conductor and braiding
HITF13029	Al 2017-T4	0.615	7.05	0	Open Circuit = No Shorts = Yes, between Conductor and braiding
HITF13030	440C SS	0.503	6.95	45	Open Circuit = No Shorts = Yes, between Conductor and braiding
HITF13031	Al 2017-T4	0.615	7.18	0	Open Circuit = No Shorts = Yes, between Conductor and braiding
HITF13032	Al 2017-T4	0.621	6.89	35	Open Circuit = No Shorts = Yes, between Conductor and braiding

Twisted Pair Data Cables

Results of NASA tests on twisted-pair data cables are given in Fig. 3.3-5 for normal and oblique (45 deg) impact angles, for aluminum and steel projectiles (spherical) [3-5]. The impact location on the twisted-pair cable was largely responsible for the observed variation in test results. For these cables, both types of failure modes (shorts and open circuits) were observed in the hypervelocity tests. Failure was more often observed if the impact occurred over/on-top of a conductor, then if the impact occurred in areas that contained the filler between conductors.

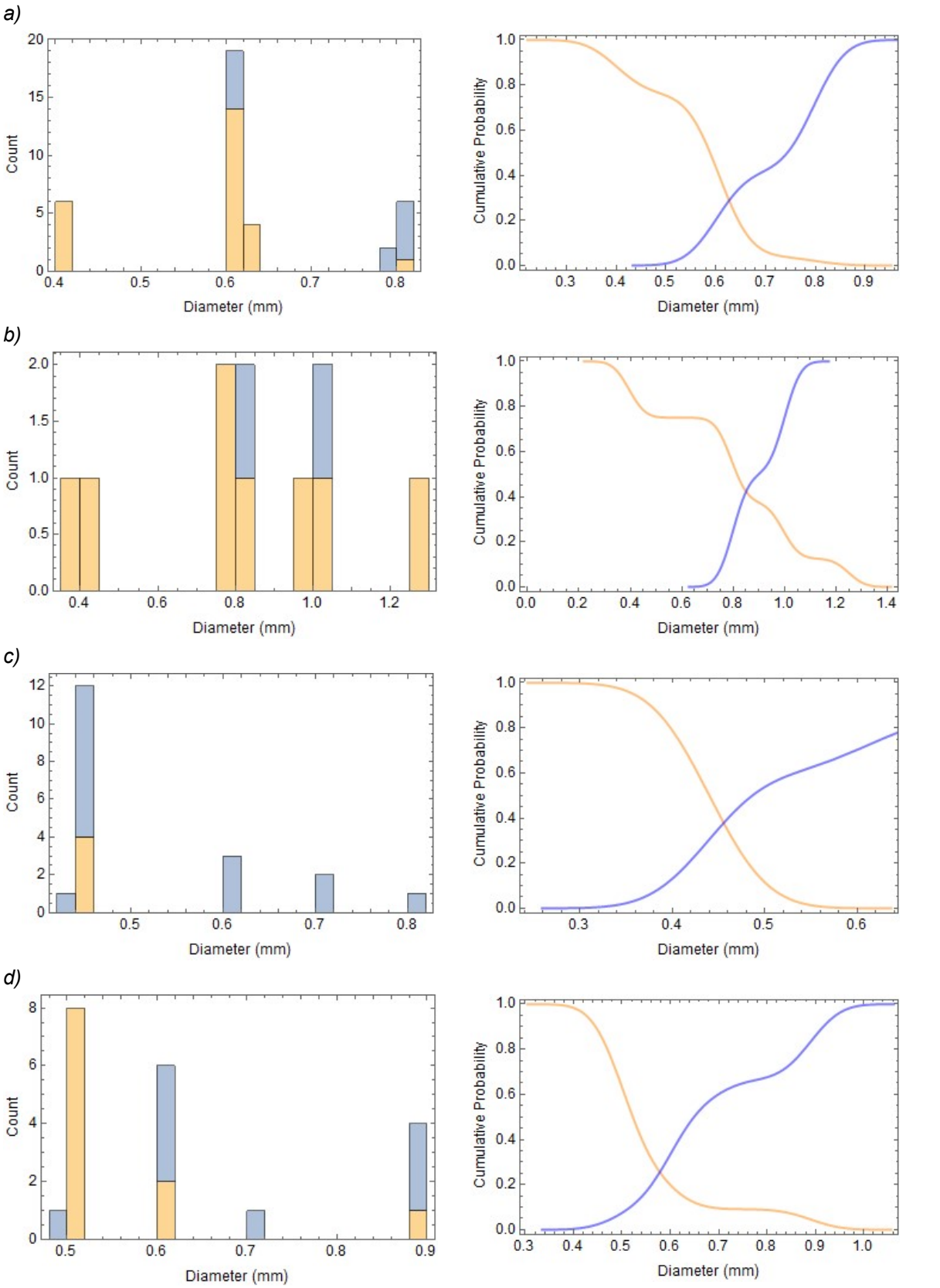

Fig. 3.3-5 Failure statistics for tests on twisted-pair (MIL-STD-1553) cable as function of projectile diameter, showing number of passes (yellow) and fails (blue) along with the cumulative probability of pass (yellow) and fail (blue) from a) normal impact aluminum, b) 45° to normal impact aluminum, c) normal impact steel and d) 45° to normal impact steel

3.4 Recommendation for MMOD risk reduction

For exterior cables, providing separated redundancy is a good way to have a robust system from MMOD failure. Separation of 5-10cm is suggested, to avoid failure of multiple cables in one strike, particular if the cables run under an MLI thermal blanket or other thin projective layers which would cause impacting particles to fragment and spread. Routing cables behind sacrificial materials such as bus structure panels as much as possible and ideally away from external surfaces is also used to increase cable robustness.

Shorting a conductor to a grounded layer within a cable, or between conductors within a cable, is often the failure mode experienced in hypervelocity impact tests for many types of cables. Severing conductors causing an open circuit usually requires larger projectiles and is much less likely to happen from MMOD. Adding additional insulation layers or spacing between the conductors and any overbraid or other grounded layer used for electromagnetic protection will decrease the chance of shorting and improve cable survivability. Multiple tests on cables are usually necessary to establish failure limits due to the complex configuration of the cable, which can contain multiple conductors along with fillers, and especially for twisted pair cables.

3.5 References

[3-1] Schäfer F., Ryan S., Lambert M., Putzar R. (2008). Ballistic limit equation for equipment placed behind satellite structure walls. International Journal of Impact Engineering 35, 1784–1791.

[3-2] Schäfer F., Putzar R., Lambert M. (2008). Vulnerability of Satellite Equipment to Hypervelocity Impacts. 59th International Astronautical Congress. Glasgow, Scotland.

[3-3] J.H. Kerr, F. Lyons, D. Henderson, A.D. Carden, Hypervelocity Impact Testing of International Space Station Primary Power Cables, Presented at the 50th Meeting of the Aeroballistic Range Association, 8-12 November 1999.

[3-4] F.Lyons, NASA HVIT report JSC-66712, Coaxial Cable Test Results, 2014.

[3-5] J. Read, NASA HVIT report JSC-66971, C&DH Wire Harness Hypervelocity Test Results, 2016.

4 Battery

This section provides hypervelocity impact test data for two types of batteries: Lithium-Ion (Li-Ion) and Nickel Hydrogen (Ni-H2) batteries. The impact tests were directed by the NASA Johnson Space Center Hypervelocity Impact Technology (HVIT) group in Houston Texas, and were performed at the NASA White Sands Test Facility (WSTF).

4.1 Damage Mode

Li-ion batteries have been selected to replace Ni-H_2 batteries for the International Space Station (ISS) program to meet the energy storage demands while the ISS is in the Earth's shadow during its approximate 90 minute low Earth orbit. ISS battery boxes are located on the exterior of ISS and are exposed to micrometeoroid and orbital debris (MMOD) impacts. Dedicated MMOD shields on the battery boxes reduce failure risk to an acceptable level.

Hypervelocity impact testing was performed to develop and verify the MMOD shields protecting the Li-ion battery cells (consisting of aluminum honeycomb panel and additional fabric layers), as well as to understand the consequences if at some point in the operation of the ISS a MMOD particle overwhelms the shielding designed for the Li-ion battery packs and damages the battery cells. Under some conditions, thermal runaway events have been experienced in terrestrial applications of Li-ion batteries which have been damaged, and have the potential to propagate to neighboring cells. If thermal runaway occurs in one cell, even undamaged adjacent cells can over-heat and transition into thermal runaway conditions.

Fully charged Li-ion battery cells that are representative of two possible candidates for ISS operations were impacted in hypervelocity impact tests by projectiles that easily defeat the designed shielding for the ISS external battery packs. Even though this is a low probability event, the tests were performed to evaluate if the proposed design prevented the loss of multiple cells due to propagation of thermal runaway from the impacted cell to adjacent cells.

Hypervelocity impact tests were also performed on Ni-H_2 batteries representative of ISS Ni-H_2 battery cells, which are contained within a box that is made from aluminum honeycomb sandwich panels. The Ni-H_2 battery cells were fully-charged and pressurized with hydrogen to 60 atm prior to the impact tests. The failure mode of concern is a rupture and fragmentation of the pressure shell of Ni-H_2 battery cell, and propagation to neighboring cells.

4.2 Impact Experiments and Numerical Simulations / NASA

4.2.1 Li-Ion Impact Experiments

Hypervelocity impact conditions on Li-ion cells are summarized in Table 4.2-1 [4-1]. Each test article used two separate Li-ion battery cells but only one was targeted. A second cell is included to determine if failure can propagate to a nearby undamaged cell. The impact locations were typically at the terminal end of the battery cells, although some shots to the side of the Li-ion battery were also performed. Two different types of Li-ion batteries were tested with similar results. When penetrated, the impacted Li-ion battery typically increases in temperature while the cell contents are ejected and can in some cases auto-ignite. The neighboring cell will in most cases increase in temperature, but only occasionally will the temperature increase substantially resulting in failure of the undamaged cell due to thermal runaway. A sequence of images of the Li-ion battery response from one test is shown in Fig. 4.2-1. This test resulted in a visible deflagration as the impacted cell contents were

energetically ejected over a several second time period following cell penetration. The aluminum honeycomb panel in front of the cell was severely melted due to the expelled cell material (Fig. 4.2-2a). The neighboring cell did not transition into thermal runaway. Fig. 4.2-2b shows the cells after the impact test.

Table 4.2-1 Li-Ion cell impact conditions.

Test #	Projectile Diameter (mm)	Impact Obliquity (°)	Impact Speed (km/s)	Cell Damage Measurements (mm)
HITF12143	10.0	0	6.86	Primary cell-Perforated with peak temperature of 184°C Secondary cell-No ignition or thermal runaway
HITF12144	10.0	0	7.02	Primary cell-Perforated, no ignition, peak temperature 194°C Secondary cell- Thermal runaway peaking at 531°C
HITF12145	10.0	30	7.05	Primary cell-No Perforation Secondary cell-No Perforation
HITF12147	13.5	45	6.88	Primary cell-Perforated with peak temperature of 193°C Secondary cell- Thermal runaway peaking at 315°C
HITF12148	10.0	0	7.19	Primary cell-Perforated, no ignition Secondary cell-No ignition or thermal runaway

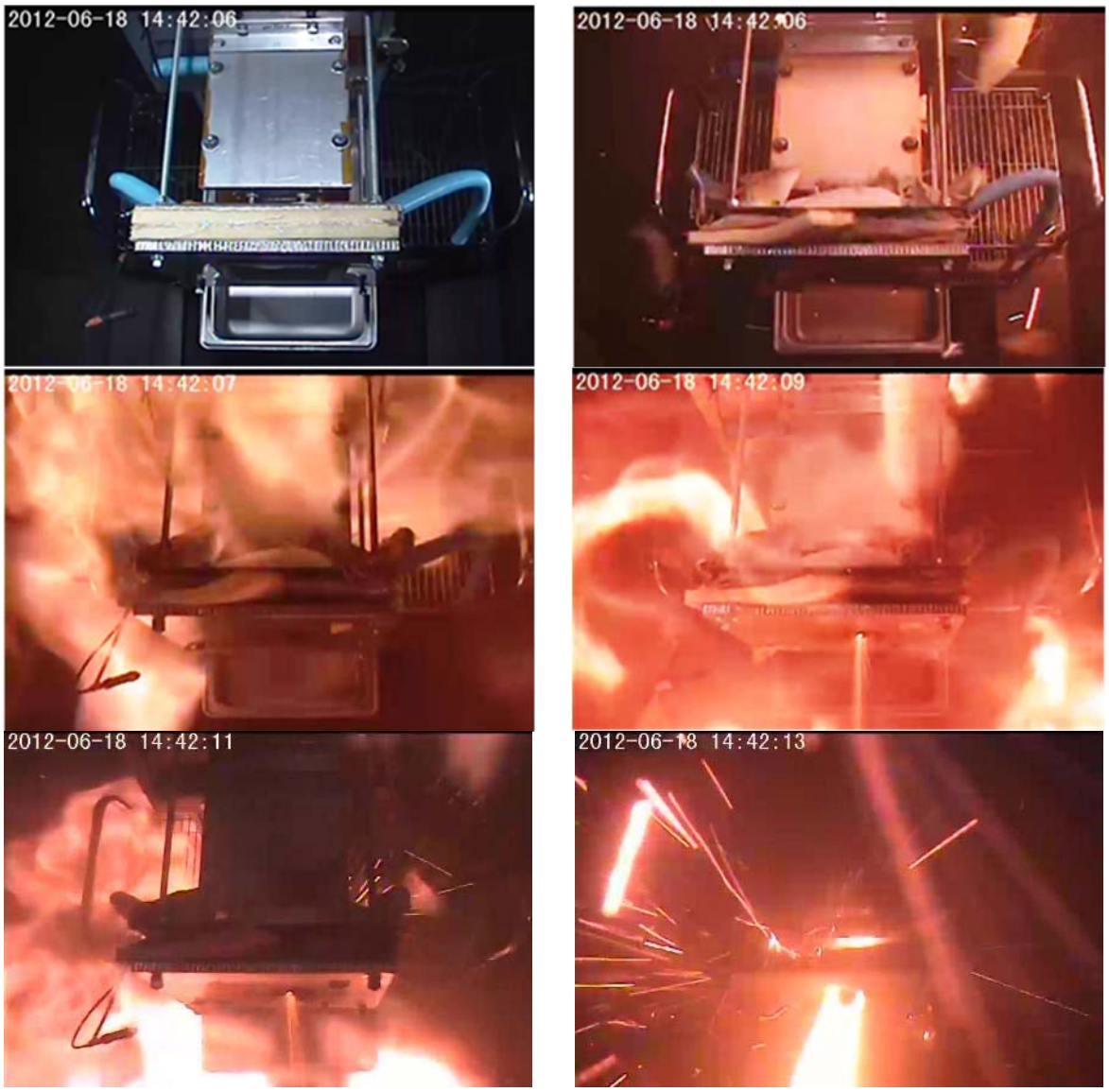

Fig. 4.2-1 HITF12143 visible video frames at 1s-2s intervals after impact.

a) b)

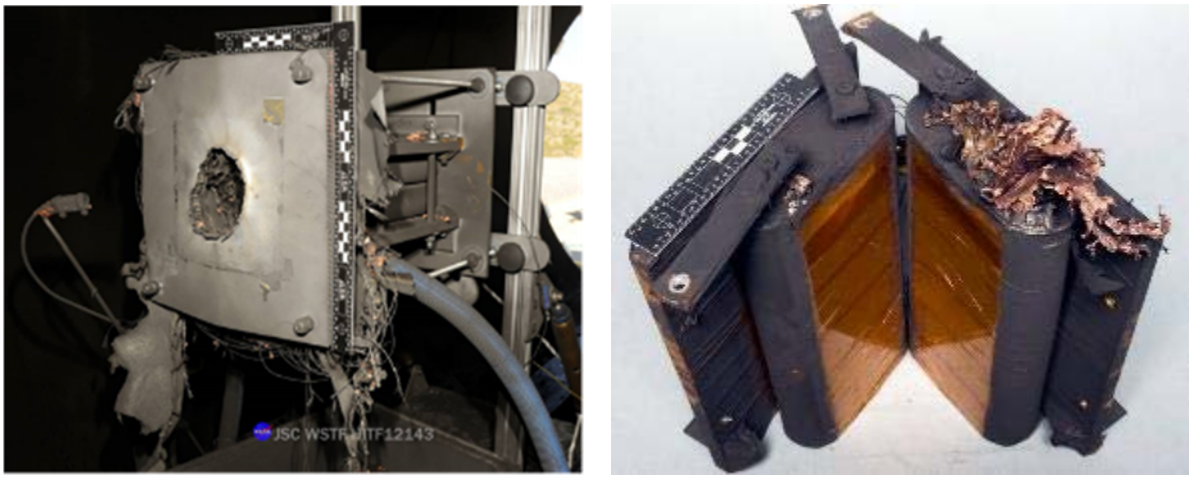

Fig. 4.2-2 After test imagery of HITF12143 a) shield with 9.5cm diameter through-hole, and b) cell close-up with impacted cell on right showing molten material from cell interior that was ejected and deposited on exterior of cell.

4.2.2 Ni-H2 Cell Impact Experiments

Ni-H_2 battery hypervelocity impact tests were performed on a legacy configuration of the ISS orbital replacement unit (ORU) battery assembly as shown in エラー! 参照元が見つかりません。4.2-3. Thirty-eight cylindrical battery cells are contained in the enclosure as seen in エラー! 参照元が見つかりません。4.2-3b. The Ni-H_2 battery cells are constructed from Inconel 718 with minimum thicknesses in the cylinder of 0.8 mm and the dome of 0.65 mm.

a) b)

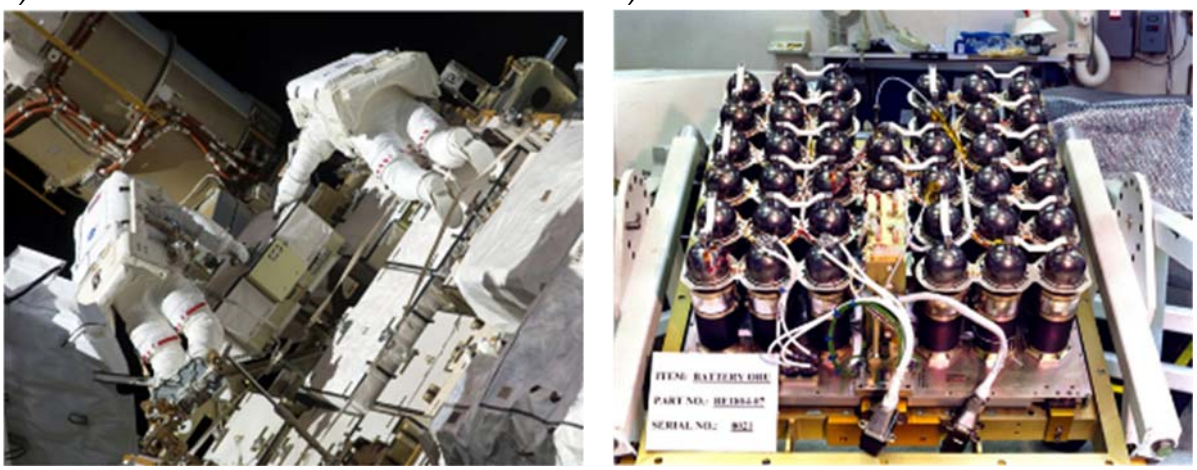

Fig. 4.2-3 a) ISS Ni-H_2 battery ORU and b) ORU subassembly without enclosure.

The Ni-H_2 cell considered in this testing generates hydrogen gas in the free cell volume as a result of the chemical reactions that occur during charging. The hydrogen accumulates up to a design pressure of 6 MPa which indicates 100% state of charge (SOC) for the rated 81 ampere-hour (Ah). The cells contain an aqueous potassium hydroxide (KOH) electrolyte solution. The cells were proof tested to 10.3 MPa and have a burst pressure of 37.2 MPa. The burst factor for this cell is 6 (burst pressure/operating pressure). In the event of over-pressurization, the cells are designed to leak before burst. Impact testing was performed to

determine if the vessel fragments after penetration and to assess if there are any adverse reactions with the electrode materials, thermal events or cascade failure responses.

The enclosure consists of an aluminum honeycomb panel with 0.4 mm facesheets separated by 12.7 mm thick honeycomb that is covered by a multi-layer insulation blanket (0.086 g/cm^2).

The Ni-H_2 impact conditions are summarized in Table 4.2-2. These tests impacted through the aluminum honeycomb enclosure, and were targeted to consider three basic locations on the Ni-H_2 battery: in the dome, into the terminals on the top of the domes, and into the side. Various aluminum and steel projectile diameters were used in the tests, at impact speeds of 7 km/s and impact angles of 0° and 45° to the normal of the honeycomb panel. None of the tests resulted in fragmentation of the cells. No thermal events or cascading failures resulted to neighboring cells. The largest perforations are shown in Fig. 4.2-4a (test HITF13144) and Fig. 4.2-4b (test HITF13165). Generally, the response to cell perforation was that the Ni-H2 cell vented and the voltage across the terminals declined until the cell could no longer maintain current over a load. In one case, the battery box cover was deformed because cell venting occurred so quickly that the box pressure increased sufficiently to deform the cover.

Table 4.2-2 Ni-H_2 impact conditions.

Test #	Impact Location	Projectile Diameter (mm)	Impact Obliquity (°)	Impact Speed (km/s)	Cell Damage Measurements (mm)
HITF13144	Dome	5.0	0	6.66	11.5 x 10.0 Perforation
HITF13145	Dome	4.0	0	6.86	1.0 x 1.5 Perforation
HITF13146	Dome	3.8	0	7.09	1.5 x 2.4 Perforation
HITF13147	Dome	3.4	0	7.09	2.4 x 3.5 Perforation
HITF13148	Dome	3.0	0	7.00	2.5 x 1.5 Perforation
HITF13149	Dome	2.8	0	7.19	No Perforation
HITF13151	Terminal	2.9	0	7.19	No Perforation
HITF13152	Terminal	3.1	0	7.12	No Perforation
HITF13153	Terminal	3.3	0	6.85	No Perforation
HITF13154	Terminal	4.2	45	7.13	1.6 x 1.2 Perforation
HITF13155	Terminal	3.0*	45	7.00	1.5 x 1.5 Perforation
HITF13158	Dome	5.0	45	7.13	2.0 x 2.0 Perforation
HITF13159	Dome	4.0	45	7.00	No Perforation
HITF13160	Dome	4.2	45	7.07	1.8 x 08 Perforation
HITF13162	Terminal	5.0	0	7.05	7.5 x 7.0 Perforation
HITF13163	Terminal	4.8	0	7.07	No Perforation
HITF13164	Terminal	5.1	0	7.04	3.0 x 1.0 Perforation
HITF13165	Terminal	3.8*	0	6.87	18.0 x 8.0 Perforation
HITF13174	Side	4.1	45	7.04	1.0 x 4.0 Perforation
HITF13175	Side	3.9	45	7.04	No Perforation

a) b)

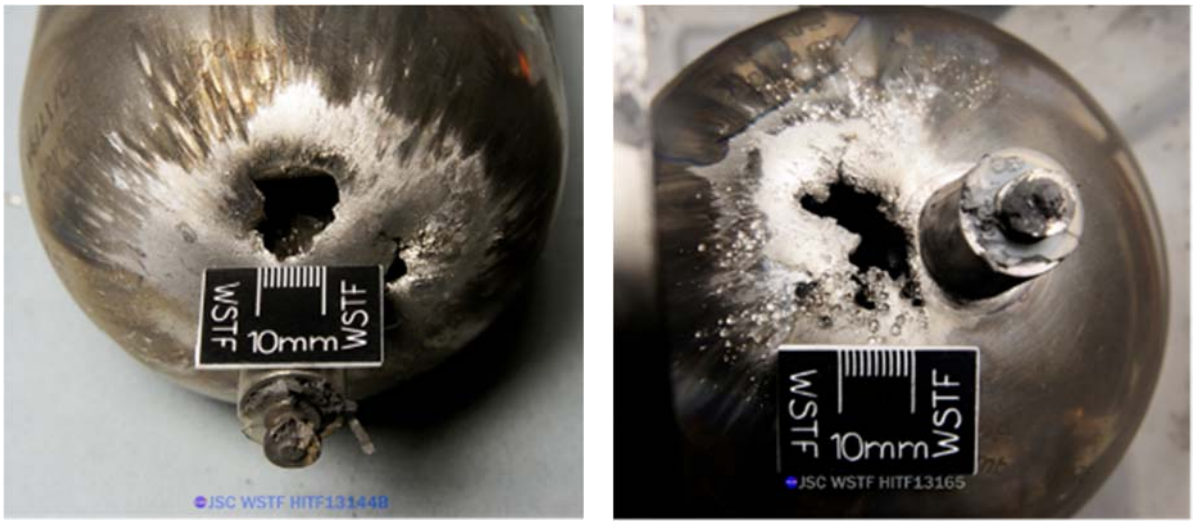

Fig. 4.2-4 ISS a) HITF13144 and b) HITF13165.

4.3 Recommendation for MMOD risk reduction

The use of rechargeable batteries in orbital spaceflight requires consideration of the uncontrolled energy release from a cell, which is dependent on the type of cell. Impact experiments have evaluated the failure mechanisms of the pressurized Ni-H_2 battery cell and the charged Li-Ion battery cell. For the operational design of the Ni-H_2 battery like those used on the ISS, the hydrogen gas will vent on perforation of the battery vessel; but unusual thermal events or catastrophic rupture did not occur. The ISS Ni-H_2 battery cells have a relatively high burst factor of 6. When pressurized battery cells are used in other spacecraft, attention to the burst factor of the cell should be taken into account.

Impact tests on Li-ion battery cells demonstrated an energetic release of energy when shielding is overmatched and the cell is penetrated. The impacted cell typically will overheat and will vent/eject the internal contents of the cell, including molten metal, rapidly after impact (within a few seconds). In some cases the venting material will auto-ignite, even in the vacuum environment of the test chamber. Depending on the design of the battery cell enclosure, neighboring Li-ion cells can also experience increases in temperature and can fail due to thermal runaway.

Shielding for batteries could be selected based upon the type of cell to be protected, typical failure modes and the acceptability for loss of battery cells. Supplemental shielding for Li-ion batteries should be designed to meet survivability requirements without allowing perforation of the cell wall. Shield and battery designs should be verified by test to ensure they meet protection requirements.

4.4 References

[4-1] F. Lyons, NASA HVIT test report, JSC-66713, ISS Lithium Ion Battery Hypervelocity Impact Test Evaluation, 2016.

5 Electronic Box

5.1 Damage Mode

Laboratory tests suggest that e-boxes have to be mechanically damaged to show signs of failure. Failure is understood as temporary or permanent disruption of all or just part of the e-box functions.

1) Temporary failures in the experiments were characterized by short interruptions in the operation of the processor, followed by nominal operation a few milliseconds later. The reason for temporary failures is assumed to be related to conductive dust, which caused transient shorts between electrical circuits on the PCB.
2) The permanent failures manifested as sudden loss of supply voltage or loss of nominal operation of the computer.

5.2 Impact Experiments and Numerical Simulations / EMI

Electronics boxes (E-Box) are computers or, more generally, assemblies of printed circuit boards enclosed in an aluminum box that are widely used in all satellite subsystems including the payload. Typically, a share of 20% to 40% of a satellite bus volume consists of electronics boxes. The casing of an E-Box is typically made of milled aluminum with a thickness of between 1 to 3 mm. If the casing of an E-box is perforated during an impact, fragments penetrate its interior and may damage or destroy the electronic components, leading to potentially catastrophic consequences for a mission if this system is not redundant.

For the laboratory hypervelocity impact tests, simplified electronics boxes representative of onboard computers were designed. The onboard computer consisted of a printed circuit board (PCB) with FPGA, clock, integrated circuits, memory units, interfaces etc., located inside an aluminum box, at a stand-off S_2 of 28 mm behind the box lid. In the experiments the Al-box was placed behind an aluminum honeycomb sandwich panel (Al H/C SP) with MLI, same specification as above. Three different stand-offs between sandwich panel and front wall of the electronics box, $S_{1,}$ were selected: 0, 100 and 300 mm. The lid thickness of the electronics casing was varied between 1 and 3 mm.

In the laboratory hypervelocity impact tests, the computer-boxes were in an operational mode, performing basic read- and write-operations. The observed failure modes induced by the impact were temporary failure and permanent failure. The temporary failures caused interruptions in the operation of the processor, followed by nominal operation a few milliseconds later. The reason for temporary failures is assumed to be related to conductive dust, which caused transient shorts. Any temporary failure i.e., temporary loss of operational performance of electronic components may manifest itself to the system operator as an in-flight anomaly. Such in-flight anomalies, including faulty data transmission and ‘ghost commands’, have been reported and hence, may be explained by hypervelocity impacts. The permanent failures manifested as sudden loss of supply voltage or loss of nominal operation of the computer.

Table 5.2-1 summarizes some a series of experiments published in [5-1].

In Fig. 5.2-1, a PCB with severe impact damages (memory chip, resistors and capacitances removed, deposits of metallic spray in various locations) and the corresponding CPU signals are shown.

Table 5.2-1 Test results matrix from HVI tests on E-Boxes: S_1 – stand-off between rear side of structure wall and E-Box front lid, t_L – thickness of E-Box cover lid, v_0 – impact velocity, d_P – projectile diameter, α impact angle (0° corresponds to perpendicular impact direction) [6.2]

Exp.	S_1 [mm]	t_L [mm]	v_0 [km/s]	d_P [mm]	α [°]	E-Box Test Results Damage to Lid Mechanical Damage	E-Box failure type
4699	0	1.5	6.41	2.3	0	perforation	destroyed
4708	0	1.5	6.08	2.3	0	perforation	temporary error
4718	0	1.5	6.59	2.8	0	perforation	destroyed
4703	0	2.0	6.56	2.3	0	perforation	no malfunction
4701	0	3.0	6.17	3.2	0	perforation	destroyed
4702	0	3.0	6.65	2.5	0	no perforation	no malfunction
4721	0	2.0	6.75	3.5	45	perforation	no malfunction
4722	0	2.0	3.34	2.8	45	no perforation	no malfunction
4723	0	2.0	3.39	3.5	45	no perforation	no malfunction
4714	100	1.5	3.66	2.5	0	no perforation	no malfunction
4715	100	1.5	3.52	3.2	0	no perforation	no malfunction
4716	100	1.5	3.81	4.0	0	perforation	destroyed
4712	100	1.5	4.7	2.5	0	perforation	no malfunction
4704	100	1.5	6.56	4.0	0	detached spall	no malfunction
4706	100	1.5	6.17	4.5	0	perforation	temporary error
4719	100	1.5	6.55	4.5	45	no perforation	no malfunction
4720	100	1.5	6.60	5.5	45	no perforation	no malfunction
4711	300	1.0	5.8	3.2	0	perforation	no malfunction
4710	300	1.0	5.44	4.0	0	perforation	destroyed
4700	300	1.5	6.76	5.0	0	detached spall	temporary error
4709	300	1.5	5.66	5.5	0	perforation	destroyed

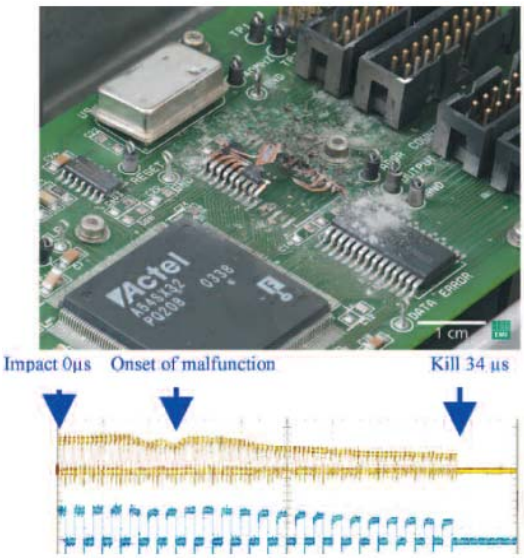

Fig. 5.2-1 Degradation of computer performance followed by cease of operation shortly after incident of the hypervelocity particle.

5.3 Recommendation for MMOD risk reduction

- Thickening of exposed e-box lids or addition of protective materials (high-strength fabrics etc.)
- Additional shielding between structure wall and e-box lid (e. g. stuffing from appropriate Kevlar/Nextel combinations)
- Additional shielding of the structure wall by e.g. external shields (protection enhanced MLI etc.)

5.4 References

[5-1] Schäfer F., Putzar R., Lambert M. (2008). Vulnerability of Satellite Equipment to Hypervelocity Impacts. 59th International Astronautical Congress. Glasgow, Scotland.

6 Structure / Effect of Material Degradation

This section provides brief review of hypervelocity impact (HVI) study on three types of structural part, namely: metallic walls, structural panels and composite parts.

6.1 Damage Mode

Metallic Walls Experimental studies have shown that the impact damage in the perforated unshielded wall ranges from the petal hole to a hole surrounded by a strain-affected region with the microcracks created by the passage of compressive and rarefaction waves [6-1][6-2]. For the case of both shield and metallic part perforation the impact damage varies from the petal hole to the “cookie-cutter hole”. The crack-like defects in the vicinity of the perforated hole have a significant effect on the residual strength of the impact-damaged structures. The problem of their potential catastrophic fracture was extensively examined by the NASA Advanced Fracture Mechanics Group [6-3]-[6-4][6-5] and Research Lab ONIL-17 at Samara State Aerospace University [6-6]. Comparison to the experimental data showed that the linear elastic fracture mechanics methods are too conservative and non-linear fracture mechanics approach is required for a more realistic treatment of the problem.

Structural Panels Honeycomb sandwich panels are the traditional primary structures used in spacecraft construction due to their light weight and high strength and stiffness; their performance under hypervelocity impact has been investigated experimentally and by means of numerical simulation in many studies [6-7]-[6-11]. The studies revealed that the presence of honeycomb core restricts the expansion of debris cloud fragments having the negative effect (known as channeling) on the shielding performance of the panel. As a promising alternative to the honeycomb core, a number of researchers has considered open-cell aluminum foam [6-12]-[6-14]. The performance improvement in case of using the foams was observed which could be explained not only by the possibility of radial expansion of debris cloud due to absence of the channeling cells but also by the repeated impact of fragments on individual foam cell ligaments inducing further fragmentation, melt and vaporization of fragments.

Composite Parts Composite materials are being used extensively for space applications. A number of experimental programs have been conducted to study the behavior of composites under HVI [6-15]-[6-21] and demonstrated the complexity of the impact damage pattern and failure mechanisms. Numerical techniques for the modeling of composite subjected to hypervelocity impact have been described in the literature [6-22][6-23] and implemented in commercial software packages, such as ANSYS Autodyn. These techniques are designed for the standard laminated composites represented in the modeling as a macroscopically homogeneous orthotropic media with effective properties equivalent to those of the real material. The homogenization-based techniques are inapplicable to the composites fabricated by filament winding. In order to incorporate the detailed representation of the fabrication patterns into numerical simulations, the meso-scale modeling approach was introduced in [6-24]-[6-26]. Due to its generality, this approach can be applied to both standard laminated and filament-wound composites.

6.2 Impact Experiments and Numerical Simulations / CSA

6.2.1 Summary of Conditions and Results

The consequences of hypervelocity impact on structural elements such as metallic walls, structural panels and composite parts were studied experimentally and numerically. In order to accommodate the diversity of the impact damage pattern in the conventional metallic wall a universal impact damage is suggested. To reduce computational cost, complex materials are often represented in HVI modeling as homogeneous substances with the effective properties similar to those of the real materials. Although this approach has been successfully used in modeling of HVI on different materials with complex architecture, there are applications where it may not be applicable due to significant influence of materials' meso-scale features on resulting HVI damage. Two of such applications are considered in this study, and include simulation of HVI on sandwich panels with metallic foam-cores, and composites fabricated by filament winding. In the former case, adequate modeling of the multi-shock action of the foam ligaments on hypervelocity fragment cloud propagating through the foam core requires an explicit representation of the foam geometry in numerical model. In the latter case, the meso-scale modeling is required due to experimentally observed dependence of HVI damage of the composite on the particular filament winding pattern used in its fabrication. The study presents numerical models developed for both of these applications and compares numerical results with obtained experimental data.

6.2.2 Details

6.2.2.1 Metallic Wall

A variability in the structure design parameters and impact conditions leads to a variety of impact damages formed in the metallic wall making the failure analysis challenging. In order to accommodate the diversity of the impact damage pattern it is suggested to model the cracked area around the penetrated hole by two radial cracks emanating from the rim of the hole perpendicularly to the applied load, i.e. along the expected fracture path (Fig. 6.2-1). The diameter of the model hole is equal to the diameter of the impact hole (D_{hole}) and the length of the fictitious radial cracks is bounded by a damage zone (D_{crack}) [6-6]. The fracture propagation analysis employs the non-linear fracture mechanics technique. Model provides a universal approach which fits all penetration scenarios to replicate the observed fracture behavior of the impact damaged structures. This work started at Samara State University and continued at the University of Manitoba.

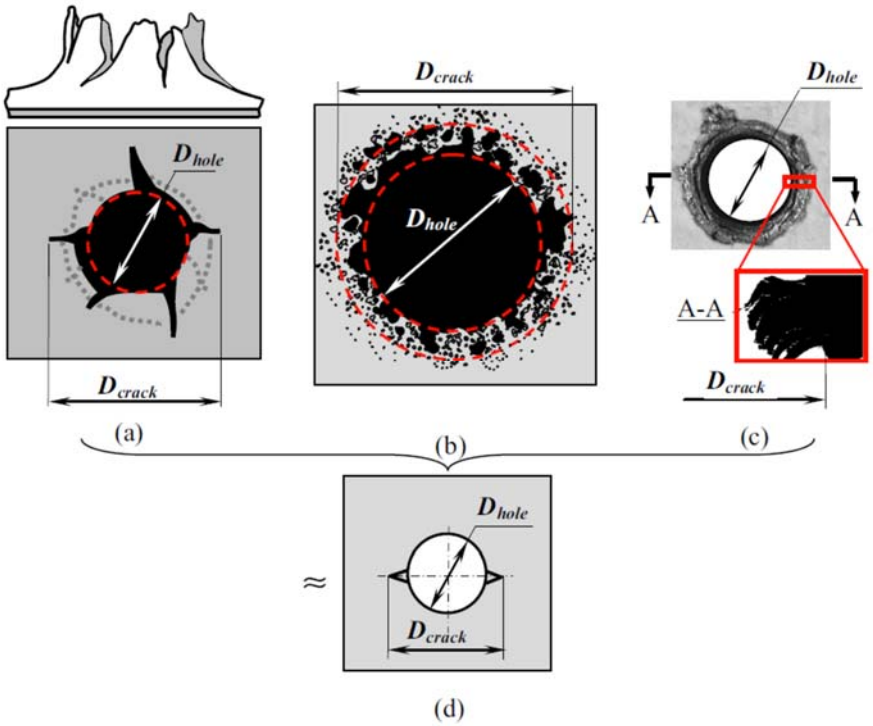

Fig. 6.2-1 Modeling the impact holes: (a) petal hole; (b) ‘‘cookie-cutter hole”; (c) hole with adjacent spall cracks; (d) model of impact hole

6.2.2.2 Structural Panel

The concept named “ENSURE” (ENhanced SURvivability Elements) is used by the University of Manitoba team to develop effective MMOD protection without prohibitive additional weight. Concept is based on the idea of redesigning the original spacecraft parts such as structural panels to enhance their inherent capability to act as an element of impact protection. The structural panels can be turned into the multifunctional components offering impact protection in addition to their original function. This can be advantageous in terms of weight savings, as well as savings in space, materials, and manufacturing costs.

Two types of structural panels were evaluated in [6-14], namely, honeycomb-core and foam-core sandwich panels, when used to protect an unmanned space vehicle against small debris (1 mm particle an impact velocity of 7 km/s). Examples of the damage that can be produced by a 1 mm aluminum projectile accelerated to 7 km/s are given in Fig. 6.2-2.

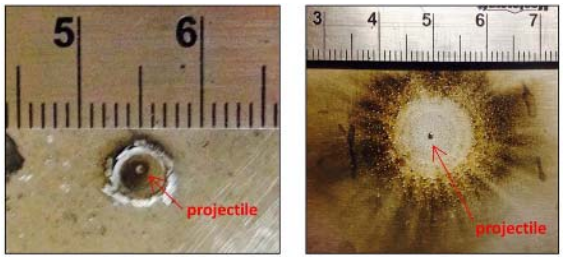

Fig. 6.2-2 Damage from 7 km/s impact of 1 mm aluminum projectiles on a monolithic aluminum target (left) and the rear wall of a double-wall aluminum shield (right)

It can be deduced from this figure that even such a tiny particle can produce a lot of damage and potentially cause failure of spacecraft components such as pressure vessels, tethers, electronic circuit boards, etc.

Honeycomb-core sandwich panels (HCSP) are well known for their superior structural properties. However, compared with Whipple shields, honeycomb panels are more easily penetrated in the case of normal impacts because of channeling of the debris cloud after perforation of the first facesheet. This channeling results from the interaction of the debris cloud with the walls of the honeycomb cells. Metallic foam-core sandwich panels (FCSP) have been recognized as prospective substitutes for honeycomb-core panels because of the lack of such a tunneling effect and the multishock action on the debris cloud propagating within the space filled with foam. The preliminary sizing of panels were performed using the ballistic equations and finalized by means of numerical modeling. The standoff between the bumper and the rear wall (or the front and rear facesheets for sandwich panels) was chosen from within the typical range of $15d_p < S < 30d_p$ as S=16 mm.

The structural functionality of these panels is ensured by their flexural stiffness, which has to be no lower than some minimum specified value. The minimal required level of flexural stiffness is determined by a reference honeycomb sandwich panel with 0.5-mm-thick aluminum facesheets and a 16-mm-thick core. These parameters of the reference sandwich panel are close to the lower boundary of the typical range for unmanned spacecraft structures, which is 0.25–2.00 mm for the facesheet thickness and 5–50 mm for the overall panel thickness. In addition, these panels often have equal-thickness facesheets in order to avoid unwanted bending–stretching coupling when subjected to structural loads. Thus, the considered sandwich panels are symmetrical relative to their midsurface.

Parameters of the HCSP and FCSP cores considered in this study are presented in Table 6.2-1. The cores have similar values of reference density. The cell size of the aluminum foam was chosen so as to be less than the diameter of the projectile, in order to maximize the

intensity of the interaction between the foam layer and the debris cloud. This consideration led to the minimal commercially available size of 40 ppi.

Table 6.2-1 Parameters of the cores for sandwich panels

No.	Core type	Core thickness, mm	Reference density, % of base material
1	1/8 – 0.0015[a] aluminum honeycomb by Hexcel	16.0	3.60
2	40 ppi aluminum foam by ERG Aerospace	16.0	3.00

[a]Hexcel honeycomb designation: cell size (in inches)–wall thickness (in inches).

The employed modeling approach is based on simultaneous utilization of both SPH and the FEM in each numerical simulation. The SPH method is used to represent the behavior of parts exhibiting fragmentation, namely, bumpers, front facesheets, and aluminum foam. The rear facesheets and honeycomb-core are simulated using FEM. All simulations are preformed using ANSYS Autodyn v15.0.7

The representative element of the honeycomb panel is shown in Fig. 6.2-3. Results of the simulation (see Fig. 6.2-4) indicate that the panel will be easily perforated by a 1 mm aluminum projectile at 7 km/s. It can be noted that, because of the shape of the honeycomb cell, not all locations are equipotential, and material in the debris cloud (in the course of radial expansion) tends to concentrate in the corners of the hexagon rather than being uniformly distributed over its circumference. This effect reveals itself in the resulting

perforation pattern, as is shown in Fig. 6.2-4. Taken together with the well-known channeling effect (i.e., constraining of expansion of the debris cloud by the honeycomb cells), the honeycomb at normal impact thus produces “double-focusing” of the debris cloud (the debris cloud is focused/channeled by a cell and, within the cell, it is focused in its corners).

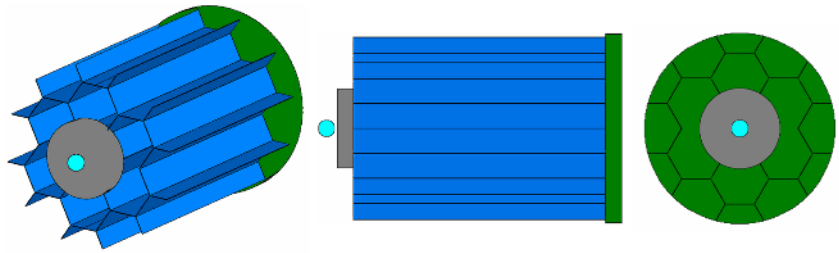

Fig. 6.2-3 Representative element of honeycomb-core sandwich panel

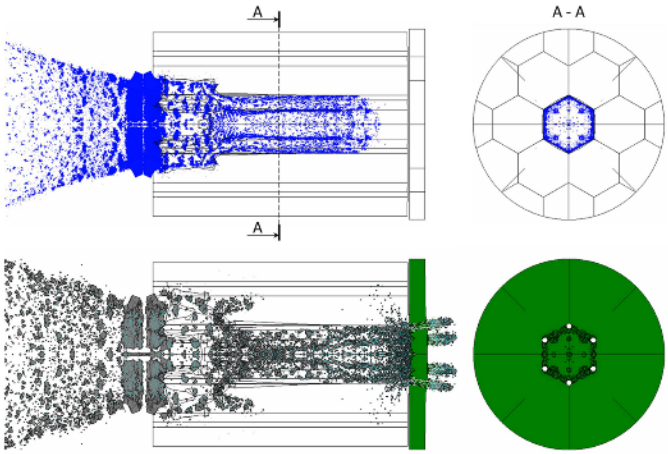

Fig. 6.2-4 Simulation of HVI on honeycomb-core sandwich panel [6-14]

The original structure that formed metallic foam was a three-dimensional array of bubbles having a maximum volume for the minimal surface area and surface energy. In the course of the fabrication process, membranes of the bubbles were removed, leaving an interconnected network of solid struts. Adequate modeling of the multi-shock action of the foam ligaments on hypervelocity fragment cloud propagating through the foam core requires an explicit representation of the foam geometry in numerical model. The SPH model of the foam-core sandwich panel is depicted in Fig. 6.2-5. The foam in the model is present only in the central region of the panel, where the most energetic fragments with the greatest damage potential will propagate. Additional lateral extension of the foam model was found to be impractical, as it was associated with high computational expenses.

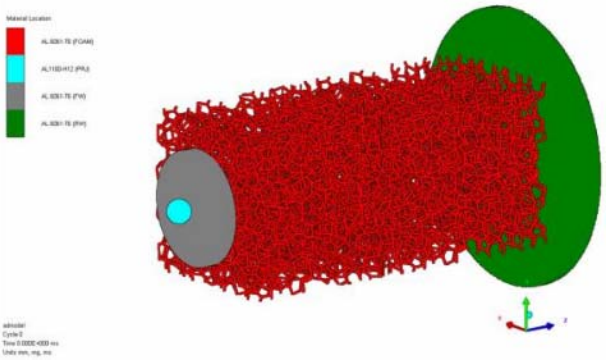

Fig. 6.2-5 Numerical model of the open cell foam-core sandwich panel

Results of the conducted simulation are presented in Fig. 6.2-6, which demonstrates three consequent moments of time when the debris cloud propagates through the aluminum foam. It can be seen in the figure that multi-shock action of the foam effectively breaks up fragments of the projectile and the front bumper, converting them into a cloud of small, disperse particles. No perforation of the rear wall was detected during the numerical experiment.

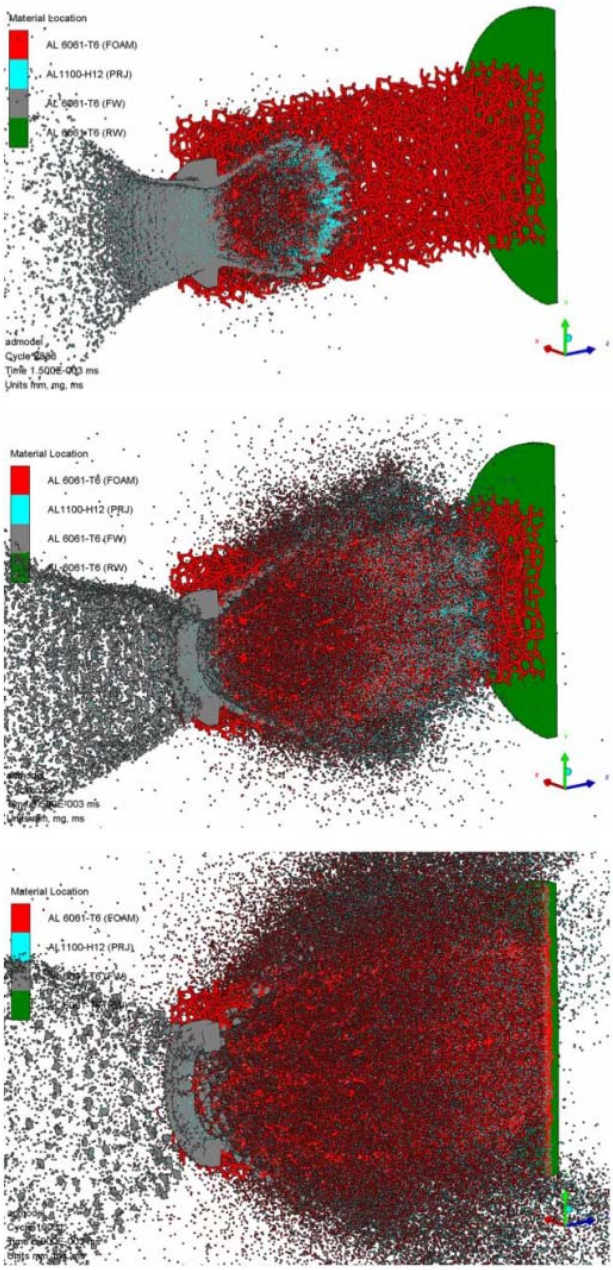

Fig. 6.2-6 Results for the foam-core sandwich panel: a) t = 1.5 μs; b) t = 3.5 μs; and c) t = 8.5 μs [6-14]

In view of the novelty of the foam modeling approach (i.e., its mesoscale representation in HVI analysis), the numerical prediction was verified by means of a physical experiment. The experiment was carried out using a two stage light gas gun at the HIT Dynamics, Ltd., impact testing facility (Canada). The tested panel consisted of two Al6061-T6 facesheets and 16-mm-thick 3% 40 ppi aluminum foam from ERG Aerospace (Fig. 6.2-7).

The panel was impacted by a 1 mm aluminum projectile at 6.965 km⁄s, and the resulting damage to the panel is shown in Fig. 6.2-8. Rear-wall damage was represented by discoloration and barely noticeable bulging. No perforation of the rear wall was detected, which supported the results of the numerical simulation. Therefore, the considered configuration of the FCSP provides the minimal required bending stiffness and can be used to protect a spacecraft from 7 km⁄s impacts of 1 mm debris particles.

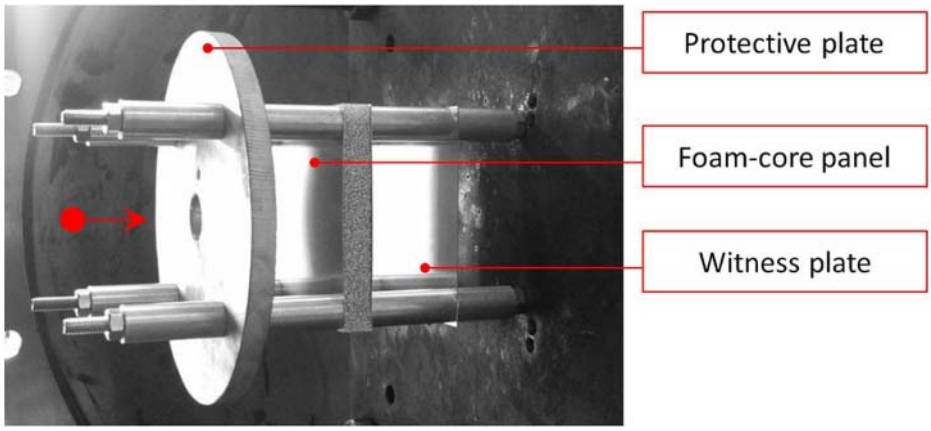

Fig. 6.2-7 Experimental setup

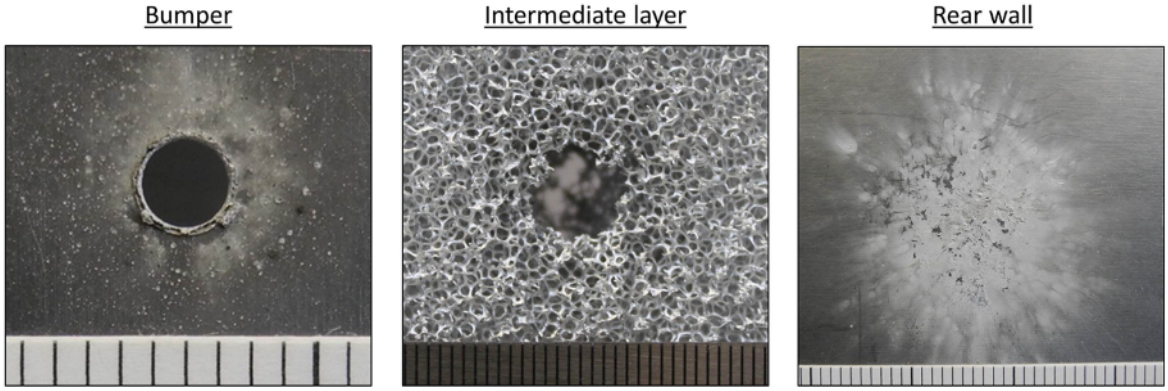

Fig. 6.2-8 Results of experiment for FCSP [6-14]

According to the numerical simulations, the parameters of the structural panels that satisfied the imposed constraints (no-perforation, bending stiffness and equal facesheet thickness) and had the minimal weight in their class were as follows: a) HCSP of 1.45mm Al6061 +[1/8 - 0.0015] aluminum honeycomb + 1.45 mm Al6061 and b) FCSP of 0.5 mm Al6061 + 3% 40 ppi aluminum foam + 0.5 mm Al6061. Analysis of these data shows that, the areal density of the FCSP (0.400 g/cm^2) is more than twice as low in comparison with the HCSP (0.940 g/cm^2) having a similar ballistic performance, even in the presence of the minimal bending stiffness constraint, which limits further reduction of the FCSP facesheets' thickness.

The performed analysis showed that if the critical component is located behind a honeycomb-core sandwich panel, which must be in place for structural reasons, and the structural panel in the baseline design does not provide the required level of orbital debris protection, then its modification through the replacement of the honeycomb core by aluminum foam will be more weight efficient than thickening the facesheets of the baseline honeycomb-core panel.

6.2.2.3 Composite Parts

Filament winding is a common manufacturing technique (e.g. for composite overwrapped pressure vessels, composite truss tubes etc.) which is characterized by meso-scale inhomogeneity of the fabricated material, in addition to microscopic inhomogeneity inherent to all types of composites. The former feature results from multiple interweavings of filament

bands forming a filament-wound composite part. Behavior of composites under HVI has been studied experimentally and numerically by many researchers, e.g. [6-15]-[6-21]. However, most of the reported work was confined to the standard laminated composites, whereas less attention has been paid to the filament-wound materials.

Telichev and Cherniaev from the University of Manitoba studied the manufacturing features and defects of fabrication that may influence the response of composite parts to HVI [6-24]-[6-26]. Two types of filament-wound specimens different in terms of degree (or “density”) of filament bands interweaving were manufactured for the purposes of this study. The types were designated as “low” and “high” degree of interweaving specimens (LDI and HDI, correspondingly). The overall manufacturing process is schematically illustrated in Fig. 6.2-9. As a result, flat 200 × 200 mm specimens with filleted corners and metallic reinforcing tabs were fabricated. LDI specimens had a single row of filament band crossover points in the center, whereas HDI specimens had multiple rows of crossovers in the test area.

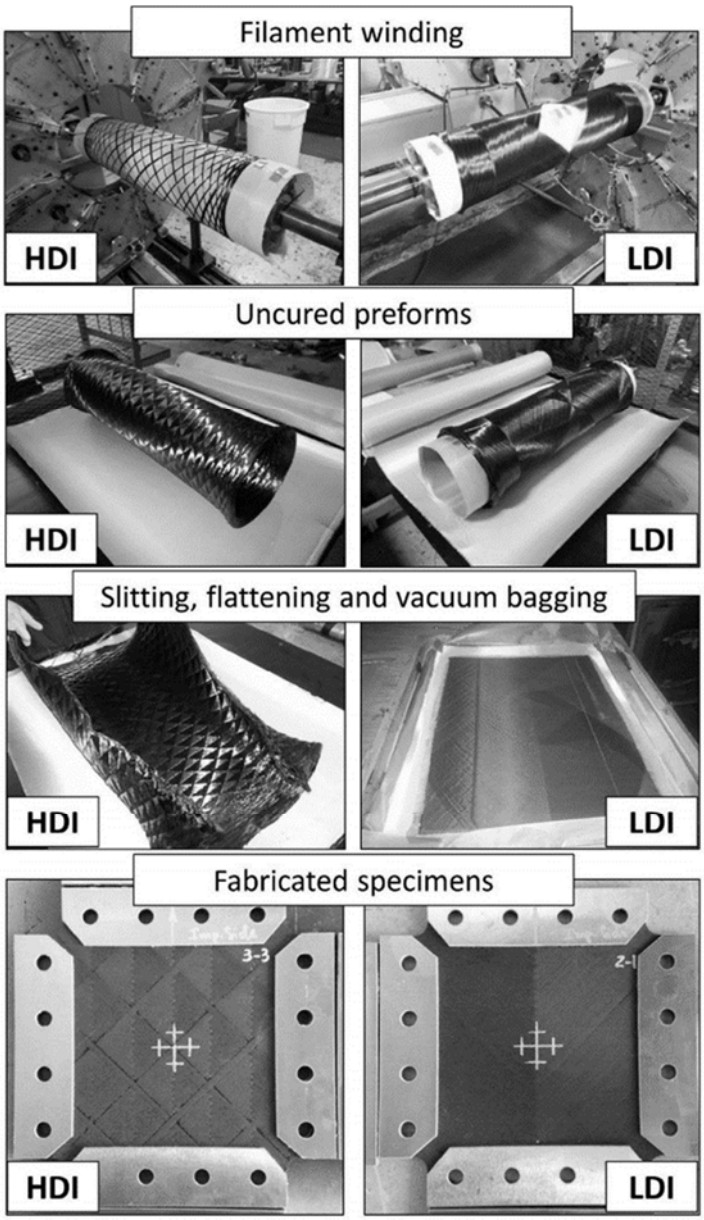

Fig. 6.2-9 Manufacturing of composite specimens

A test fixture was designed and manufactured in order to provide the following functionality: (1) Hold the external 0.8 mm-thick Al6061-T6 bumper, composite specimen, and witness plate during the hypervelocity impact tests; and (2) pre-load the composite specimens, when required.

Pre-loading was controlled by a strain gauge that was aligned with the direction of loading (see Fig. 6.2-10c). An additional strain gauge, installed in the direction perpendicular to loading, was used to control the value of Poisson ratio.

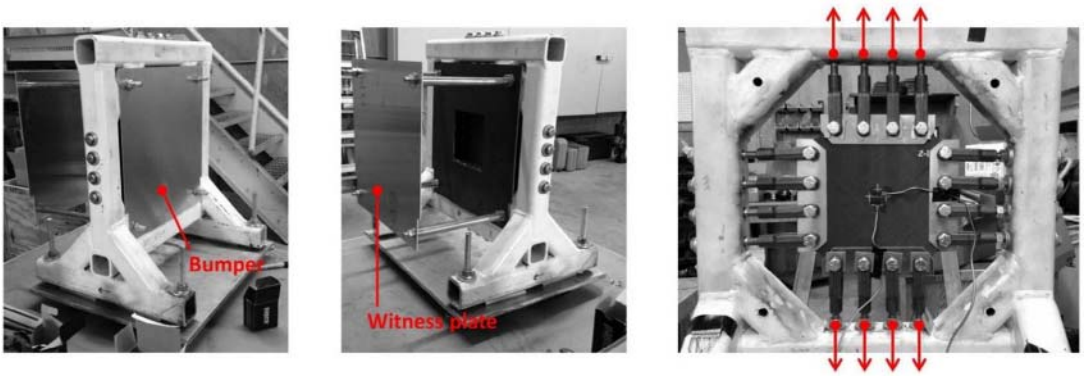

Fig. 6.2-10 Test fixture: a) front; b) back; c) specimen pre-loading

Table 6.2-2 summarizes the HVI test sequence, panel configuration, and as-tested projectile impact speeds for each test. In total, eight successful hypervelocity impact experiments were conducted with specimens of two different winding patterns (LDI and HDI), subjected to two different loading conditions (pre-loaded and not pre-loaded), and using two different projectile diameters (3.125 mm and 4.763 mm). The unidirectional pre-load stresses corresponding to the measured pre-load strains given in Table 6.2-2 were estimated using the classical lamination theory. They were found to be equal to 63 and 70 MPa for the LDI and HDI panels, respectively (the effective modulus of elasticity of the panels in the direction of loading is equal to 13 Gpa. All hypervelocity impact tests were conducted using a two-stage light gas gun at HIT Dynamics Ltd. impact testing facility (NB, Canada).

Table 6.2-2 Test parameters

Test #	Specimen #	Type	Pre-loading	Measured strain	Projectile diameter (mm)	Projectile mass (g)	Projectile velocity (km/s)
1	1-2	LDI	No	–	3.125	0.046	6.822
2	2-1	LDI	Yes	0.00483	3.125	0.046	6.828
3	3-2	HDI	No	–	3.125	0.047	6.847
4	4-2	HDI	Yes	0.00483	3.125	0.045	6.878
5	1-3	LDI	No	–	4.763	0.153	6.786
6	2-3	LDI	Yes	0.00540	4.763	0.156	6.786
7	4-3	HDI	No	–	4.763	0.154	6.922
8	3-3	HDI	Yes	0.00548	4.763	0.154	6.781

Following an impact test, each specimen was examined using the Immersion Automated Ultrasonic Testing (Immersion-AUT) technique, which can detect such defects as delaminations, large internal voids and large subsurface cracks by measuring the time-of-flight of the ultrasound signal sent through a composite panel. Resulting impact damage to panels with low- and high densities of interweaving of filament bands is represented in Fig. 6.2-11. Total damage zone areas were carefully measured from the C-Scan images using Adobe Photoshop tools. Results of these measurements are compared inFig. 6.2-12.

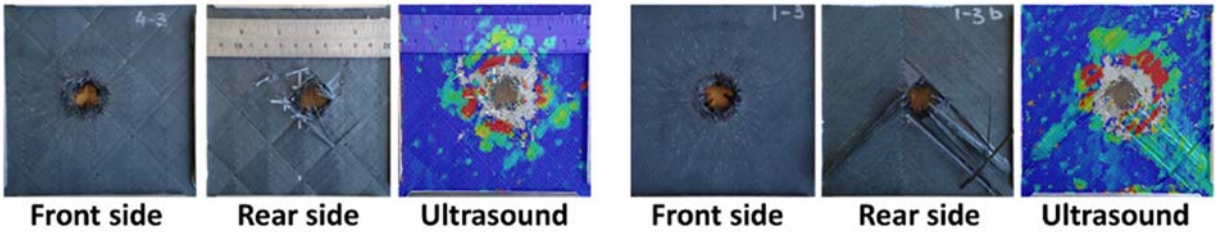

Fig. 6.2-11 HVI damage to a HDI composite (left) and a LDI composite panel (right)

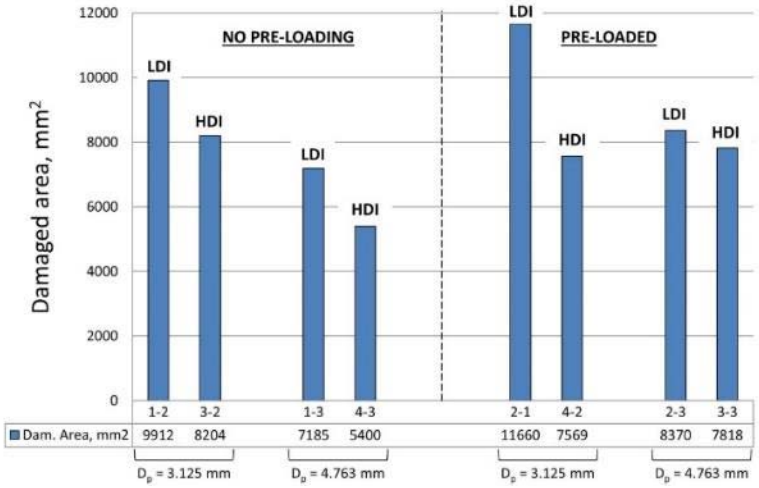

Fig. 6.2-12 Damaged area of the specimens determined from the C-Scan images

Conducted physical experiments revealed dependence of HVI damage of filament-wound composites on the particular winding pattern used in fabrication, as shown in Fig. 6.2-11. In the case of pattern with the high density of interweaving (HDI) of filament bands, a specimen inspection revealed a “containment” of the impact damage within the region restricted by 2x2 weave units adjacent to the perforated hole. In case of low density of interweaving (LDI), the specimen damage propagates outwards along the direction of the fibers, especially in the bottom left and bottom right directions. In most cases, pre-loading leads to formation of a larger damage zone.

Also, the filament-wound composites were subjected to optical microscopy (Fig. 6.2-13). It was found that the materials manufactured using filament winding contain two types of voids: voids internal to filament bands (analogous to inter-ply voids in laminated composites), and voids at the filament bands’ crossover regions. Voids of the latter type are believed to be an artifact of filament winding and may result in stress concentration at crossovers leading to formation of cracks and preliminary disintegration of the filament wound composite when subjected to static or impact loading. Higher density of crossovers leads to the higher density of such voids that may be a limiting factor for application of composites with high degrees of interweaving. Therefore, it should not be expected that simple increase of the density of interweaving in manufacturing will always result in higher damage tolerance of composite parts.

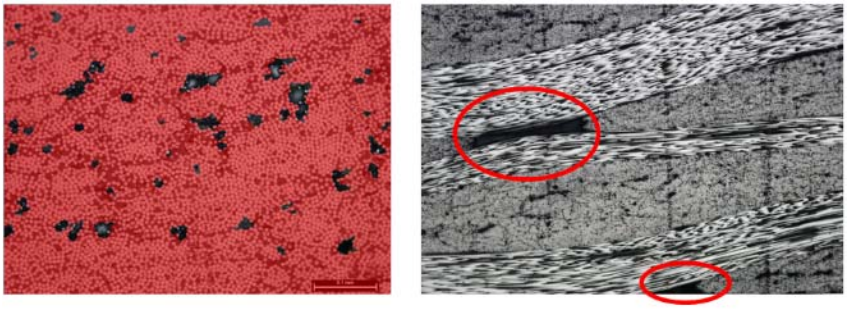

Fig. 6.2-13 Voids in the filament-wound composite: intra-band voids (left) and voids at the crossovers (right)

In the presence of the experimentally discovered complex dependence of HVI-induced damage on the filament winding pattern, the homogenization-based simulation techniques are inapplicable to this class of materials. Instead, a meso-scale modeling approach was used to represent the material structure in HVI simulations [6-24][6-25]. The meso-scale representation of the composite materials included explicit modeling of fiber-reinforced filament bands with ultrathin resin-rich regions between them and voids at crossover points (Fig. 6.2-14).

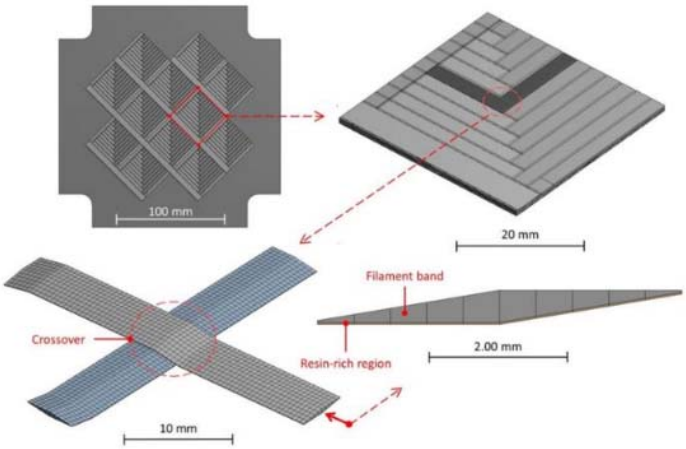

Fig. 6.2-14 Meso-scale modeling of the filament-wound composite

The modeling approach employed FEM in the Lagrangian formulation for composite panel and SPH method for parts that exhibited fragmentation, namely aluminum projectile projectiles and bumpers. Fig. 6.2-15 represents comparison of experimental and modeling results in terms of the damage to composite panels.

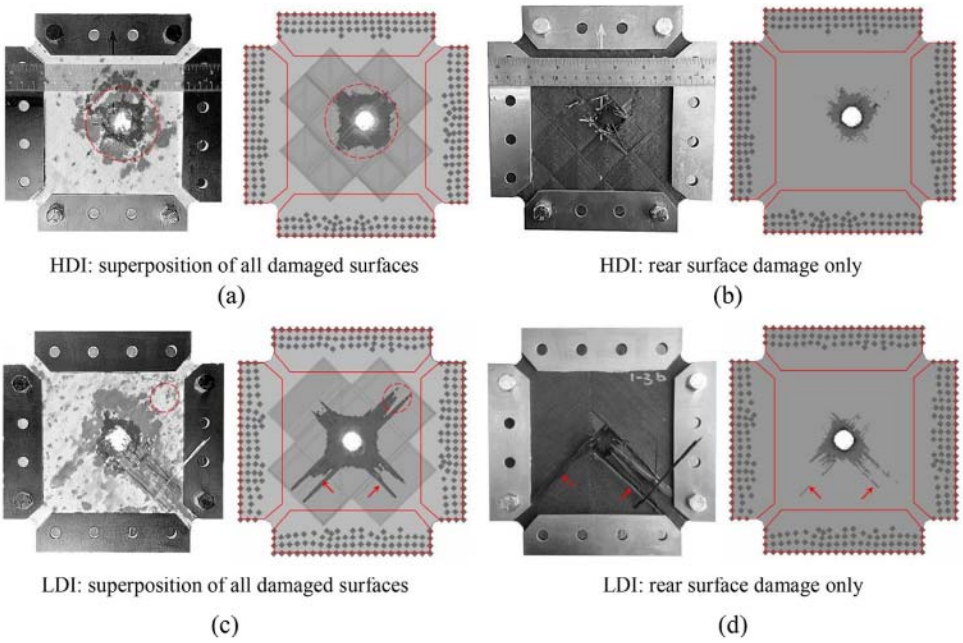

Fig. 6.2-15 Composite damage: comparison of experimental results and numerical predictions (top – HDI panel; bottom – LDI panel)

A comparison of experimental results and numerical predictions illustrates the ability of developed meso-scale modeling approach for capturing the main features of the HVI damage in the composites with different winding patterns. This approach can be used in the design of spacecraft filament-wound components, in order to determine the critical level of damage that is sustained due to orbital debris impacts.

6.3 Impact Experiments and Numerical Simulations / JAXA

6.3.1 Summary of Conditions and Results

JAXA has investigated the hypervelocity impact damage on a chassis wall of internal equipment behind a structure panel of a satellite. Fig. 6.3-1 shows the experimental conditions. To simulate a structure panel and an equipment chassis wall, a honeycomb sandwich panel was fixed on an aluminum alloy plate without spacing. According to the ESA MASTER model, alumina is the dominant material in submillimeter-size debris found in low earth orbit, and its average collision velocity relative to a spacecraft is about 10 km/s. However, advanced techniques are required to accelerate small solid projectiles up to 10 km/s. Therefore, this study used projectiles made from higher-density material to simulate the impact pressure caused by alumina projectiles at 10 km/s.

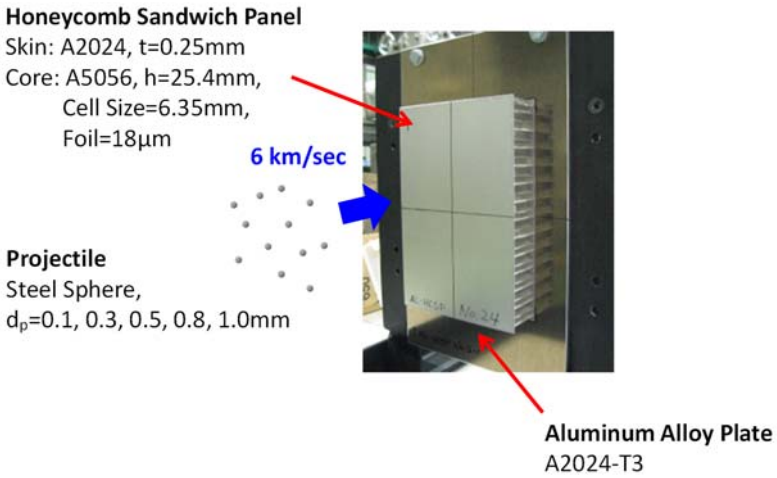

Fig. 6.3-1 Experimental conditions [6-27]

Crater depth on the aluminum alloy plate behind the honeycomb sandwich panel was expressed in the following empirical equation:

$$p < 2.18 d_p - 0.454 \qquad (6.3\text{-}1)$$

where p is the crater depth (mm) and d_p the projectile diameter (mm). From this equation, the critical projectile diameter causing perforation of the honeycomb sandwich panel was calculated as 0.21 mm.

By decreasing the thickness of the aluminum plate, perforation data was also obtained in addition to cratering data. The perforation includes detached spalling. The critical thickness of the aluminum alloy plate was estimated by the following equation:

$$t_c - = 4.91 d_p + 1.23 t_f - 1.06 \qquad (6.3\text{-}2)$$

where t_c is the critical thickness of the aluminum alloy plate (mm) and t_f the face sheet thickness of the honeycomb sandwich panel (mm).

6.3.2 Details

Many mission devices in unmanned spacecraft are generally set in an aluminum chassis. The chassis is installed inside of the structure, and fixed on a surface of a structure panel. If particles of debris pass through a structure panel without perforating a chassis wall, the debris impact will not affect electronic devices internally or the probability of mission success. To assess the vulunerability of unmanned spacecraft structures to debris impact, it is important to know the impact damage limit of a chassis wall behind a structure panel.

The tested target and setup are as described in the previous section. Hypervelocity impact experiments were performed using a two-stage light gas gun at ISAS/JAXA. Projectiles smaller than 0.5 mm were launched by using a scattershot method, where multiple projectiles were put into a sabot and then launched for impact on the target at almost the same velocity. By using this method, 10 to 20 impacts were obtained from a single shot.

The surfaces of the honeycomb sandwich panels and aluminum plates after the experiments were shown in Fig. 6.3-2. The impact of projectiles 0.15 mm in diameter caused little damage to the back face sheet of the honeycomb sandwich panel. Perforation of the back face sheet only occurred when multiple projectiles had impacted a honeycomb cell;

when only one projectile had impacted a cell, there was no perforation hole on the back face sheet. The honeycomb sandwich panel was perforated by projectiles larger than 0.3 mm in diameter. In cases of impact by 0.3 mm projectiles, clusters of small perforated holes were observed on the back face sheet. These clusters show that the projectile changed into a fragment cloud at impact on the front face sheet. The honeycomb sandwich panel is considered to function similar to a double-wall bumper shield, as the impact energy of projectiles was dispursed inside the panel.

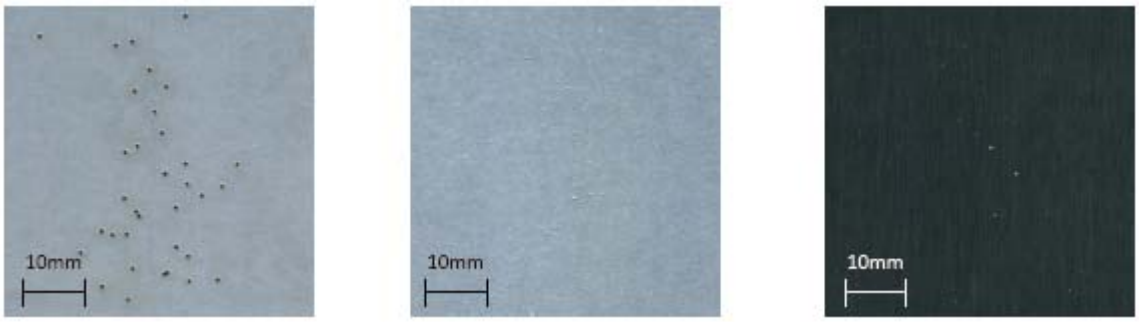

(a) Impacts of projectile 0.15 mm in diameter, impact velocity = 5.78 km/s

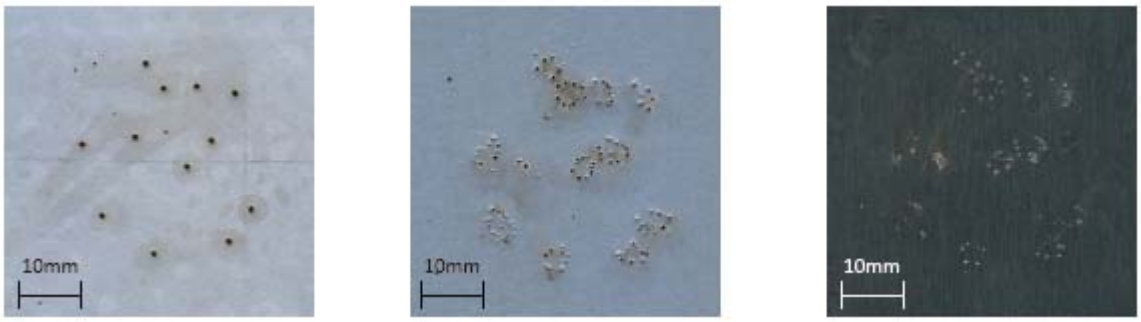

(b) Impacts of projectile 0.3 mm in diameter, impact velocity = 5.92 km/s

Fig. 6.3-2 Surfaces of the honeycomb sandwich panel and aluminum alloy plate after the impact experiments: (left) Front face sheet of the honeycomb sandwich panel, (center) Back face sheet of the honeycomb sandwich panel, (right) Impact surface of the aluminum alloy plate [6-28]

The tested honeycomb sandwich panels were examined by soft X-ray radiography. The results are shown in Fig. 6.3-3. The impacted honeycomb cells were deformed. A projectile 0.8 mm in diameter ruptured some honeycomb cells and also caused damage to adjacent cells. However, perforated holes on the back face sheet were only generated in areas under the impacted cells. To examine the effect of the honeycomb core, numerical simulations were performed. The face sheets were modeled as discs having sufficient size for simulation. To simplify the simulation, the honeycomb cell was modeled as a cylinder having the same diameter as the honeycomb cell size. The simulation result is shown in Fig. 6.3-4. The honeycomb cell walls interrupted expansion of the fragment cloud. Consequently, the impacts of the fragments were concentrated in a small area of the back face sheet. This simulation result is in good agreement with the X-ray radiographs. Thus, the honeycomb core is considered to increase the damage on the back face sheet as compared with a double-wall structure (without a honeycomb core).

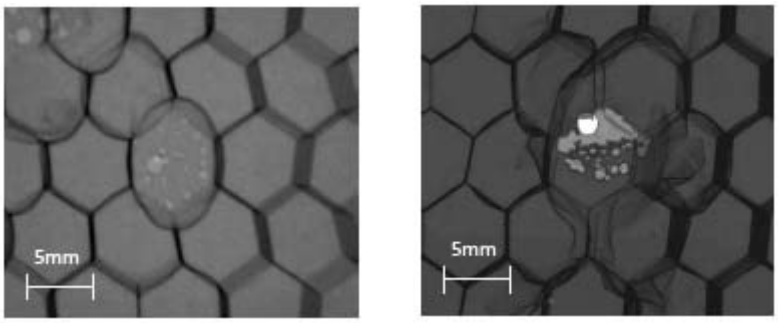

Fig. 6.3-3 Soft X-ray radiographs of tested honeycomb sandwich panels: (left) projectile diameter = 0.5 mm, impact velocity = 5.86 km/s, (right) projectile diameter = 0.8 mm, impact velocity = 5.71 km/s [6-28][6-28]

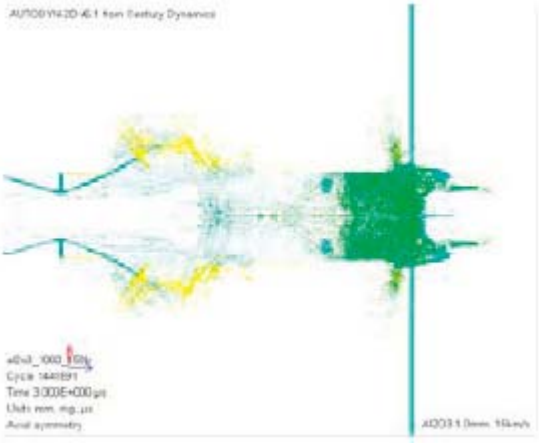

Fig. 6.3-4 Numerical simulation result of impact on the honeycomb sandwich panel [6-29]

The depths of craters on the aluminum alloy plate behind the honeycomb sandwich panel were measured using optical and laser microscopes. The maximum crater depth was obtained for each impact point. Fig. 6.3-5 shows the relationship between projectile diameter and crater depth. The craters created by multiple impacts on a single honeycomb cell are removed from the data. The impact energy was assumed to be proportional to the crater volume; the crater depth is thus proportional to the projectile diameter as the impact velocity, projectile density, and target density were almost constant. Therefore, the empirical equation (Eq.6.3-1) is obtained from Fig. 6.3-5. As the depth becomes 0 in this equation, the critical diameter is estimated to be 0.21 mm for the tested honeycomb sandwich panel.

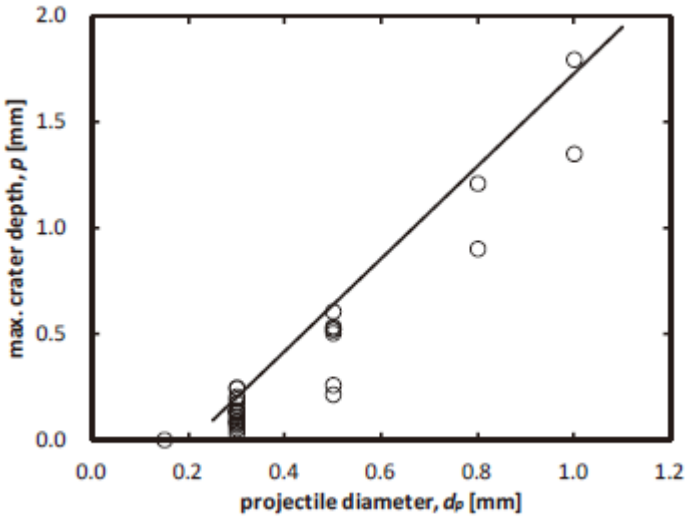

Fig. 6.3-5 Crater depth on the aluminum alloy plate behind the honeycomb sandwich panel [6-30][6-30]

The ballistic limit of a chassis wall behind a honeycomb sandwich panel was considered by using the crater depth equation. The surfaces of the aluminum plate after impact by a projectile 1.0 mm in diameter is shown in Fig. 6.3-6. Detached spall damage was observed on the back surface. The plate had been penetrated due to cratering and spalling. This result is considered almost the same as the ballistic limit of the aluminum alloy plate behind the honeycomb sandwich panel. To determine the ballistic limit, additional impact experiments had been performed on aluminum alloy plates of varied thickness. Fig. 6.3-7 shows the results. Crater depth in this graph indicates an assumed crater for an aluminum alloy plate having sufficient thickness for not causing spalling; the crater depth was thus calculated from Eq. 6.3-1. The dotted line is the estimated threshold of perforation. The ballistic limit of a chassis wall behind a honeycomb sandwich panel was expressed in Eq.6.3-2.

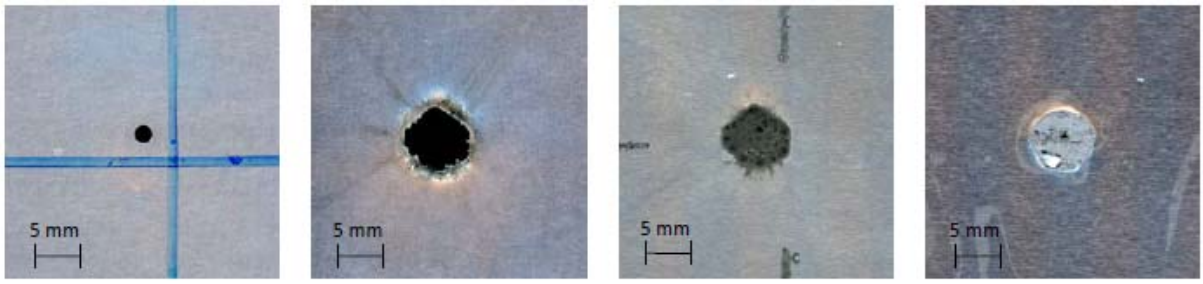

Fig. 6.3-6 Surfaces of the honeycomb sandwich panel and aluminum alloy plate after impact of a projectile 1.0 mm in diameter: (left) Front face sheet of the honeycomb sandwich panel, (center left) Back face sheet of the honeycomb sandwich panel, (center right) Impact surface of the aluminum alloy plate, (right) Back surface of the aluminum alloy plate [6-31]

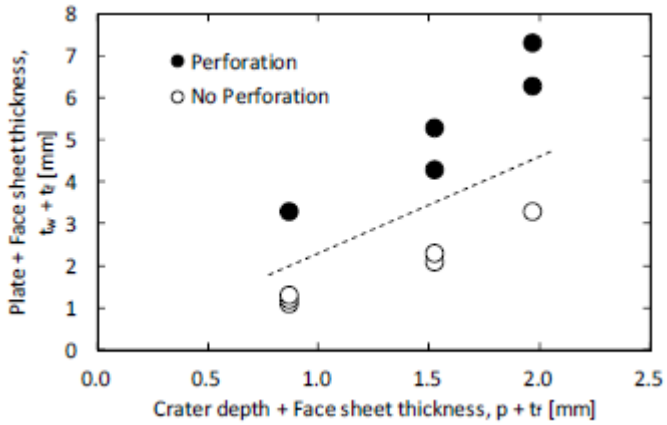

Fig. 6.3-7 Ballistic limit of the aluminum alloy plate behind the honeycomb sandwich panel [6-31]

6.4 References

[6-1] Gehring, J.W. (1970). Engineering considerations in hypervelocity impact. In: High-Velocity Impact Phenomena (Kinslow, ed.), Academic Press, New York, pp. 463-514.

[6-2] Pond, R.B., and Glass, C.M. (1970) Metallurgical observations and energy partitioning. In: High-Velocity Impact Phenomena (Kinslow, ed.), Academic Press, New York. pp. 420-461.

[6-3] Couque, H., O'Donoghue, P., Mullin, S., Kanninen, M. Investigation of crack initiation and unstable propagation due to meteoroid or orbital debris impact into Space Station Freedom pressure vessels. SwRI-NASA contractor report 64-00133; September, 1993.

[6-4] Lutz, B.E., Goodwin C.J.. Catastrophic failure modes assessment of the International Space Station Alpha. NASA Contractor Report 4720; February, 1996.

[6-5] Elfer N.C. Structural damage prediction and analysis for hypervelocity impacts – handbook. NASA Contractor Report 4706; February, 1996.

[6-6] Telichev, I., Prokhorov, A. G., Lukashev L. G. (1997) Residual toughness of spacecraft structural elements damaged by space debris, International Journal of Impact Engineering, 20, pp. 789-800.

[6-7] R. Sennett, R., Lathrop, B. (1968) Effects of Hypervelocity Impact on Honeycomb Structure, Journal of Spacecraft; 5(12), pp. 1496-1497.

[6-8] Jex, D.W., Miller, A.M., MacKay, C.A. The Characteristics of Penetration for a DoubleSheet Structure with Honeycomb, NASA Marshall Space Flight Center, Huntsville,
NASA TM X-53974,1970.

[6-9] Taylor, E.A., Herbert, M.K., Vaughan, B.A., McDonnell, J.A. (1999) Hypervelocity Impact on Carbon Fibre Reinforced Plastic/Aluminum Honeycomb: Comparison with Whipple Bumper Shields", International Journal of Impact Engineering; 23(1), pp. 883-893.

[6-10] Ryan, S., Schaefer, F.K., Destefanis, R., Lambert, M. (2008) A Ballistic Limit Equation for Hypervelocity Impacts on CFRP/Al HC Satellite Structures", Advances in Space Research; 41, pp. 1152-1166.

[6-11] Sibeaud, J-M., Thamie, C., Puillet, C. (2008) Hypervelocity Impact on Honeycomb Target Structures: Experiments and Modeling, International Journal of Impact Engineering, 35, pp. 1799-1807.

[6-12] Ryan, S., Hedman, T., Christiansen, E. (2010) Honeycomb vs. foam: Evaluating potential upgrades to ISS module shielding, Acta Astronautica, 67, pp. 818-825.

[6-13] Destefanis, R., Schaefer, F., Lambert, M., Faraud, M. (2006) Selecting enhanced space debris shields for manned spacecraft, International Journal of Impact Engineering, 33, pp. 219–230.

[6-14] Cherniaev, A., Telichev, I. (2016) Weight-efficiency of conventional shielding systems in protecting unmanned spacecraft from orbital debris, Journal of Spacecraft and Rockets, 54(1), pp. 75-89.

[6-15] Yew, C.H., Rodney, B.K. (1987) A study of damage in composite panels produced by hypervelocity impact. International Journal of Impact Engineering , 5, pp.729-738.

[6-16] Christiansen, E.L. (1990) Investigation of hypervelocity impact damage to space station truss tubes. International Journal of Impact Engineering,10(1), pp.125-133.

[6-17] Schonberg, W.P. (1990) Hypervelocity impact response of spaced composite material structures. International Journal of Impact Engineering,10, pp. 509-523.

[6-18] Silvestrov, V.V., Plastinin, A.V., Gorshkov, N.N. (1995) Hypervelocity impact on laminate composite panels. International Journal of Impact Engineering, 17(1), pp. 751-762.

[6-19] Lamontagne, C.G., Manuelpillai, G.N., Taylor, E.A., Tennyson, R.C. (1999) Normal and oblique hypervelocity impacts on carbon fibre/PEEK composites. International Journal of Impact Engineering, 23(1), pp. 519-532.

[6-20] Tennyson, R.C., Lamontagne, C. (2000) Hypervelocity impact damage to composites. Composites Part A, 31(1), pp. 785-794.

[6-21] Baluch, A.H., Park, Y., Kim, C.G. (2013) Hypervelocity impact on carbon/epoxy composites in low earth orbit environment. Compos Struct, 96(1), pp.554-560.

[6-22] White, D.M., Tylor, E.A., Clegg, R.A. (2003) Numerical simulation and experimental characterization of direct hypervelocity impact on spacecraft hybrid carbon fibre/Kevlar composite structure. International Journal of Impact Engineering, 29(1), pp. 779–790.

[6-23] Wicklein, M, Ryan, S., White, D.M., Clegg, R.A. (2008) Hypervelocity impact on CFRP: testing, material modelling, and numerical simulation. International Journal of Impact Engineering;35(1), pp. 1861–1869.

[6-24] Cherniaev, A., Telichev, I. (2014) Numerical simulation of impact damage induced by orbital debris on shielded wall of composite overwrapped pressure vessel, Applied Composite Materials, 21(6), pp. 861-884.

[6-25] Cherniaev, A., Telichev, I. (2015) Meso-scale modeling of hypervelocity impact damage in composite laminate, Composites part B: Engineering, 74, pp. 95-103.

[6-26] Cherniaev, A., Telichev, I. (2016) Experimental and numerical study of hypervelocity impact damage in composite materials fabricated by filament winding, *International Journal of Impact Engineering*, 98, 19-33.

[6-27] Higashide, M., Kurosaki, H., Hasegawa, S., Research Status and Action of Sub-millimeter Debris Impact Damage on Spacecraft Structure, Proc. 6th Space Debris Workshop, JAXA-SP-14-013, pp. 513-525, 2015.

[6-28] Higashide, M., Onose, N., Hasegawa, S., Evaluation of Space Debris Impact on Spacecraft Structure Panels, Trans. JSASS Aerospace Tech. Japan, Vol. 10, No. ists28, pp. Pr_1-Pr_6, 2012.

[6-29] Nitta, K., Higashide, M., Kitazawa, Y., Takeba, A., Katayama, M., Matsumoto, M., Response of an Aluminum Honeycomb Subjected to Hypervelocity Impacts, Procedia Eng., Vol. 58, pp. 709-714, 2013.

[6-30] Higashide, M., Onose, N., Hasegawa, S., Sub-millimeter Debris Impact Damage of Unmanned Spacecraft, Procedia Eng., Vol. 58, pp. 517-525, 2013.

[6-31] Higashide, M., Onose, N., Hasegawa, S., Submillimeter Debris impact Damage of Unmanned Spacecraft Structure Wall, Proc. 13th Japan International SAMPE Symposium and Exhibition, 2013.

7 MLI

7.1 Damage Mode

Debris larger than 1 mm can generally pass through a MLI blanket as the blanket consists of very thin layers less than 0.1 mm in thickness. Collision with debris produces a perforated hole on the outer layer of a MLI blanket. Then the perforated area is larger than the impacting debris. When the outer layer is made of polyimide film or fabric, cracking or peeling are often not observed around the hole. The debris itself is damaged and fractured as it passes through the reflective layers of the blanket. As a result, the damaged area on the blanket's inner layer will be larger than that on the outer layer. Due to the diffusion of debris impact energy, the MLI blanket can reduce damage on a shielded structure as compared with a bare structure. If large fragments of debris impact the blanket, peeling damage is observed in the inner layer. The fragments pass through the blanket and finally collide with a structure. In case of a close distance between the structure wall and the blanket, the inner layer is also damaged by the impact of ejecta fragments from the structure wall.

7.2 Impact Experiments and Numerical Simulations / JAXA

7.2.1 Summary of Conditions and Results

JAXA investigated the impact damage to MLI blankets caused by submillimeter-size debris. Table 7.2-1 lists the MLI blankets tested. For a hypervelocity impact experiment, each blanket was fixed on an aluminum alloy plate as shown in Fig. 7.2-1. As only its four corners were fixed on the plate, the blanket made rough contact with the aluminum alloy plate. According to the ESA MASTER model, alumina is the dominant material in submillimeter-size debris found in low earth orbit, and its average collision velocity relative to a spacecraft is about 10 km/s. However, advanced techniques are required to accelerate small solid projectiles up to 10 km/s. Therefore, this study used projectiles made from higher-density material to simulate the impact pressure caused by alumina projectiles at 10 km/s.

Table 7.2-1 Tested MLI blankets [7-1]

Target ID		MLI-I	MLI-II	MLI-III	MLI-IV	MLI-V
Weight (kg/m^2)		0.268	0.229	0.315	0.154	0.268
Outer film	Material	Single aluminized polyimide	Double aluminized polyimide	Single aluminized polyimide	Double aluminized polyimide	ITO coating aluminized polyimide
	Thickness	50 μm	25 μm	25 μm	25 μm	50 μm
Reflectors	Material	Double aluminized polyester				
	Thickness	6 μm	6 μm	12 μm	6 μm	6 μm
	Layers	10 ply	10 ply	10 ply	6 ply	10 ply
Inner film		Double aluminized polyimide, 25 μm				
Separators		Polyester mesh				

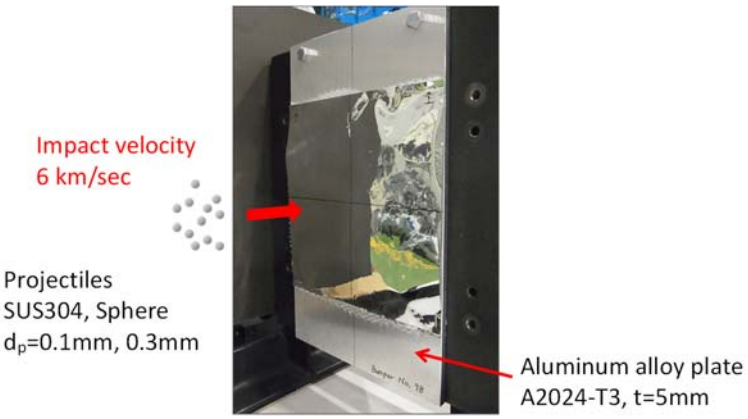

Fig. 7.2-1 Experimental conditions for the MLI blanket [7-1]

After the experiments, only MLI-III was not perforated by the impacts of projectiles 0.1 mm in diameter; all other blankets were perforated. In the experiments using projectiles 0.3 mm in diameter, all blankets were perforated. From a comparison of craters produced on the aluminum alloy plate, the MLI blankets were estimated to reduce impact energy by about 20%.

The ballistic limit of each high-strength fiber fabric was also investigated. The following fibers were tested: alamido fiber (Kevlar produced by DuPont), glass fiber covered with polytetrafluoroethylene (Beta produced by Saint-Gobain), and ceramic fiber (Nextel produced by 3M). Table 7.2-2 lists the properties of the tested fabrics. For the hypervelocity experiments, the fabrics were stacked and then set on an aluminum alloy plate as shown in Fig. 7.2-2. The top and bottom edges of the fabrics were fixed on the aluminum alloy plate. The total thickness of stacked fabrics was approximately 10 mm. Steel spheres were launched using a scattershot method. The impact velocity was about 6 km/s. The diameters of the projectiles were 0.15, 0.3 and 0.5 mm.

Table 7.2-2 Tested high-strength fiber fabrics [7-2]

Fabric ID	Fiber	Areal density (kg/m^2)	Thickness (mm)
Kevlar, normal	K29	0.319	0.43
Kevlar, high-modulus, thin	K49	0.058	0.08
Kevlar, high-modulus, thick	K49	0.217	0.33
Beta cloth, w/ aluminum	Beta	0.274	0.203
Beta cloth, w/o aluminum	Beta	0.274	0.177
Nextel, normal	Nextel 312	0.305	0.406
Nextel, normal, satin	Nextel 312	0.447	0.533
Nextel, hi-modulus, satin	Nextel 440	0.500	0.508

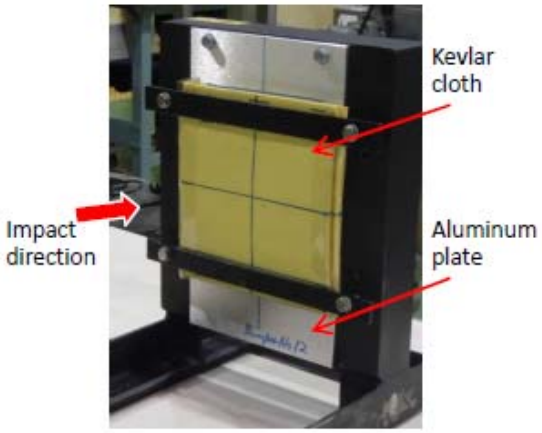

Fig. 7.2-2 Experimental conditions for the high-strength fiber fabrics [7-3]

To assess the protective capabilities of the fabric bumper shields, the perforated thickness of each shield was compared with a monolithic aluminum bumper as shown in Fig. 7.2-3. The vertical axis represents the perforated thickness of the fabrics divided by the thickness of an aluminum plate that can stop the same projectile. To also compare the bumper weight, the perforated thickness was converted to areal density. Fig. 7.2-4 shows a comparison of areal density. The high-strength fiber fabrics are considered to reduce bumper weight as compared with aluminum, but the total bumper thickness becomes thicker.

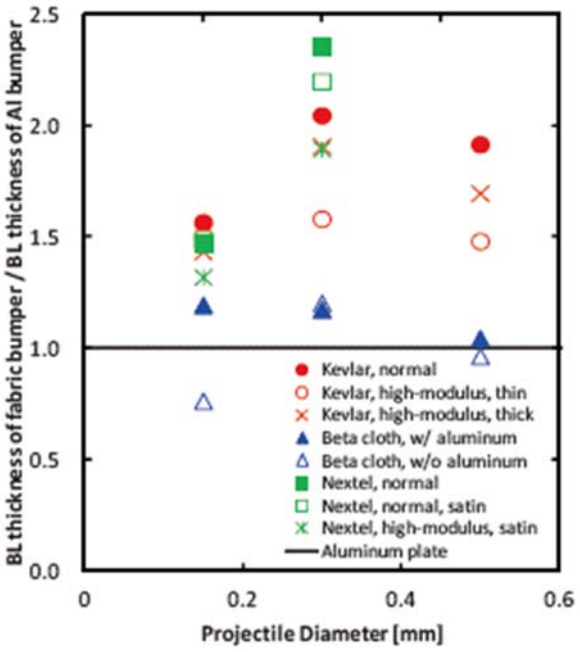

Fig. 7.2-3 Thickness of the fabric bumpers [7-2]

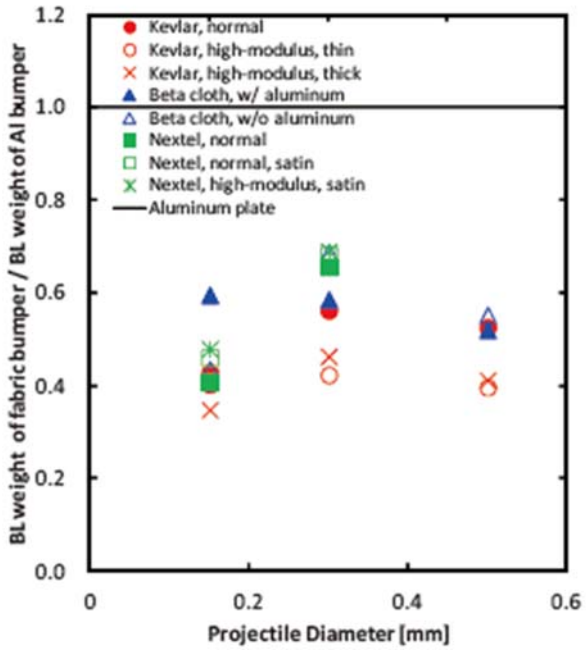

Fig. 7.2-4 Weight of the fabric bumpers [7-2]

7.2.2 Details

MLI blankets are normally installed on the outside of a spacecraft structure. JAXA investigated the shielding effect of MLI blankets against the impact of submillimeter-size debris. Typical MLI blankets installed on LEO satellites were chosen as specimens, as listed in Table 7.2-1. MLI-II is the standard blanket. MLI-I has the thickest outer film. MLI-III is the heaviest due to its thick reflectors. In contrast, MLI-IV is the lightest due to having about half the layers as the other blankets. MLI-V has coating on its outer film. Indium tin oxide (ITO) coating is used for maintaining the lower surface potential of a satellite. The MLI blanket was set for a hypervelocity experiment as shown in Fig. 7.2-1. The experiments were performed using a two-stage light gas gun at ISAS/JAXA. Projectiles were launched by using a scattershot method, where multiple projectiles were put into a sabot and then launched for impact on the target at almost the same velocity.

The results of experiments using projectiles 0.1 mm in diameter showed that only MLI-III (the heaviest specimen) was not perforated. Examples of perforated holes on the outer and inner films are shown in Fig. 7.2-5 and Fig. 7.2-6. In MLI-I, MLI-II and MLI-IV, the perforated holes became larger than those on the outer film. In contrast, groups of smaller holes were observed on the outer film of MLI-V. ITO coating apparently contributes to the fragmentation of a projectile.

ID	MLI - I	MLI - II	MLI - III	MLI - IV	MLI - V
Mark	Thick outer film	Standard	Thick reflectors	Half layers	ITO outer film
Outer film	Single Aluminized Polyimide, 50μm	Double Aluminized Polyimide, 25μm	Single Aluminized Polyimide, 25μm	Double Aluminized Polyimide, 25μm	ITO Coated Aluminized Polyimide, 50μm
Front surface	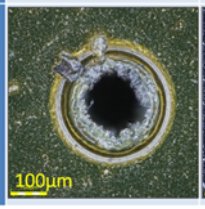	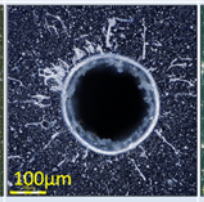	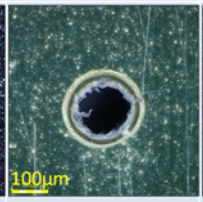	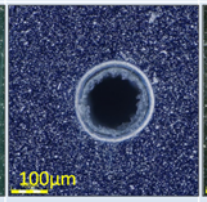	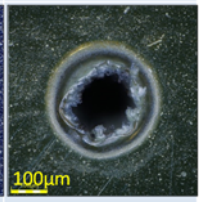

Fig. 7.2-5 Perforated holes on the outer films [7-1]

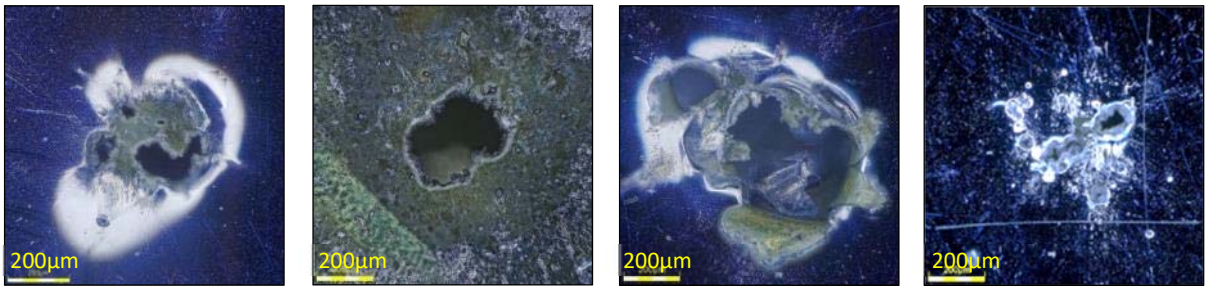

(a) MLI-I *(b) MLI-II* *(c) MLI-IV* *(d) MLI-V*

Fig. 7.2-6 Perforated holes on the inner films [7-1]

The projectiles 0.3 mm in diameter perforated all of the MLI blankets. The craters on the aluminum alloy plates behind the blankets were measured with an optical microscope. The measured crater volumes are shown in Fig. 7.2-7. The leftmost bar is a reference that indicates experimental results without using a MLI blanket. Comparing the results with or without a MLI, the average crater volume was approximately 20% smaller when using a MLI blanket. The crater volume is considered to correlate with impact energy. Therefore, MLI blankets are apparently effective in reducing impact energy by about 20%.

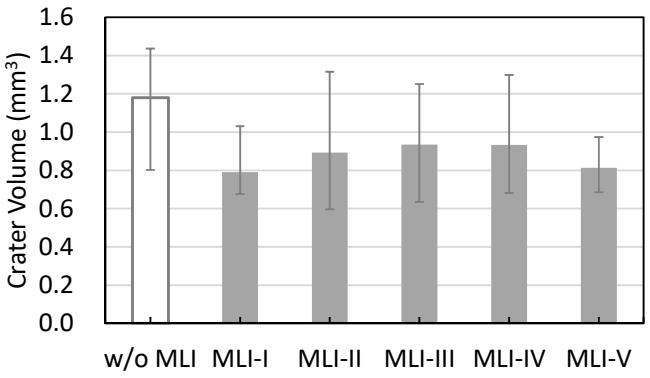

Fig. 7.2-7 Crater volumes on the aluminum alloy plate behind the MLI blanket [7-1]

High-strength Fiber Fabrics

Fabrics are useful as a debris bumper shield due to their shape flexibility in protecting complex-shaped satellite components. High-strength fiber fabrics are known to be effective for protection against hypervelocity impacts. These fabrics were employed as part of the Stuffed Whipple Bumper installed on the International Space Station. In order to assess the applicability of such fabrics for protection against submillimeter-size debris, JAXA investigated the ballistic limits of these high-strength fiber fabrics.

8 kinds of fabrics were tested, as listed in Table 7.2-2. For the fabrics made of Kevlar and Nextel fibers, high-modulus type fibers were also assessed. The tensile strength of both Kevlar fibers is approximately 3,000 MPa, but their tensile moduli are 71 GPa (K29) and 112 GPa (K49), respectively. Nextel 312 has tensile strength of about 1,700 MPa and tensile modulus of 150 GPa. Nextel 440 has a higher strength modulus than Nextel 312, with tensile strength of about 2,000 MPa and tensile modulus of 190 GPa. In Beta cloth, the fabric aluminized on one side was compared with that not aluminized.

The fabrics were stacked and installed in a test chamber as shown in Fig. 7.2-2. Hypervelocity impact experiments were performed using a two-stage light gas gun at ISAS/JAXA. Projectiles were launched by using a scattershot method. In the experiments for this study, the average impact numbers of projectiles per shot were 55.2 for 0.15 mm, 19.3 for 0.3 mm, and 8.3 for 0.5 mm, respectively. Steel spheres were employed as projectiles for the same reason as in the experiments for the MLI blankets.

Fig. 7.2-8 to Fig. 7.2-10 show examples of targets after the experiments. The projectiles perforated the 1st layers and then broke up. The fragment clouds were stopped in the middle layers.

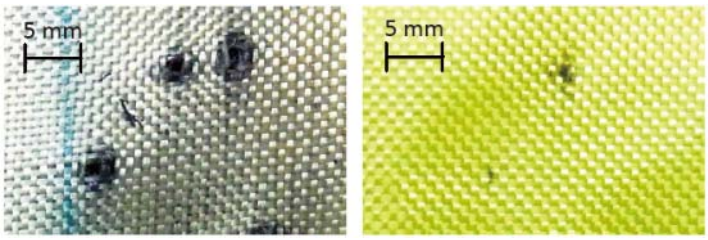

Fig. 7.2-8 Impacted Kevlar cloth (high modulus, thin), projectile diameter = 0.5 mm, impact velocity = 6.26 km/s [2]: (left) 1st layer, (right) 53rd layer

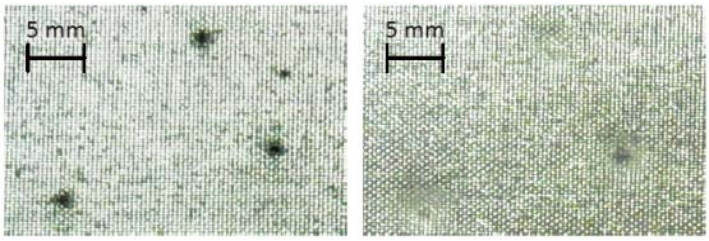

Fig. 7.2-9 Impacted Beta cloth (w/ aluminum), projectile diameter = 0.5 mm, impact velocity = 6.10 km/s [7-2]: (left) 1st layer, (right) 15th layer

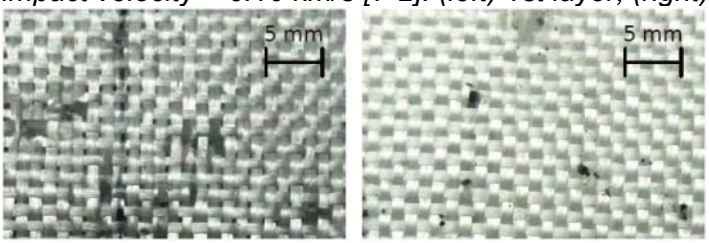

Fig. 7.2-10 Impacted Nextel cloth (normal), projectile diameter = 0.3 mm, impact velocity = 6.08 km/s [7-2]: (left) 1st layer, (right) 10th layer

In this study, the ballistic limit was defined as a damaged but non-perforated layer, as shown in Fig. 7.2-11. The ballistic limit was converted to thickness and weight by using those values of 1 ply, and then were normalized by thickness and weight of an aluminum plate that can stop the same projectile. The values of an aluminum plate were calculated from the ballistic limit equation by E. Christiansen in 2003. From the ballistic limit thickness and weight shown in Fig. 7.2-3 and Fig. 7.2-4, the thinnest bumper was Beta cloth and the lightest bumper was Kevlar cloth made from high-modulus fibers. The Beta cloth bumper had a thickness similar to that of an aluminum bumper, but its weight was approximately 60% that of aluminum. The fabrics made of lower density fibers reduced the bumper weight. The Kevlar cloth bumper needed twice the thickness compared to an aluminum bumper, but its weight was only 30% that of aluminum. The use of high-modulus fibers in Kevlar and Nextel was effective for producing thinner bumpers. Comparing the results of the Kevlar cloths made from high-modulus fibers, the total bumper thickness was decreased by stacking thinner fabrics.

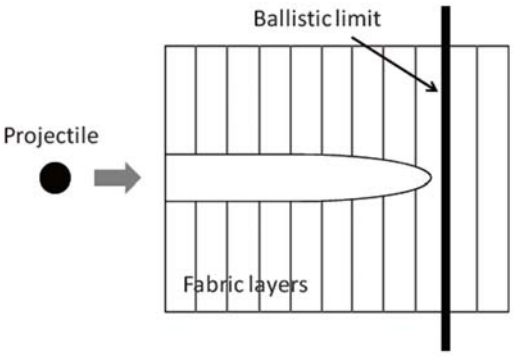

Fig. 7.2-11 Definition of ballistic limit [7-2]

Numerical simulation was also performed to obtain the ballistic limit curve of the Kevlar cloth. An alumina sphere was used as a projectile. The projectile diameter and impact velocity varied in the range of 0.01 - 2.0 mm and 1.5 - 15.0 km/s, respectively. The ballistic limits of Kevlar cloths stacked to 1, 5, and 10 ply were also investigated. Fig. 7.2-12 shows the simulation results. The ballistic limit curves were estimated based on the penetration depth measured from the non-perforation results. The curves showed good agreement in the range of high velocity.

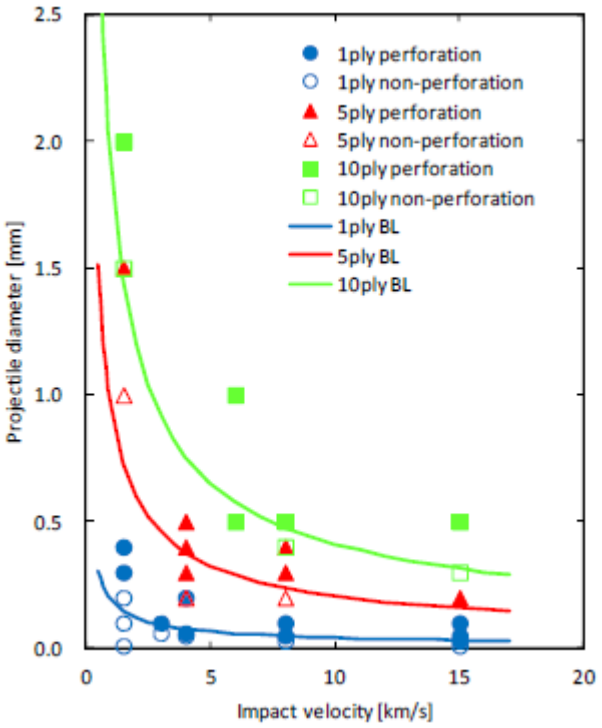

Fig. 7.2-12 Numerical simulation results for Kevlar cloths [7-3]

7.3 Impact Experiments and Numerical Simulations / NASA

Numerous mission support hardware systems and their spares are maintained outside of the habitable volume of the International Space Station (ISS), and are covered by a multi-layer insulation (MLI) thermal blanket which provides both thermal control and a measure of protection from micrometeoroids and orbital debris (MMOD).

The NASA Hypervelocity Impact Technology (HVIT) group at the Johnson Space Center in Houston Texas has assessed the protection provided by MLI in a series of hypervelocity impact tests using a 1 mm thick aluminum 6061-T6 rear wall to simulate the actual hardware behind the MLI. HVIT has also evaluated methods to enhance the protection provided by MLI thermal blankets. The impact study used both aluminum and steel spherical projectiles accelerated to speeds of 7 km/s using a 4.3 mm, two-stage, light-gas gun at the NASA White Sands Test Facility (WSTF).

7.3.1 Impact Experiments

Hypervelocity impact tests have been performed with aluminum and steel projectiles on several different combinations of MLI areal density and wall separation. The nominal MLI configuration has an outer and inner layer of Teflon coated glass fabric (beta cloth) and nineteen aluminized-polyimide reflective layers separated by twenty polyester mesh layers with a total areal density of 0.086 g/cm^2. The first four configurations use this MLI with separations of 50.8, 101.6 and 152.4 mm between the back of the MLI package and the front of the rear wall. These different shield configurations are arranged as shown in Fig. 7.3-1 where the separation, as marked, is varied for the configurations. A pre-impact photograph of a representative 152.4 mm experimental target is shown in Fig. 7.3-2.

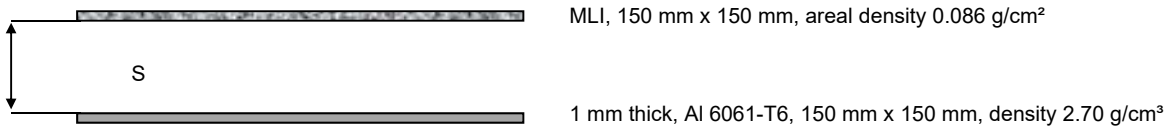

Fig. 7.3-1 MLI double wall shield

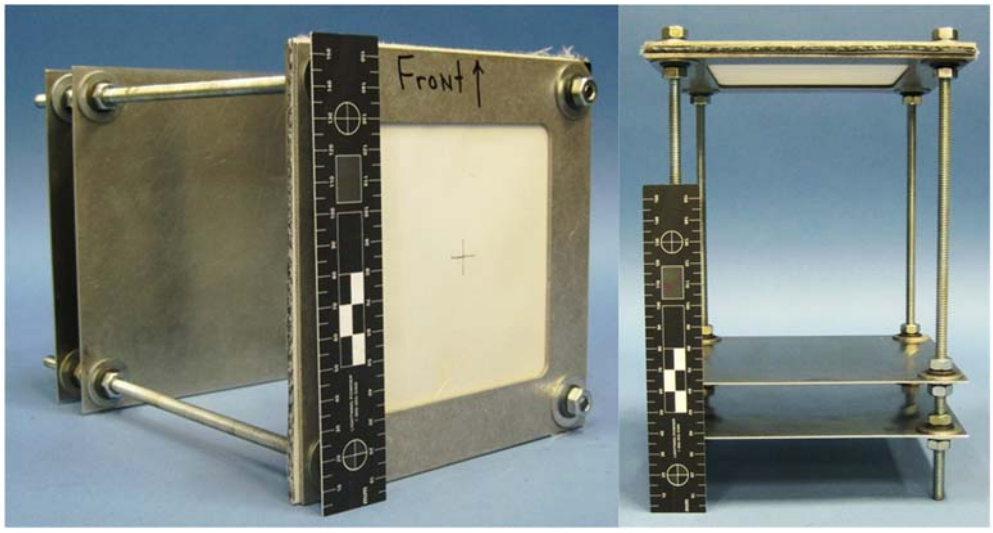

Fig. 7.3-2 Pre-impact photograph of a typical 152.4 mm configuration target

In addition to the nominal MLI package, another MLI configuration with the inner beta cloth layer removed resulting in an areal density of 0.059 g/cm^2 was also included in the test matrix. This modified MLI package was tested with the single separation distance of 50.8 mm between the back of the MLI and the front of the rear wall as shown in Fig. 7.3-3.

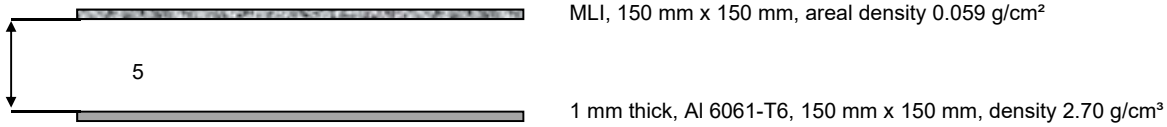

Fig. 7.3-3 Lightweight MLI double wall shield

7.3.2 Experimental Conditions and Results

The MLI experimental impact conditions are summarized in Table 7.3-1. Any detached spall or perforation of the Al 6061-T6 rear wall is considered a failure of the shield. Aluminum (Al 2017-T4) and stainless steel 440C spherical projectiles were used in the tests.

Table 7.3-1 MLI shield impact conditions

Test #	MLI Density (g/cm^2)	Wall Separation (mm)	Projectile Material	Projectile Diameter (mm)	Impact Obliquity (°)	Impact Speed (km/s)	Test Result
HITF11218	0.086	50.8	Al2017	1.0	0	7.00	Pass
HITF11224	0.086	152.4	Al2017	2.0	0	6.97	Fail
HITF11225	0.086	152.4	Al2017	1.8	0	6.91	Pass
HITF11227	0.086	101.6	Al2017	1.9	0	7.01	Pass
HITF11231	0.059	50.8	Al2017	1.2	0	6.99	Pass
HITF11232	0.059	50.8	Al2017	1.4	0	6.95	Fail
HITF11248	0.059	50.8	Al2017	1.3	0	7.00	Pass
HITF11273	0.086	50.8	Al2017	1.7	0	6.93	Fail
HITF13253	0.086	50.8	SS440C	0.8	45	7.06	Fail
HITF13254	0.086	50.8	SS440C	0.6	45	4.95	Fail
HITF13255	0.086	50.8	SS440C	0.8	0	6.82	Fail
HITF13256	0.086	50.8	SS440C	0.6	45	7.16	Pass
HITF13258	0.086	152.4	SS440C	1.0	0	7.11	Fail
HITF13259	0.086	152.4	SS440C	0.89	45	7.10	Fail
HITF13260	0.086	152.4	SS440C	0.6	45	4.46	Fail
HITF13261	0.086	152.4	SS440C	0.8	0	7.15	Pass
HITF13262	0.086	152.4	SS440C	0.7	45	6.42	Pass
HITF14001	0.086	50.8	SS440C	0.75	0	7.03	Pass

7.4 Recommendation for MMOD risk reduction

Toughened thermal blankets have been developed that greatly improve protection from hypervelocity micrometeoroid and orbital debris (MMOD) impacts as described by Christiansen and Lear in “Toughened Thermal Blanket for Micrometeoroid and Orbital Debris Protection”. This blanket arrangement can be used for significant improvement of MLI performance even when there is no separation between the MLI and the critical component. Three types of materials were added to the thermal blanket to enhance its MMOD performance: (1) disrupter layers, near the outside of the blanket to improve breakup of the projectile, (2) standoff layers, in the middle of the blanket to provide an area or gap that the broken-up projectile can expand, and (3) stopper layers, near the back of the blanket where the projectile debris is captured and stopped. Hypervelocity impact tests performed on the candidate toughened thermal blanket configurations at NASA WSTF and at the University of Dayton Research Institute showed significant improvement of MLI performance. From these tests the best disrupter materials was found to be beta cloth and fiberglass fabric. Polyimide

open-cell foams provide a light-weight means to increase the blanket thickness and improve MMOD protection. The best stopper material from these tests was Spectra™ 1000-952 and Kevlar™ KM2-705

7.5 References

[7-1] Higashide, M., Hirai, T., Kurosaki, H., Hasegawa, S., Matsumoto, H., Shielding Effect of MLI against Submillimeter Debris, Proc. 7th Space Debris Workshop, JAXA-SP-16-011, pp. 345-355, 2017.

[7-2] Higashide, M., Onose, N., Hasegawa, S., Ballistic Limit Thickness and Weight of High Strength Fiber Fabrics for Sub-Millimeter Steel Sphere Impact at 6 Km/s, Trans. JSASS, Aerospace Tech. Japan, Vol. 12, No. ists29, pp. Pr_1-Pr_5, 2014.

[7-3] Higashide, M., Nitta, K., Hasegawa, S., Onose, N., Matsuzawa, R., Takeba, A., Katayama, M., Ballistic Limit of Alamido Fiber Fabric Stacking for Sub-Millimeter Debris Impact, Proc. 6th European Conf. Space Debris, ESA SP-723, 2013.

[7-4] Christiansen, E. L. and Lear, D. M. “Toughened Thermal Blanket for Micrometeoroid and Orbital Debris Protection”, Procedia Engineering, **103**, 73-80 (2015).

8 Pressure Vessel

8.1 Damage Mode

With the unceasing development of space activities, the total number of space debris is ever increasing, which greatly threatens orbiting space vehicles. Spacecrafts often employ pressure vessels to contain gases and liquids. A pressure vessel subject to hypervelocity impact by meteoroids and space debris can represent a significant hazard to a space vehicle because of the energy stored within the vessel. Venting can occur to the vessel through the impact hole. Catastrophic rupture of the vessel can send high-velocity fragments in all directions and secondary debrisary damage becomes a serious threat to the spacecraft. The damage characteristic of pressure vessel by space debris and prediction of catastrophic failure are crucial aspects to shield structure design and risk evaluation of spacecraft in space debris environment.

In addition to the inherent gas, the catastrophic failure of a pressure vessel is mainly involves the following three mechanisms: the stress wave, the shock wave, and the debris cloud generated by hypervelocity impact. In this paper, the experiment and numerical simulation of the above three aspects are introduced.

8.2 Impact Experiments and Numerical Simulations / CNSA

8.2.1 Summary of Conditions and Results

Quite a few scholars from China and other countries are devoted to the research about gas filled pressure vessel under hypervelocity impact. The studies are mainly focused on the damage behavior characteristics and damage mechanism of the pressure vessel subject to hypervelocity impact. The research method is mainly based on the ground hypervelocity impact experiment, and numerical simulation is carried out using a variety of fluid codes.

Understanding the mechanism of processes produced by hypervelocity impact (debris cloud, gas shock wave, stress wave propagation) is the key to understand the damage mechanism of pressure vessels suffered by hypervelocity impact. Current research on the stress wave produced by hypervelocity impact of the pressure vessel is not enough, most of the studies do not take the influence of stress wave on the back wall of the pressure vessel into consideration. The propagation of stress wave in the pressure vessel wall is not clear. There are some results of the debris cloud formation and movement created by hypervelocity impact on pressure vessels. At present, the propagation law of shock wave caused by hypervelocity impact of gas filled pressure vessel has been basically understood.

8.2.2 Details

8.2.2.1 Propagation of stress wave in pressure vessel under hypervelocity impact

At present, there are few researches on the stress wave generated by hypervelocity impact on pressure vessel. Schäfer[8-1] did some research on the projectile impacting the cylindrical pressure vessel. The research points out that the elasticity stress wave generated by hypervelocity impact on pressure vessel could cause a penetration of the front wall within a short time; The compressible elastic wave travels along the wall of the pressure vessel with

little decay. The interference of the stress wave at the back wall may lead to the failure of pressure vessel.

8.2.2.2 The motion mechanism of debris cloud in pressure vessel

Debris cloud forms after a hypervelocity projectile impact and penetrat the front wall of a pressure vessel. N. N. Smirnov[8-2] provided a preliminary description of the debris cloud travelling in the pressure gas, the size and speed of particles in debris cloud as average. The results of the study pointed out that the friction between debris cloud and gas could lead to the liquefaction of the particles in front of the debris cloud.

F. Schäfer[8-3] analyzed the effect between debris cloud and gas in pressure vessel. The speed of the spherical projectile is 6.0~7.0 km/s, impacting small size spherical and cylindrical aluminum pressure vessel. It is found that instability expansion occurred in the back wall, and the debris cloud and the gas pressure are important factors to control the whole vessel damage.

Then, E. L. Christiansen[8-4] used the method of experiment to test response characteristics of pressure vessels under hypervelocity impact and the influence of different impact parameters to the damage mode of container. Research shows that catastrophic failure is caused from the back wall, the impact of the gas to the debris cloud is an important index to the damage of the back wall; due to the effect of the gas on the debris cloud, the increase of the gas pressure will not increase the catastrophic failure of the vessel.

In 2003, IGOR Y. TELITCHEV[8-5] from Canada used numerical simulation method to study the characteristics of the debris cloud generated after hypervelocity impact on pressure vessel. By Nigmatulin, he analyzed two-phase flow, and established a nonlinear hyperbolic partial differential equation group to characterize the interactions between debris cloud and gas. Based on the MacCormack method, he established the engineering calculation model of debris cloud velocity and shock wave pressure amplitude. The model and code could be used to design a pressure vessel and analyze its life.

Gai Fangfang and Pang Baojun from HIT[8-6][8-7][8-8] researched the debris cloud generated from the hypervelocity impact on the pressure vessel by numerical simulation based on the gas-solid-two-phase-flow theory. The interaction characteristics of debris cloud and gas medium are analyzed. Taking the factors such as projectile diameter, impact velocity and gas pressure into account, the characteristics of debris cloud motion are studied.

In 2014, Gai Fangfang[8-9] investigated the characteristics of debris clouds propagation inside the gas-filled pressure vessels for hypervelocity impact by SPH (Smoothed Particle Hydrodynamics) methods in AUTODYN-2D. The result showed that the venting time of vessels is related to“vacuum pole” in impact-axial direction. Gas pressure can reduce the damage of the debris clouds' impact on the rear wall vessels when the pressure value is in a certain range. And the comparison of debris cloud in vacuum and in 10.5MPa is shown in Fig. 8.2-1.

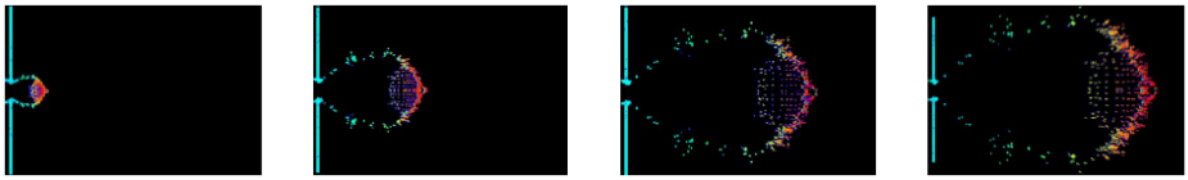

(a) pressure 0MPa

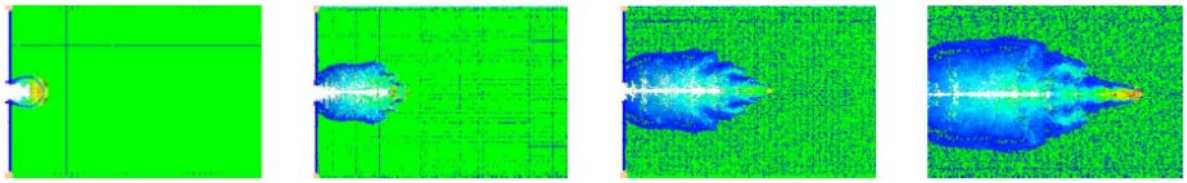

(b) pressure 10.5MPa

Fig. 8.2-1 Comparison of debris cloud[8-9]

In 2015, Pierre-Louis Héreil[8-10] investigated tanks which are CFRP (carbon fiber reinforced plastics) wrapped Al vessels. Explored internal pressure of nitrogen ranges from 1 bar to 300 bar and impact velocity are around 4400 m/s. Data obtained from X-ray radiographies and particle velocity measurements manifests the evolution of debris cloud and shock wave propagation in pressurized nitrogen. Observation of recovered vessels leads to the damage pattern and to its evolution as a function of the internal pressure. It is shown that the rupture mode is not a bursting mode but rather a catastrophic damage of the external carbon composite part of the vessel.

8.2.2.3 Characteristics of shock wave generated during hypervelocity impact on gas filled pressure vessel

Back in 1999, Telitchev[8-11] divided the gas shock wave motion into four stages which is generated during hypervelocity impact on gas filled pressure vessel as shown in Fig. 8.2-2: (1) the front wall perforation and intensive gas shock wave generated; (2) shock wave propagation and attenuation observed; (3) shock wave impacts the rear wall and reflects; (4) reflected shock wave impacts the front wall. The failure mode of the front wall and the rear wall is obtained by modeling and analyzing these four stages separately. The results show that the failure of the front wall is due to the shock wave reflected by the rear wall and gas pressure makes the crack unstable propagation; the rear wall failure is due to the impacting of debris cloud and shock wave. By increasing the gas pressure, the reflected shock wave intensity increases. The reflection shock wave is attenuated in the propagation of the front wall.

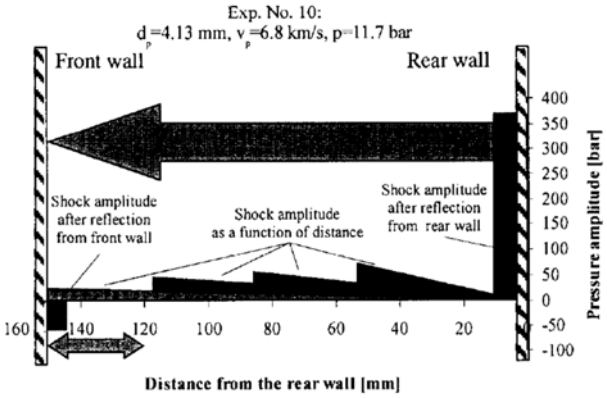

Fig. 8.2-2 The attenuation of the shock wave reflected by the rear wall [8-11]

In 2010, Gai Fangfang from HIT[8-6] established a model of the rear wall impacted by debris cloud generated by different projectile fragmentation patterns and gas shock wave. Critical conditions of therear wall penetration and the catastrophic failure are determined.

By using X-ray, Pierre-Louis Héreil[8-10] obtained the radiographies of the shock wave propagation in pressurized nitrogen. Observation of recovered vessels leads to the damage pattern and to its evolution as a function of the internal pressure. It is shown that the rupture mode is not a bursting mode but rather a catastrophic damage of the external carbon composite part of the vessel as mentioned above.

8.2.2.4 Failure of gas filled pressure vessel suffered by hypervelocity impact

The failure behavior of a gas filled pressure vessel suffered by hypervelocity impact is the result of stress wave, debris cloud impact, and the gas shock wave. The catastrophic failure of the gas filled pressure vessel is mostly due to the crack propagation of the rear wall.

In 2005, Telitchev[8-12] analyzed the burst conditions of pressure vessel under hypervelocity impact. A semi analytical model was adopted to describe the process of hypervelocity impact on pressure vessels, combined with nonlinear fracture mechanism analysis. The model could forecast the damage pattern and the critical conditions of catastrophic conditions. The model considers the pressure attenuation in the pressure vessel, and further analyzed the pressure value of the critical catastrophic failure of the vessel.

Zhang Yong from China Academy of Space Technology[8-13] presented hypervelocity impact characteristics and failure modes of the spherical pressure vessel (Fig. 8.2-3). The hole diameters under different projectile impact parameters were achieved according to the hypervelocity impact tests of unpressurized vessels (Table 8.2-1), then the ballistic limit diameter of projectile at a velocity 6.5km/s was analyzed. The hypervelocity impact tests of gas-filled pressurized vessels were also carried out to analyze the impact parameter leading to a catastrophic failure of the vessel. Finally, the prediction model of hole diameter was achieved by means of hypervelocity impact test data fitting, which provided reference for M/OD shielding design of spacecraft.

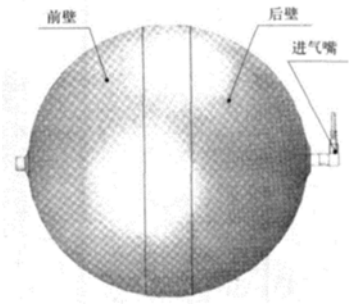

Fig. 8.2-3 The spherical pressure vessel[8-13]

Table 8.2-1 Test results of hypervelocity impact[8-13]

Test #	Projectile material	Projectile diameter(mm)	Impact velocity(km/s)	Gas pressure (MPa)	Vessel damage result	Hole diameter(mm)
1	LY12	1.76	6.58	0	No perforation	–
2		2.24	6.55	0	Perforation	2.46
3		2.52	6.62	0	Perforation	4.06
4		3.04	5.53	0	Perforation	5.00
5		4.98	6.39	0	Perforation	11.94
6		2.24	6.72	6	Perforation	2.00
7		9.04	6.48	6	Perforation	24.15

In 2012, Smirnova[8-14] researched the failure behavior of pressure vessel filled with liquid and gas. The study regards the interface of liquid and gas as a free surface. Due to the liquid phase, the kinetic energy of projectile is converted to the internal energy of the fluid phase, and the impact to the vessel rear wall by the projectile reduced.

In 2014, Ke Fawei[8-15] tested and simulated the characteristics of pressure vessel filled with water under hypervelocity impact. Parameters are listed in Table 8.2-2. The results showed that the main damage were perforation and burst for spherical pressure vessel filled with water under hypervelocity impact. The fragments generated by projectile impacting pressure vessel were decelerated evidently by the water which caused no evident damage on the back wall (Fig. 8.2-4, Fig. 8.2-5).

Table 8.2-2 Test parameters[8-14]

Test #	Vessel diameter(mm)	Vessel thickness(mm)	Projectile mass(g)	Impact velocity(km/s)
1	300	1.80	0.9936	2.46
2	300	1.80	1.0870	2.55
3	300	1.80	0.4990	2.45
4	200	0.55	0.9916	2.42

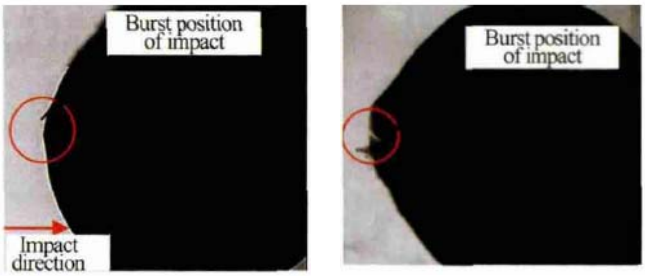

(a) T=0 (b) T=100 μs

Fig. 8.2-4 X ray image of impact time[8-14]

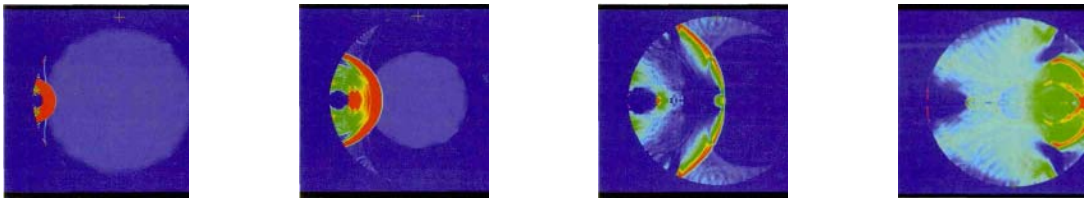

(a) T=0.02ms (a) T=0.05ms (a) T=0.1ms (a) T=0.2ms

Fig. 8.2-5 Simulation results of aluminum sphere impacting pressure container with inner diameter of 300mm[8-14]

During 2014 and 2015, Gai Fangfang[8-16][8-17] tested and simulated for the damage of pressure vessels' rear wall caused by hypervelocity impact. Firstly, tests of spherical projectiles hypervelocity impact on gas-filled pressure vessels were performed with a two-stage light gas gun loading technique, the damage characteristics of pressure vessels' rear wall were obtained. Experimental parameters and experimental results are shown in Table 8.2-3 and Fig. 8.2-6 to Fig. 8.2-8. Based on the linear-elastic fracture mechanics theory and the elastic mechanics theory, a simplified damage prediction model for pressure vessels' rear wall was built under different fragmentized patterns of projectiles. In the model, the rear wall was assumed to be a fixed circular plate, the debris cloud and gas shock wave were assumed to be uniform loads. The effectiveness of the model was verified through comparing the predicted results with test results. The critical condition for rear wall's perforation and crack, and the damage size under the action of debris cloud and gas shock wave were obtained. The critical condition for catastrophic rupture of rear wall considering the vessel wall's curvature effect was obtained.

Table 8.2-3 Comparison of prediction and experiment results of rear wall damage [8-17]

Test #	d	v	P	Prediction result	Experiment resutl	error
1	6.35	2.646	0.6	Crack size 21.4mm	Crack size 18.7mm	14.4
2	6.35	2.809	1.0	Crack size 23.0mm	Crack size 24.8mm	7.3
3	6.35	2.604	1.4	Crack size 25.2mm	Crack size 27.0mm	6.7
4	6.35	3.750	0.6	Crack size 41.4mm	Crack size 46.1mm	10.2
5	6.35	4.000	1.0	Crack size 40.0mm	Crack size 35.1mm	14.0
6	6.35	2.604	1.0	Crack size 20.8mm	Crack size 20.1mm	3.5
7	6.35	4.058	1.0	Destroy	Crack size 51.2mm	--
8	4.76	1.873	1.0	Perforation7.4mm	Perforation 7.3mm	1.4
9	4.76	2.193	1.0	Perforation 7.6mm	Perforation 7.6mm	0
10	6.35	3.301	1.0	Crack size 28.8mm	Crack size 31.0mm	7.1
11	3.97	2.100	1.0	Perforation 6.6mm	Perforation 7.4mm	10.8
12	6.35	3.700	1.4	Destroy	Crack size 54.2mm	--

d-projectile diameter(mm), v-impact velocity(km/s), P- gas pressure(MPa)

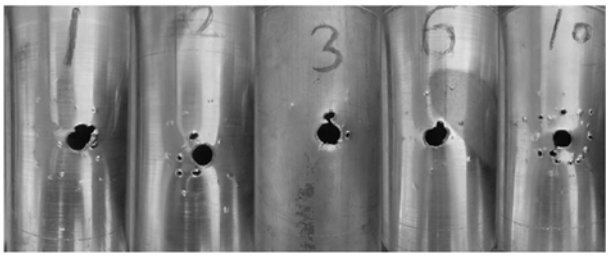

(a) NO.1 (b) NO.2 (c) NO.3 (d) NO.6 (e) NO.1

Fig. 8.2-6 Experiment results of pressure vessel damage in conditions of the projectile was not fragmentated

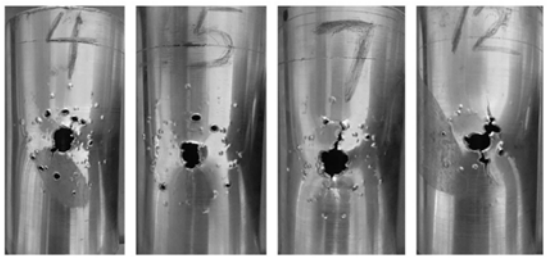

(a) NO.4 (b) NO.5 (c) NO.7 (d) NO.12

Fig. 8.2-7 Experiment results of pressure vessel damage in conditions of the projectile was completely fragmentated

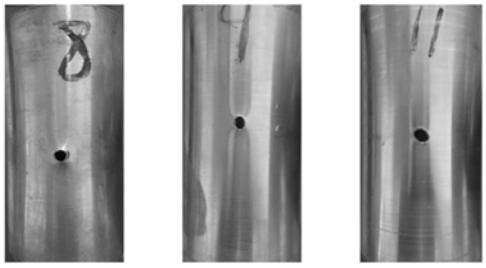

(a) NO.8 (b) NO.9 (c) NO.11

Fig. 8.2-8 Experiment results of pressure vessel damage in conditions of the projectile was not fragmentated

In 2015, William P. Schonberg and J. Martin Ratliff[8-18][8-19] presented a first-principles based model that has been developed to predict whether cracking might start or a through-crack might be created under an impact crater in a thin plate. This model was used to examine the effect of penetration depth on crack formation and whether the crack might grow through the tank wall thickness. The predictions of the model are compared to experimental data and show encouraging results. The paper also provides some suggestions for future work in this area, including the extension of the first-principles based model to include 3-D crack initiation modelling.

Recently, the research on hypervelocity impact of composite pressure vessel has been carried out, and it is found that the damage mode is closely related to the winding pattern of the composite fiber[8-20].

8.3 Impact Experiments and Numerical Simulations / EMI

To investigate failure modes and to determine failure threshold conditions of pressure vessels placed behind a satellite structure wall, simplified pressure vessels representative of equipment used onboard spacecraft were designed and built, as full space grade equipment was not available due to cost constraints [8-21]. The design of the high pressure vessels and the propellant tanks was very similar, both consisting of a ca. 1 mm thick Al liner. The difference was in the ca. 3 mm and 0.85 mm thick overwrapped CFRP layer, respectively, which was selected to comply with requirements for typical high-pressure vessels and propellant tanks, respectively. The outer diameter of the vessels was ca. 200 mm, the total length of the vessels including caps was 400 mm. The sandwich panel was the same as above (see Chapter “Cable”). To simulate propellant, the tanks were filled with water and

pressurized with nitrogen gas to 3 MPa. The high pressure vessels were inflated to 9 MPa with nitrogen gas.

Table 8.3-1 Wall composition of the pressure vessels in the cylindrical section

Pressure Vessel Type	CFRP thickness [mm]	Al thickness [mm]	Outer Diameter [mm]
High Pressure Vessel	2.9 ± 0.2	1.05 +0.35/–0.25	204.0 ± 1.1
Propellant Tank	0.85 ± 0.15	0.8 ± 0.3	200.0 ± 1.0

The configuration for a pressure vessel set-up behind a typical satellite structure wall is shown in Fig. 8.3-1.

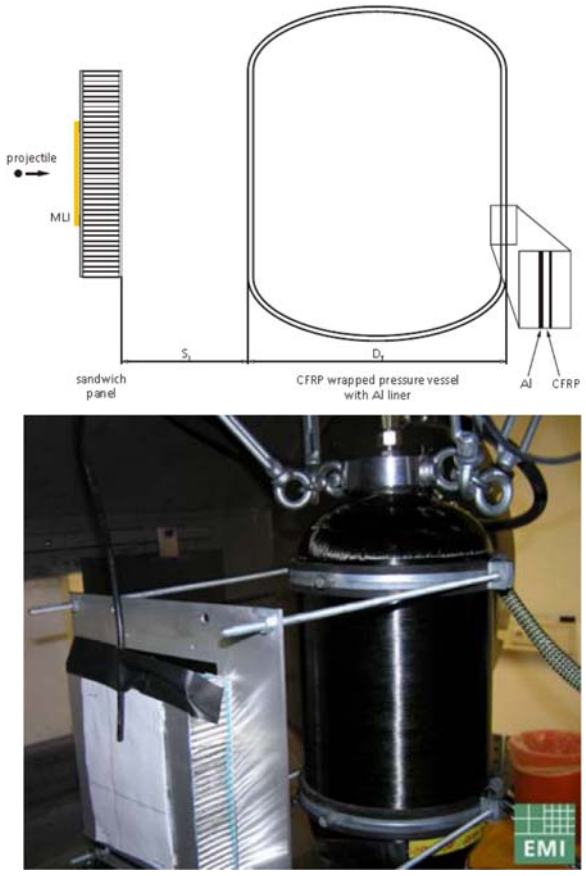

Fig. 8.3-1 Configuration for impact tests on pressure vessels.

In Table 8.3-2 and Table 8.3-3, the impact test results are listed. The high pressure vessels show leak-before-burst behaviour: At projectile velocity of ca. 3 km/s, the vessel wall is perforated from a projectile with a diameter of ca. 4 mm. Gas leaks but the vessel does not burst. At around 6.5 km/s, there is a transition from leakage-before-burst to catastrophic rupture (unzipping) at projectile diameters of between 5.0 and 6.0 mm (Fig. 8.3-2). As expected, the peak overpressure in the gas is rather low compared to the inflation pressure (not exceeding 10 % of P0). The effect of spacing on failure threshold could not be resolved from the few experimental test results available.

Table 8.3-2 Test parameters and test results of High Pressure Vessels (Gas-filled); meas. = measured, perf. = perforation

Exp.	S [mm]	v_0 [km/s]	d_P [mm]	P_0 [MPa]	ΔP_{Max} [MPa]	Overall result
4756	100	3.30	4.0	9	not meas.	perf., leakage
4759	100	2.26	4.0	9	0.4	no perf., pressure tight
4755	100	6.51	4.5	9	not meas.	no perf., pressure tight
4757	100	6.52	5.0	9	not meas.	perf., leakage
4754	200	6.51	6.0	9	0.9	perf., rupture, unzipping

Table 8.3-3 Impact tests on water-filled pressure vessels: Test parameters and test results

Exp.	S [mm]	v_0 [km/s]	d_P [mm]	P_0 [MPa]	ΔP_{Max} [MPa]	Overall result
4752	100	6.77	4.5	3	8.0	perf., leakage
4751	100	6.50	6.0	3	> 10	perf., rupture, no unzipping
4750	200	6.55	4.0	3	1.1	no perf., pressure tight

For the water filled vessels at ca. 6.5 km/s, there is a clear transition of failure mode "leakage-before-burst" to "catastrophic rupture" for projectiles of 4.5 mm diameter to 6.0 mm diameter. The underlying physical effect causing failure is hydrodynamic ram (Fig. 8.3-3). The recorded peak overpressure in the fluid exceeded the inflation pressure by at least a factor of three.

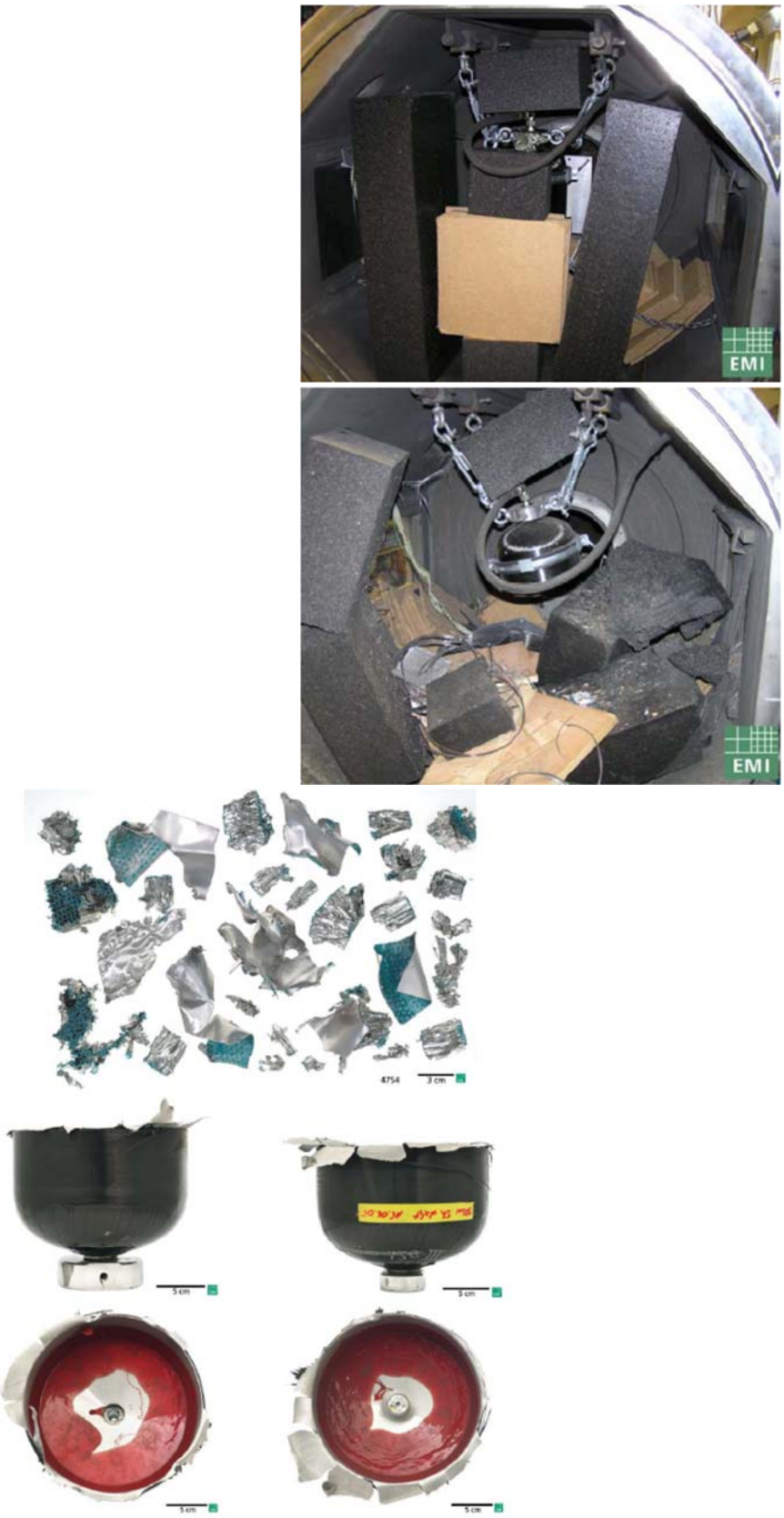

Fig. 8.3-2 (top) Target chamber before and after Exp. 4754. Catastrophically bursted pressure vessel of experiment 4754 (side and top view) and remnants of sandwich panel (center).

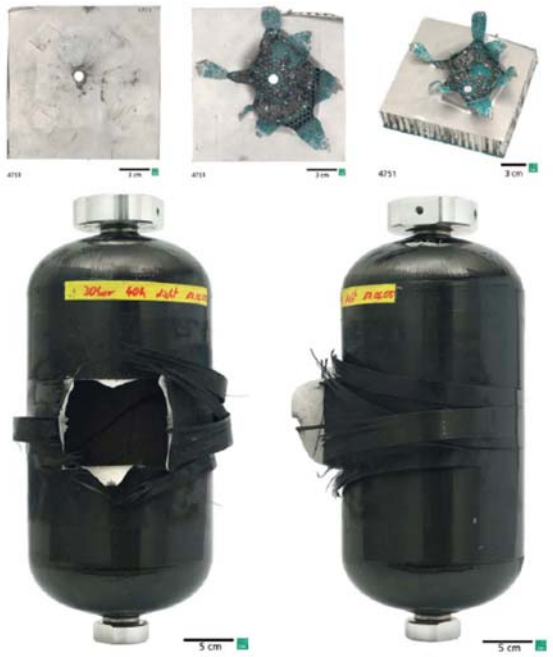

Fig. 8.3-3 Damage on pressure vessel of experiment 4750 (front and side views)

8.4 Recommendation for MMOD risk reduction

- Addition of protective materials on top of the vessel (high-strength fabrics etc.)
- Additional shielding between structure wall and vessel (e. g. stuffing from appropriate Kevlar/Nextel combinations)
- Additional shielding of the structure wall at the location of the vessel e. g. by external shields (such as protection enhanced MLI etc.)

8.5 References

[8-1] F. Schäfer. Hypervelocity impact testing impact on pressure vessels final report, 2001

[8-2] N. N. Smirnov, A. B. Kiselev, V. F. Nikitin. Fragmentations Caused by Hypervelocity Collisions of Debris Particles with Pressurized Vessels. Third European Conference on Space Debris, ESOC, Darmstadt, Germany, 2001

[8-3] F. Schäfer, E. Schneider, M. Lambert. Impact Fragment Cloud Propagation a Pressure Vessel. Acta Astronautica, 1997, 39(1): 31-40

[8-4] E. L. Christiansen, J. H. Kerr, J. P. Whitney. Debris Cloud Ablation in Gas-Filled Pressure Vessels. Int. J. Impact Engineering, 1997, 20: 217-228

[8-5] I. Y. TELITCHEV. Engineering model for simulation of debris cloud propagation inside gas-filled pressure vessels. Int. J. Impact Engineering, 2003, 29: 703-712

[8-6] Gai Fangfang. Prediction of damage and failure of gas-filled pressure vessels under space debris hypervelocity impact. Doctoral Dissertation of Harbin Institute of Technology, 2010 (盖芳芳. 空间碎片超高速撞击下充气压力容器破损预报. 哈尔滨工业大学博士论文, 2010)

[8-7] Gai Fangfang, Pang Baojun, Guan Gongshun. Model for the deceleration of secondary debris produced by hypervelocity impact on pressure vessels. Chinese

Journal of High Pressure Physics, 2012, 26(2): 177-184 (盖芳芳, 庞宝君, 管公顺.超高速撞击充气压力容器二次碎片减速运动建模研究. 高压物理学报, 2012, 26(2): 177-184)

[8-8] Gai Fangfang, Pang Baojun, Guan Gongshun. Quasi-static bursting analysis of gas-filled pressure vessels on the front side under hypervelocity impact. Chinese Journal of High Pressure Physics, 2011, 25(1): 48-54 (盖芳芳, 庞宝君, 管公顺. 空间碎片超高速撞击充气压力容器前壁准静态破坏分析. 高压物理学报, 2011, 25(1): 48-54)

[8-9] Liu Xun, GAI Fangfang, XING Hualu. Numerical Simulation on the Characteristics of Debris Clouds Produced by Hypervelocity Impact on Pressure Vessels. 2014 8th International Conference on Future Generation Communication and Networking

[8-10] Pierre-Louis Héreil, Jérome Mespoulet, Fabien Plassard. Hypervelocity Impact of Aluminum Projectiles Against Pressurized Aluminum-Composite Vessel. Procedia Engineering, 2015(103) : 181-188

[8-11] I. Y. TELITCHEV. Analysis of the fracture of gas-filled pressure vessels under hypervelocity impact. International Journal of Impact Engineering, 1999, 23: 905-919

[8-12] I. Y. Telitchev. Analysis of Burst Conditions of Shielded Pressure Vessels Subjected to Space Debris Impact. Journal of Pressure Vessel Technology, 2005, 127: 179-183

[8-13] Zhang Yong, Huo Yuhua, Han Zengyao, Li Ming Huang Jie. Experimental of gas-filled pressure vessel under hypervelocity normal impact. Chinese Space Science and Technology, 2009, 29(1): 56-60 (张永, 霍玉华, 韩增尧等. 卫星高压气瓶的超高速撞击试验. 中国空间科学技术, 2009, 29(1): 56-60)

[8-14] M. N. Smirnova, K.A. Kondrat'ev. Space debris fragments impact on multi-phase fluid filled containments. Int. J. Acta Astronautica 79 (2012) 12–19)

[8-15] Ke Fawei, Zhou Zhixuan. Test and simulation study on characteristics of pressure container filled with water under hypervelocity impact. Journal of Experiments in Fluid Mechanic. 2014, Jun, Vol. 28, No. 3 (柯发伟，周智炫，黄洁. 充水压力容器超高速撞击特性试验与仿真研究. 实验流体力学，2014, Jun, Vol. 28, No.3)

[8-16] Gai Fangfang, HAO Juncai. Analysis of Damage of Gas-Filled Pressure Vessels' Rear Wall Subjected to Spherical Projectiles Hypervelocity Impact. Proceedings of China Conference on Computational Mechanics and Qian Lingxi prize in Computational Mechanics, 2014 (盖芳芳, 郝俊才, 乔牧. 球形弹丸超高速撞击充气压力容器后壁损伤分析. 中国计算力学大会暨钱令希计算力学奖颁奖大会论文集, 2014)

[8-17] Gai Fangfang, Cai Yuan. Tests and modeling for damage of pressure vessels' rear wall caused by hypervelocity impact. Journal of Vibration and Shock, 2015 (13) Vol. 34 (盖芳芳, 才源, 郝俊才, 乔牧. 超高速撞击压力容器后壁损伤实验及建模研究. 震动与冲击，2015 (13) Vol. 34)

[8-18] William P. Schonberg, J. Martin Ratliff. A First-Principles-Based Model for Crack Formation in a Pressurized Tank Following an MMOD Impact. Procedia Engineering, 2015 (103) 546-552

[8-19] William P.Schonberg, J.MartinRatliff. Hypervelocity impact of a pressurized vessel: Comparison of ballistic limit equation predictions with test data and rupture limit equation development. Acta Astronautica, 2015 (115)400-406

[8-20] Garcia, M. A, Davis, B. A., Miller, J. E.. Development of a numerical model of a hypervelocity pressurized composite overwapped pressure vessel. 14th Hypervelocity Impact Symposium, April 24th-28th, 2017, University of Kent, Canterbury, UK

[8-21] Schäfer F., Putzar R., Lambert M. (2008). Vulnerability of Satellite Equipment to Hypervelocity Impacts. 59th International Astronautical Congress. Glasgow, Scotland.

9 Transparent Materials

Transparent materials are used for viewports in crewed vehicles, and as covers and lens for instruments on spacecraft of all types. These materials can be made of glass or ceramics with brittle characteristics, or polymers with ductile properties. As a consequence of the different material types used for applications of transparent materials, their response to hypervelocity impact from micrometeoroid and orbital debris (MMOD) particles varies considerably.

NASA's Hypervelocity Impact Technology (HVIT) group has evaluated the ballistic response of a number of transparent materials including fused silica glass, quartz glass, soda-lime glass, Chemcor tempered glass, aluminum oxynitride (ALON™), spinel, polycarbonate (Hyzod™), acrylic, and lithium-aluminosilicate glass-ceramic (Zerodur™). There are many more transparent materials. Two materials will be discussed below as typical examples used on the ISS and other spacecraft (fused silica glass and Hyzod polycarbonate).

9.1 Damage Mode

Typical damage modes of interest are (1) craters of a given diameter or depth, (2) crater with detached spall from the back side of the transparent material, (3) complete penetration or perforation of the transparent material. In some cases, the extent of cracking in the material is of interest (depth and length of the cracks) because the transparent material is subject to stress due to loading, and the cracks may grow to cause complete failure of the material.

Target size and mounting conditions can influence test results, especially for brittle targets. NASA will typically use rubber gasket materials between the glass and target frames to avoid metal to glass contact which can result in damage to the glass during hypervelocity tests. Also, edge effects become significant as target size is decreased, which results in increased target damage for brittle targets. There is a further complication that can occur from impact shock/elastic waves that reflect from the edges of a target and can focus in an area of the target causing damage to the target especially for brittle targets [9-1]. In NASA tests, it is usual practice to not test at the direct center of a circular glass target, because the reflected waves from the edges will focus at the center of the target causing more damage than would be the case if the impact occurred anywhere else on the target but the exact center.

9.2 Impact Experiments and Numerical Simulations / NASA

9.2.1 Impact Experiments on Fused Silica Glass

Parameters and results from NASA impact tests that resulted in craters to fused silica glass are given in Table 9.2-1 [9-1][9-2]. The targets in these tests were circular fused silica disks that are 1.7cm thick and typically 7.6cm diameter. Tests with larger impactors (usually 1mm or larger) are conducted on 25cm diameter fused silica disks. These fused silica targets were cored from flown Shuttle thermal panes (the outer pane of Shuttle windows is the thermal pane). Results from tests with larger projectiles resulting in either perforation or spall are reported elsewhere [9-3].

Table 9.2-1 NASA test results on fused silica glass

Test Number	Projectile Diameter (cm)	Proj. Density (g/cm^3)	Velocity (km/s)	Impact Angle (deg)	Normalized Velocity (km/s)	Crater Depth (cm)	Front Surface Spall Diameter (cm)
1	0.04	2.80	6.88	0	6.88	0.125	1.81
2	0.04	2.80	6.93	0	6.93	0.112	1.76
3	0.04	2.80	6.69	30	5.79	0.125	1.59
4	0.04	2.80	6.69	45	4.73	0.067	1.48
5	0.04	2.80	6.91	60	3.46	0.045	0.97
7	0.04	2.80	6.48	0	6.48	0.113	1.99
8	0.04	2.80	6.29	45	4.45	0.082	1.49
9	0.04	2.80	5.24	0	5.24	0.101	1.55
10	0.04	2.80	5.38	45	3.80	0.058	1.05
11	0.04	2.80	5.71	60	2.86	0.054	0.567
12	0.04	2.80	4.55	0	4.55	0.1	1.43
13	0.04	2.80	5.00	45	3.54	0.074	1.29
14	0.04	2.80	5.66	0	5.66	0.087	1.84
15	0.04	2.80	4.48	45	3.17	0.053	0.96
16	0.04	2.80	4.63	60	2.32	0.05	0.75
17	0.04	2.80	3.87	0	3.87	0.05	0.57
20	0.04	2.80	3.50	45	2.47	0.036	0.725
21	0.04	2.80	3.56	60	1.78	0.036	0.64
24	0.04	2.80	2.97	0	2.97	0.042	0.9
25	0.04	2.80	2.79	45	1.97	0.029	0.67
26	0.04	2.80	2.56	60	1.28	0.023	0.47
27a	0.06	2.80	6.97	0	6.97	0.182	3.05
28a	0.08	2.80	6.59	0	6.59	0.278	3.77
29a	0.1	2.80	6.82	0	6.82	0.251	4.34
30a	0.16	2.80	6.82	0	6.82	0.35	8
31	0.06	3.99	6.62	0	6.62	0.163	3.25
32a	0.08	3.99	6.85	0	6.85	0.223	4.25
34	0.04	7.84	6.74	0	6.74	0.15	2.7
35	0.04	7.84	6.78	45	4.79	0.143	2.72
37	0.04	3.99	6.74	45	4.77	0.116	2.1
38a	0.04	8.55	6.87	0	6.87	0.167	3.9
40	0.1	1.11	6.75	0	6.75	0.129	3.2
41a	0.1	1.11	6.76	45	4.78	0.157	2.6
52	0.1	1.11	5.82	0	5.82	0.122	2.63
53	0.1	1.11	5.85	45	4.14	0.104	2.7
58	0.04	7.84	5.23	0	5.23	0.119	1.92
59a	0.04	7.84	4.99	45	3.53	0.179	1.8
60	0.04	3.99	4.83	0	4.83	0.08	1.5
61a	0.04	3.99	4.94	45	3.49	0.15	1.6
62	0.04	8.55	4.9	0	4.90	0.132	2
63	0.04	8.55	5	45	3.54	0.112	2.2
64	0.1	1.11	5.02	0	5.02	0.122	2.4
65	0.1	1.11	5	45	3.54	0.105	2.4
70	0.04	7.84	4.12	0	4.12	0.107	1.29
71a	0.04	7.84	4.11	45	2.91	0.102	1.1
72	0.04	3.99	3.9	0	3.90	0.068	1.26
73	0.04	3.99	3.97	45	2.81	0.063	1.1

74	0.04	8.55	3.47	0	3.47	0.093	0.96
75a	0.04	8.55	3.71	45	2.62	0.138	1.58
76	0.1	1.11	4	0	4.00	0.087	3.04
77	0.1	1.11	4.1	45	2.90	0.076	2.8
82a	0.04	7.84	3.27	0	3.27	0.086	0.9
83	0.04	7.84	2.82	45	1.99	0.082	0.8
84	0.04	3.99	3.08	0	3.08	0.055	1
85	0.04	3.99	3.1	45	2.19	0.085	0.9
86	0.04	8.55	3.02	0	3.02	0.08	1.2
87	0.04	8.55	2.94	45	2.08	0.135	1.3
88	0.1	1.11	3.15	0	3.15	0.078	2.6
89	0.1	1.11	2.91	45	2.06	0.097	2.16

9.2.2 Impact Experiments on Hyzod™ Polycarbonate

Hyzod polycarbonate is a transparent amorphous thermoplastic with a hard coated surface that resists abrasion providing high impact strength and high modulus of elasticity. HYZOD has impact strength 250 times stronger than float glass and 30 times stronger than acrylic.

A nearly 1.0 cm thick Hyzod plate is used to protect hatch windows from MMOD impacts. Hatch windows are made from tempered glass which is particularly sensitive to cracking from flaws induced by MMOD impacts. The Hyzod provides the required level of MMOD protection to the tempered glass used in the hatch. A series of hypervelocity impact tests generated data to develop ballistic limit equations and damage characteristics for the Hyzod material [9-1]. The test matrix and results are shown below in Table 9.2-2. None of the tests resulted in perforation of the Hyzod plate (0.95cm thick) and only one resulted in detached spall. Many of the others resulted in a bulge (attached spall) on the back of the Hyzod plate.

Table 9.2-2 NASA test results on Hyzod Polycarbonate

Test #	Projectile Diameter (mm)	Impact Angle	Actual Velocity (km/s)	Penetration Depth (mm)	Back of Plate	Witness Plate
1	1.00	0°	7.09	0.68	No deformation	Clean
2	1.25	0°	6.56	0.81	Bulge: 0.05mm high	Clean
3	1.42	0°	6.89	1.08	Bulge: 0.24mm high	Clean
4	1.59	0°	6.72	2.59	Bulge: 0.67mm high	Clean
5	2.01	0°	6.64	7.8	Detached Spall: 3.9mm diameter	Deposits on surface (5cm diameter)
6	1.80	0°	6.81	6.43	Bulge: 2mm high	Clean
7	2.19	45°	6.78	4.46	Bulge: 2.5mm high; incipient detached spall: crack around 270° circumference of bulge	Clean
8	2.99	45°	4.02	5.6	Bulge: 2.5mm high; incipient detached spall: crack around 180° circumference of bulge	Clean

9.2.3 Test Results

Semi-empirical equations have been developed by NASA from the experimental data for both fused silica and polycarbonate [9-4]. These equations are reported as well in the Protection Manual [9-5] and given below. Penetration depth (P, cm) in semi-infinite fused silica glass is determined from:

$$P = 0.53\ \rho^{0.5}\ d_l^{1.06}\ V_n^{(2/3)} \qquad (9.2\text{-}1)$$

$$d_l = (1.89\ P\ \rho^{-0.5}\ V_n^{-2/3})^{0.94} \qquad (9.2\text{-}2)$$

where d_l is the diameter or length (perpendicular to the target surface) of the projectile (cm), ρ is projectile density (g/cm^3) and V_n is the normal component of the projectile impact velocity (km/s), $V_n = V \cos\theta$ where θ is impact angle measured from the normal to the target.

Thickness of fused-silica glass to prevent incipient spall (cracks) at back of target:

$$t = 7P \qquad (9.2\text{-}3)$$

Thickness of fused-silica to prevent detached spall at back of target:

$$t = 4P \qquad (9.2\text{-}4)$$

Thickness of fused-silica to prevent complete perforation of target:

$$t = 2P \qquad (9.2\text{-}5)$$

Thickness to prevent complete shattering of target:

$$t = 0.14P\ V^{1.28} \qquad (9.2\text{-}6)$$

Diameter of crater, D_c, (cm) and diameter of projectile, d, (cm) parallel to target surface are given in the following equations:

$$D_c = 31\ d^{1.33}\ \rho^{0.44}\ V_n^{0.44} \qquad (9.2\text{-}7)$$

$$d = 0.076\ D_c^{0.75}\ \rho^{-0.33}\ V_n^{-0.33} \qquad (9.2\text{-}8)$$

Penetration depth in polycarbonate (Hyzod AR hard-coated), for P > 0.1 cm:

$$P = 3.0\ \rho^{1/3}\ d^{1.2}\ V^{2/3}\ \cos^{0.75}\theta - 1.38 \qquad (9.2\text{-}9)$$

where P is penetration depth (cm), d is projectile diameter (cm), ρ is projectile density (g/cm^3), V is impact velocity (km/s), and θ is the impact angle measured from the normal to the target.

9.3 Recommendation for MMOD risk reduction

The following recommendations are made to reduce the MMOD risk to transparent materials.

- A sacrificial debris pane should be used to protect fused silica glass that is used as a pressure pane and under load.
- Exterior shutters, made of one or more layers, should also be considered to protect the pressure panes of spacecraft windows [9-6].
- Polycarbonate windows will provide equivalent protection as fused silica glass but with one-half the mass [9-1].

9.4 References

[9-1] R.R. Burt and E.L. Christiansen, Hypervelocity impact testing of transparent spacecraft materials, *International Journal of Impact Engineering,* **Vol. 29**, pp. 153-166, 2003.

[9-2] R.R. Burt, E.L. Christiansen, J.H. Kerr, JSC-29549, Hypervelocity Impact Testing of Space Shuttle Windows, 2003.

[9-3] J.E. Miller and B.A. Davis, Multipurpose Crew Vehicle Window Testing and Ballistic Modeling, HVIT report JSC-66734, 2014.

[9-4] E.L. Christiansen, J. Arnold, A. Davis, J. Hyde, D. Lear, J.-C. Liou, F. Lyons, T. Prior, M. Ratliff, S. Ryan, F. Giovane, R. Corsaro, G. Studor, Handbook for Designing MMOD Protection, NASA TM-2009-214785, 2009.

[9-5] IADC Working Group 3, Protection Manual, Section 3.2.2 Windows and Glass, Ver.7, September 2014.

[9-6] R.R. Burt and E.L. Christiansen, An enhanced shutter to protect spacecraft windows from meteoroids and orbital debris, International Journal of Impact Engineering, Vol. 29, pp. 139-152, 2003.

10 Fluid Line

10.1 Impact Experiments and Numerical Simulations / EMI

In many spacecraft applications feed lines for pro¬pellant with a pressure in the order of 3 MPa are required (e. g. Fig. 10.1-1). These fuel pipes are critical components for spacecraft operation and have to be protected against hypervelocity impacts, because of the large amount of both pressure energy and chemical energy that is stored in the propellant.

The fuel pipes submitted to hypervelocity impact testing were of Ti3Al2.5V with an outer diameter of 6.35 mm (0.25") and a wall thickness of 0.41 mm (0.016"). They were tested in different configurations though only the one most representative for satellites is described here (Fig. 10.1-2). More tests can be found in [10-1].

The satellite structure wall consisted of a sandwich panel with 0.41 mm thick Al 2024 T3 face-sheets and a 35 mm thick Al honeycomb core (specification 2.0-3/16-07P-5056-MIL-C-7438G). Multi-Layer-Insulation (MLI) with an areal density of 0.447 kg/m^2 was placed in front of the sandwich panel. The MLI used consisted of one beta cloth 500GW layer (outside) and 9 layers Kapton with 9 separator layers of Dacron netting. The specification of the honeycomb sandwich panel with MLI is similar to that given in [10-2]. As was shown in [10-2], an aluminium sphere with a diameter of 1.2 mm (corresponding to a mass of 2.56 milligram) perforates this structure, when impacting at 7 km/s at perpendicular angle on it.

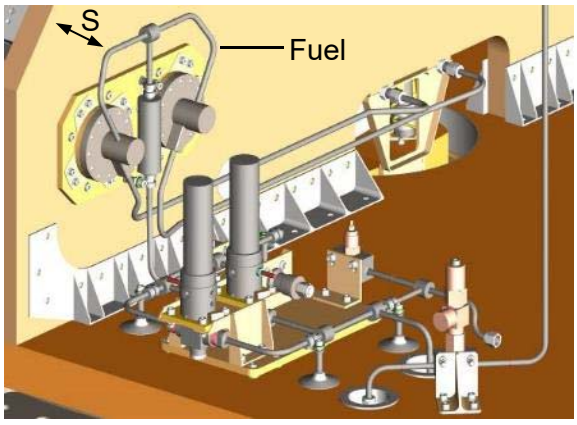

Fig. 10.1-1 Typical configuration of a fuel pipe routed inside a spacecraft with spacing S to the primary structure wall (courtesy OHB-System)

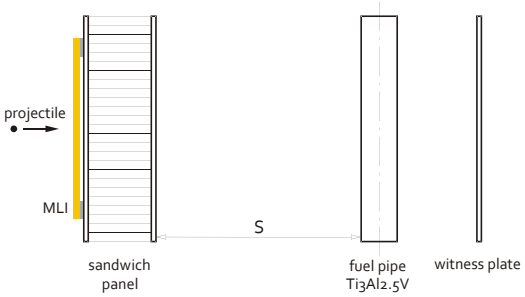

Fig. 10.1-2 Experimental configuration for fuel pipes shielded with Al-honeycomb sandwich panel structure walls and MLI placed on top. The spacing S amounts to either 50 or 100 mm

The stand-off between panel and pipe amounted to 50 mm and 100 mm in different tests. In the experiments, the propellant liquid was replaced by water. Nine hypervelocity impact tests at normal (0°) impact angle have been performed on the fuel pipes in the above configuration. In six experiments, the pipe has been filled with water and was pressurized with N2 gas. Experiments 4591 and 4592 have been performed with multiple pipes placed next to each other to increase the probability of fragment impact on the pipes. Table 10.1-1 lists the details, where S - stand-off between rear side of the sandwich panel and the surface of the pipe, v_0 - impact velocity, d_P - projectile diameter, m_P - projectile mass, P_0 - pressure inside the pipe before impact, ΔP_{Max} - maximum measured overpressure. Damage class refers to the damage in the fuel pipe. The damage class is given according to Dahl and Cour-Palais, 1991 [10-3] (C2: no perforation, but with attached spall(s) or rear surface deformation; C3: no perforation, but with detached spall(s); C4: perforation, all hole diameters < 2 mm; C5: penetration, applicable if any hole diameter ≥ 2 mm).

Table 10.1-1 Summary of fuel pipe impact tests and test results

EMI No.	S [mm]	v_0 [km/s]	d_P [mm]	P_0 [MPa]	ΔP_{Max} [MPa]	dam'ge class
93	50	3.5	2.5	3.0	—	C2
72	50	6.3	3.0	—	—	C2
4591	50	6.2	3.5	—	—	C4
4588	50	6.6	4.0	3.0	3.4	C2
4585	50	6.8	5.0	3.0	> 10	C5
4592	50	6.7	5.0	—	—	C4
4586	100	2.7	3.5	3.0	1.6	C2
4587	100	6.7	4.0	3.0	0.7	C4
4589	100	7.8	3.5	3.0	2.9	C2

At impact velocities of slightly above 6 km/s, the perforation threshold of the pipes is reached when aluminium projectiles with a diameter of between 3.0 mm and 3.5 mm impact. The pipe ruptures from impact of a projectile with diameter of 5 mm or above (Exp. 4585). Fig. 10.1-3 shows the optical shadowgraphs of the fragment cloud impacting the fuel pipe in Exp. 4585; the corresponding damage in the pipe and the witness plate that was placed behind the pipe can be seen in Fig. 10.1-4. From this damage it is obvious that fracture of the pipe was initiated by discrete fragment impact. Looking at the witness plate it is also obvious that large amounts of the fragment cloud's mass have not hit the pipe.

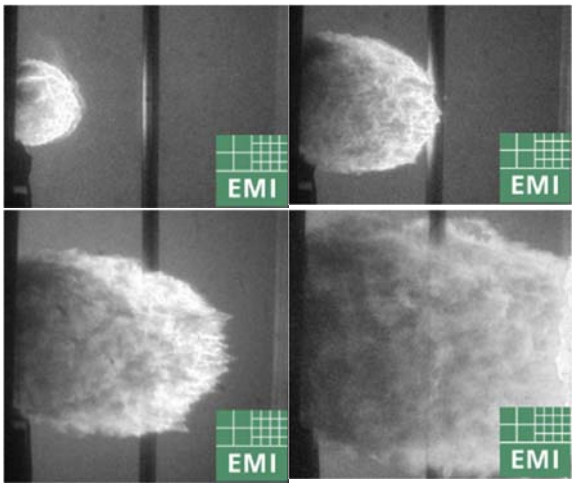

Fig. 10.1-3 Optical Shadowgraphs / Digital High-Speed Photographs of Exp 4585. Trigger times: 10, 15, 20, 30 µs with respect to impact on MLI.

Fig. 10.1-4 Fuel pipe (front and side view) and witness plate damage of Exp. 4585

Fragmentation of a projectile during hyper-velocity penetration of a complex target (such as the honeycomb sandwich panel) is a stochastic process. Thus the generated fragments may just miss the slender target in one test and hit it in the following test, generating large scatter in the data (cf. Exp. 4585 and 4592). Therefore the damages observed in the fuel pipes in most cases cannot be correlated in a straightforward, linear way with the corresponding impact parameters. Instead, a stochastic failure approach as presented in [10-1] is required.

During impact experiments on fuel pipes in the water large over¬pressures were measured. For example, in Exp. 4585, the measured overpressure was outside the recording range with an estimated peak pressure between 15 and 25 MPa.

Heat pipes, providing thermal control primarily for spacecraft electronic components, contain high-pressure NH3 and N2 (up to 4.5 MPa) depending on operational condi¬tions. Heat pipes are mainly routed within a sandwich panel (see Fig. 10.1-5). The sandwich panel provides support for the heat pipe, and acts as a radiator.

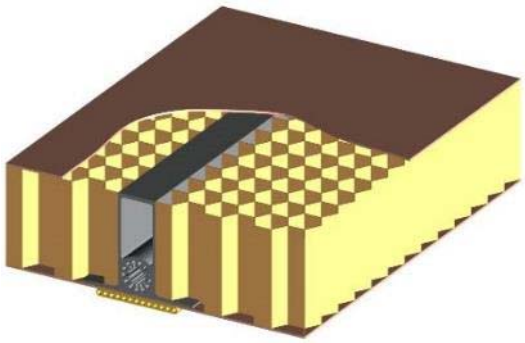

Fig. 10.1-5 HP routed inside a H/C SP

The integrated heat pipes submitted to hypervelocity tests were made of Al 6063 T5. The geometry is shown in Fig. 10.1-6. The pipes have an outer diameter of 10 mm, and a minimum wall thickness of between 0.82 and 0.95 mm. The pipes are embedded in an Al H/C SP with face sheets made of 1 mm thick Al 2024. The 20 mm thick SP H/C core specification is Hexcel 3/16-5056-0.0007. The mounting profile is made of Al 6063 T5, with a minimum thickness of 1.1 mm.

Seven impact tests at perpendicular projectile incidence (0°) on the configuration shown in Fig. 10.1-6 were performed. In six tests, the pipes were pres¬surized with N2 gas. Table 10.1-2 lists the heat pipes experiments, where D_0 - vertical offset between projectile impact location and heat pipe center. Damage is classified as either per¬foration or no perforation (of the pipe).

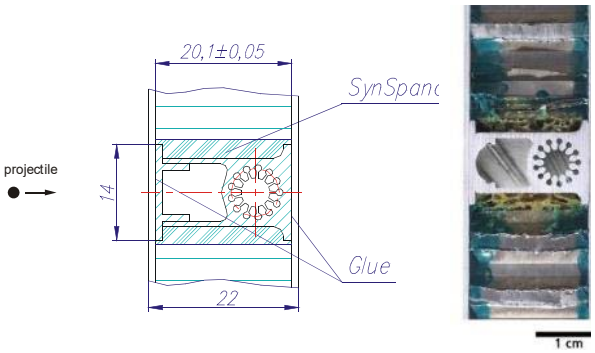

Fig. 10.1-6 Integrated heat pipe geometry

Table 10.1-2 Heat-pipe impact tests. Cfg.= configuration, NO =no offset, O = large offset, dam. = damage, no p. = no perforation, perf. = perforation

Exp	Cfg.	v_0 [km/s]	d_P [mm]	D_0 [mm]	P_0 [MPa]	ΔP_{Max} [MPa]	dam.
4603	NO	2.8	2.0	4	4.5	< 0.1	no p.
4607	NO	3.0	2.0	1	—	—	perf.
4605	NO	3.3	2.5	1	4.5	0.14	perf.
159	NO	5.4	1.1	2	4.5	—	no p.
4602	NO	6.7	1.5	1	4.5	< 0.1	perf.
4608	O	6.8	2.5	4	1.5	0.19	perf.
4609	O	6.8	2.5	14	4.5	< 0.1	no p.

In exp. 4603, the projectile did not penetrate the topmost heat pipe mounting profile, so the heat pipe itself was undamaged. In exp. 4607 the perforation hole is very small. As can be seen, at impact velocities of around 3 km/s, the perforation threshold diameter is about 2.0 mm, at impact velocities of around 6 km/s, the perforation threshold amounts to between 1.1 mm and 1.5 mm. The overpressures measured in the pressure gas are on the order of 10% or below, hence negligible. Overall, the vulnerability of the heat pipes is considered to be fairly low, because they are not affected if they are not hit directly, as can be seen from the last experiment that was performed with a large vertical offset (Table 10.1-2, Exp. 4609).

10.2 References

[10-1] Putzar, R.; Schäfer, F.; Romberg, O.; Lambert, M.: Vulnerability of shielded fuel pipes and heat pipes to hypervelocity impacts. Proc. 4th Europ. Conf. on Space Debris. Darmstadt, Germany, 2005. - ESA SP-587, pp 459-464

[10-2] M. Lambert, F. Schaefer, T. Geyer, Impact Damage on Sandwich Panels and Multi-Layer Insulation. *Int. J. Impact Engng. Vol. 26*, pp. 369 - 380, 2001

[10-3] Dahl, Kim V.; Cour-Palais, Burt G.: Standardization of impact damage classification and measurements for metallic targets, unpublished, 1991.

11 Examples of Risk Assessment Method

11.1 Vulnerability Assessment Method / University of Padova

11.1.1 Vulnerability assessment through debris cloud modelling

The method here presented can be used to assess the vulnerability of spacecraft hit by secondary debris clouds originated after perforation of the vehicle's hull. The key feature of this approach is that spacecraft configuration and internal equipment's layout are not limited to those evaluated by HVI testing, whose results are not automatically extrapolated outside the experimental configuration and range. This benefit could be significant in early design phases, when it is worth to explore solutions that might largely differ from historical ones. The idea behind the proposed impact risk assessment procedure is to evaluate the damage on internal components due to a new debris environment generated inside the spacecraft in consequence of perforations of the spacecraft walls (Fig. 11.1-1). Starting from the M/OD flux computed on each spacecraft surface by available models (e.g. MASTER or ORDEM), such new environment is given by the superposition of all secondary debris clouds resulting from primary impacts that perforate the spacecraft external surfaces.

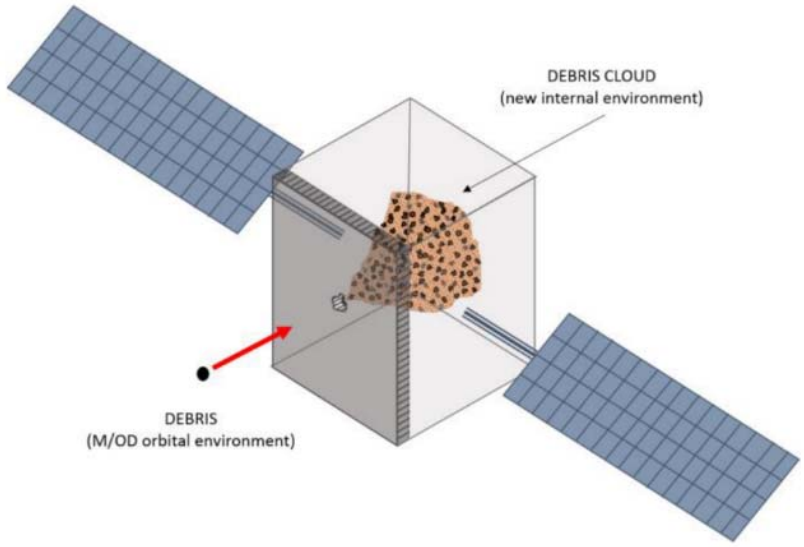

Fig. 11.1-1 Internal components vulnerability: procedure's concept

Secondary debris clouds are assumed to be independent and not-interacting, that is reasonable since the contemporary occurrence of two or more penetrating impacts on the same vehicle is unlikely.

Internal components are modelled as simple boxes/plates representing the equipment's cases, and damage equations for simple plates are used to predict the equipment failure (e.g. perforation of the case, or damage area on the case exceeding a certain threshold).

The core of the proposed procedure is the evaluation of damage due to debris clouds propagating inside the spacecraft. In this way:

- Impact risk assessment is based upon a general approach employing a true physical analysis of the interaction between debris and spacecraft components, through debris cloud modelling. Moreover, debris cloud models could be regularly improved as soon

as new test data become available, continuously increasing the accuracy/reliability to the method;

- Spacecraft structural configurations, geometries and internal equipment's layout are not limited to those evaluated by HVI testing, whose results cannot be easily and reliably extrapolated outside the experimental configuration and range. This is particularly limiting in early design phases, when it is worth to explore solutions that might largely differ from historical ones;
- Failure on internal components can be computed with reference to the damage on their cover faces using damage equations for plates, whose reliability is high because of the large databases on which they are based. Furthermore, failure criteria different from "perforation of the equipment case" can be adopted if necessary (e.g. damage area above a certain threshold, even below the ballistic limit);
- Mutual shadowing between components (and hence protecting effects related to different equipment layouts) can be accounted for automatically by propagating debris clouds inside the spacecraft.

The implementation of this approach requires the following elements:

- Suitable debris cloud models to predict the most important geometric properties of debris clouds (e.g. fragments' mass and velocity distribution);
- A specific tool for debris cloud propagation inside the spacecraft (e.g. based on raytracing)

In the method here reported, these elements are kept simple, i.e. debris clouds are described with analytical formulas, and particles ray-tracing is substituted by an original procedure which computes the "modified view factors" between the surfaces hit by debris and the internal equipment faces.

In summary, the core of the proposed procedure incorporates two principal elements, i.e. the debris cloud models (which generate the new debris environment inside the vehicle) and the algorithm to propagate the clouds towards whatever inner component. These two crucial elements are discussed in detail in Francesconi et al (2015) and Francesconi et al (2014), and are here briefly reported.

11.1.1.1 Debris cloud models

To apply the proposed procedure, debris cloud models have to provide three levels of information, i.e. a geometric description of the cloud, the velocity distribution and the mass distribution of the fragments in the cloud.

As regards geometry, the cloud is modelled with the superposition of two cones ("in-line" for heavy fragments and "dust" for all fragments), each of them is characterised by the axis direction (measured from the surface normal) and the spray angle around the axis (see Fig. 11.1-2). In the framework of this procedure, only to the in-line cone is considered. This cone contains the heaviest and fastest cloud fragments and thus represents the most dangerous part of it (with this assumption, slow but large spall fragments in the dust cloud are neglected). If only the in-line cloud is considered, the general form of a Debris Cloud Model (DCM) is a vector function of the following type (angles are defined as in Fig. 11.1-2):

$$(\xi, \alpha, m_d, v_d) = DCM(d_p, v_p, \theta, structure) \qquad (11.1\text{-}1)$$

Where ξ is the angle between the in-line cloud cone and the surface normal, α is the in-line cloud spread angle, m_d and v_d are respectively the fragments mass and velocity distribution within the in-line cloud; d_p, v_p and θ are the primary debris diameter, velocity and impact angle (measured from the surface normal), *structure* is a set of parameters describing the material and geometry of the spacecraft external surface subjected to the primary impact. A complete list of the symbols is provided in Table 11.1-1 (not limited to those introduced till now).

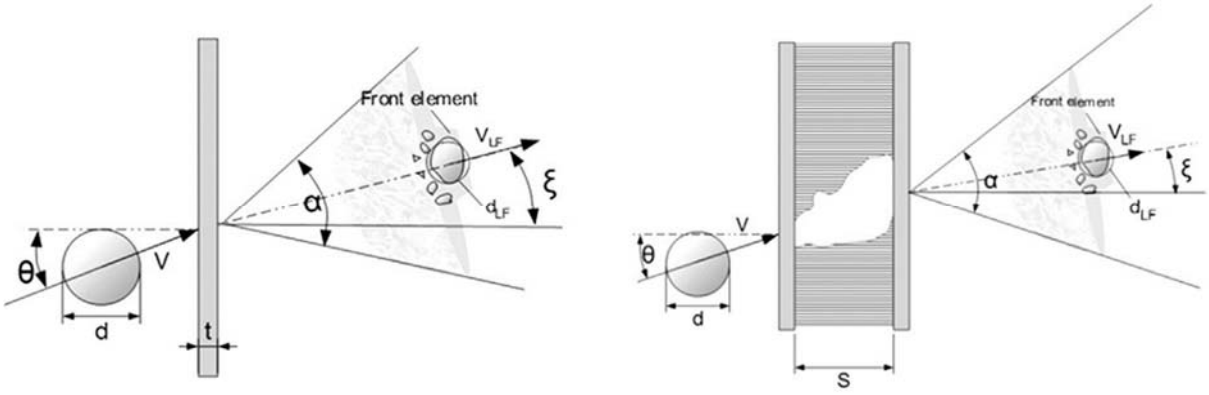

Fig. 11.1-2 In-line debris cloud geometric model for simple plates (left) and sandwich panels (right); θ is the impact angle, ξ is the angle between the in-line cloud cone and the surface normal, α is the in-line cloud spread angle (Francesconi et al, 2015)

Any debris cloud model can be implemented in the proposed procedure, provided that it is given in the form of Eq. 11.1-1: in this document, two models are proposed, as described in the following sub-sections.

Debris cloud models for simple plates

The simple plate model for largest fragment was derived by fitting the experimental results of 32 impact tests reported by Piekutowski (1996). Such data refer to normal (θ=0°) impacts on aluminium-alloy plates, and hence the model generalization to oblique impacts and/or target materials different from aluminium requires validation. A preliminary verification was done as regards the impact angle only, since too few debris cloud data are available for composite material. The model is described by the formulas in Eq. 11.1-2 (a, b, c, d) and employs the coefficients in Table 11.1-2.

$$\xi = \theta \tag{11.1-2a}$$

$$\alpha = \begin{cases} N.A. & \text{if } d < d_{BL} \\ c_1 \left[\max\left(0, v\cos\theta - v_{FR}\right)\right]^{c_2} \left(\frac{\rho t}{d}\right)^{c_3} & \text{if } d \geq d_{BL} \end{cases} \tag{11.1-2b}$$

$$\frac{d_{LF}}{d} = \begin{cases} N.A. & if\ d\ < d_{BL} \\ \min\left\{1, \max\left[0,\ 1 - b\left(v\cos\theta - v_{FR}\right)\right]\right\} & if\ d\ \geq d_{BL} \end{cases} \qquad (11.1\text{-}2c)$$

$$\frac{v_{LF}}{v} = \begin{cases} N.A. & if\ \ d < d_{BL} \\ \max\left\{0, 1 - \left[\frac{t}{d}\cdot\left(\frac{K_{BL}}{v\ \cos\theta}\right)^{2/3}\right]^{a}\right\} & if\ \ d\ \geq d_{BL} \end{cases} \qquad (11.1\text{-}2d)$$

$$d_{BL} = t\cdot\left(\frac{K_{BL}}{v\cos\theta}\right)^{2/3} \qquad (11.1\text{-}3)$$

$$v_{FR} = K_{F1}\left(\frac{\rho t}{d}\right)^{K_{F2}} \qquad (11.1\text{-}4)$$

Furthermore, the total mass of the cloud m_{tot} (fully fragmented debris plus a portion of target material ejected downrange) is given by Eq. 11.1-5:

$$m_{tot} = m\left[1 + K_{t1}\left(\frac{t}{d}\right)^{K_{t2}}\right] \qquad (11.1\text{-}5)$$

The logic and assumptions behind the derivation of Eqs. 11.1-2, 11.1-3, 11.1-4 and 11.1-5 are shortly described in the following points.

- In Eq. 11.1-3, the ballistic limit d_{BL} is calculated using the formula proposed by Cour-Palais (1969) for ductile target materials (in this case K_{BL}=1). The same equation was extended to CFRP (with K_{BL}=0.60) using test results reported by Francesconi et al (2012).
- Eq. 11.1-4 defines a threshold velocity v_{FR} below which no fragmentation occurs (and hence d_{LF}=d); v_{FR} was assumed to be dependent on t/d and Eq. 11.1-4 was obtained by fitting test data by Piekutowski (1996) regarding the size/mass of largest fragments resulting from different HVI experiments on simple Al-alloy plates.
- As regards the cloud geometry, Eq. 11.1-2a presupposes that the in-line cone deviation ξ from the target normal vector is equal to the impact angle θ. Moreover, the cone spread angle α is described by Eq. 11.1-2b, in which the angle dependence from both $v\cos\theta$-v_{FR} and t/d is included, as results from the best fit of available data from Piekutowski (1996). The equation is also corrected to force α=0 at impact speed lower than the fragmentation threshold v_{FR}.
- The equivalent diameter d_{LF} of the largest fragment is given by Eq. 11.1-2c: d_{LF} is lower than or equal to that of the original debris and, for any given value of d, it is assumed to have a linear decreasing dependence from $v\cos\theta$-v_{FR}. Eq. 11.1-2c is also

limited at very high impact speed to avoid negative values of d_{LF}. The value of 0.2 for the b parameter in Eq. 11.1-2c (see Table 11.1-2) was obtained by fitting test data from Piekutowski (1996). Note that such value of b implies that the incoming debris is fully fragmented if $v\cos\theta > v_{FR} + 5$ km/s.

- Similar considerations are behind the derivation of Eq. 11.1-2d, which predicts the largest fragment velocity v_{LF}; v_{LF} is lower than or equal to the original debris velocity. Following experimental evidences (Piekutowski, 1996), v_{LF} decrease is assumed to have a power-law dependence from t/d, and Eq. 11.1-2d features this trend with the additional condition of having $v_{LF}=0$ at the ballistic limit. The exponent in the power law was determined by fitting test data from Piekutowski (1996) for Al alloys and Francesconi et al (2012) for CFRP.
- Once fully fragmented ($d_{LF}=0$), the cloud total mass m_{tot} is estimated as the sum of the mass of the original debris plus a portion of target material removed in consequence of perforation and then projected downrange. Following this assumption, K_{t1} in Eq. 11.1-5 was obtained analytically by geometric considerations and then verified by a multi-variable fit of experimental data. On the other hand, K_{t2} was derived by reverse fitting the Ballistic Limit Equation for Whipple Shields (Christiansen, 1993), making our debris cloud model capable of predicting the failure of Whipple Shields for impact speed > 7 km/s.

Table 11.1-1 Definition of symbols and corresponding units (units are arbitrary for those parameters which appear in ratios in the equations).

Symbols and units	
θ	Impact angle(°)
ξ	In-line cone deviation angle (°)
α	In-line cone spray angle (°)
d	Projectile diameter (arbitrary unit)
d_{BL}	Debris diameter at ballistic limit (same unit as d)
d_{LF}	Largest fragment diameter (same unit as d)
v	Projectile velocity (km/s)
v_{FR}	Threshold velocity for debris fragmentation(km/s)
v_{LR}	Largest fragment velocity (km/s)
ρ	Mass density of the target material (g/(same unit as d)^3)
t	Target thickness (same unit as d)
t_{ECP}	Equipment cover plate thickness (cm)
m	Debris mass (g)
m_{TOT}	Cloud total mass (g)
m_{LF}	Largest fragment mass (g)
r	Honeycomb cell wall thickness (cm)
S	Honeycomb core thickness, face-sheets excluded (cm)
q	Honeycomb cell equivalent diameter (cm)
A_{DC}	Cover plate surface portion hit by the debris cloud (cm^2)
$E_{k,LF}$	Largest fragment kinetic energy (kJ)
$E_{k,tot}$	Total kinetic energy (kJ)
$E_{k,crit}$	Critical kinetic energy (kJ)

Table 11.1-2 Coefficients for simple plates models.
**No experimental data available for CFRP: values for Al alloys must be used with care*

	Al alloys	CFRP
K_{BL}	1.00	0.60
K_{F1}	1.41	*
K_{F2}	-0.41	*
K_{t1}	1.50	*
K_{t2}	4.56	*
a	0.83	0.19
b	0.20	*
c_1	15.89	*
c_2	0.51	*
c_3	0.15	*

Debris cloud models for sandwich panels

The model for sandwich panels is a two-step application of the model for simple plates, with the addition of a suitable corrective factor to account for the presence of the honeycomb core. More precisely, in order to calculate the debris cloud resulting from perforation of the sandwich panel, Eqs. 11.1-2, 11.1-3, 11.1-4 and 11.1-5 are applied to the panel rear skin, assuming that such back face-sheet is hit by a single piece of debris with size and velocity specified in Eqs. 11.1-6 and 11.1-7a:

$$d = d_{LF,front} \cdot K_{HC} \tag{11.1-6}$$

$$v = v_{LF,front} \cdot K_{HC} \tag{11.1-7a}$$

In the above formulas, $d_{LF,front}$ and $v_{LF,front}$ are the diameter and velocity of the largest fragment emerging after impact with the front face-sheet; K_{HC} is a corrective factor (always lower than one) accounting for the honeycomb core "filtering effect" (which is supposed to be the same for the size as well as the speed of the fragment), and finally d and v are the diameter and velocity of the largest secondary debris hitting the panel rear face-sheet. K_{HC} is related to the multiple impacts of the largest fragment on the honeycomb cell walls and was therefore related to the honeycomb cells properties (equivalent diameter *q* and wall thickness *r*; *q* is the diameter of the circle circumscribing a hexagonal honeycomb cell), the honeycomb core thickness (without face-sheets) *S* and the impact angle θ. Following these assumptions, KHC was obtained by reverse fitting, at oblique impact angle, the Ballistic Limit Equation for sandwich panels used by Sibeaud et al (2008), where *r*, *S* and *q* are measured in cm (see Eq. 11.1-7b). Note that Eq.11.1-7b gives K_{HC}=1 if θ=0° (i.e. a honeycomb sandwich panel behaves as a Whipple Shield at normal impact incidence, with no consideration to "channeling" effects), but is not to be used if no honeycomb core is present, where clearly K_{HC} must be equal to 1.

$$K_{HC} = \left[\frac{\cos\theta}{\left(1 + 1.345 \left(\frac{rS}{q}\right)^{0.455} \tan\theta\right)} \right]^{0.6} \qquad (11.1\text{-}7b)$$

Comparison with SRL equations

The reliability of the proposed debris cloud model for sandwich panels was finally assessed with reference to triple wall structures (see Fig. 11.1-2). In particular, the debris cloud emerging from the sandwich rear skin was applied to the third wall with the objective of predicting the third plate perforation, i.e. the ballistic limit of the whole triple wall system. To this aim, the model predictions were compared to few experimental data collected in the framework of the EU contract P2ROTECT (www.p2rotect-fp7.eu), and to the SRL ballistic limit equations for triple wall structures.

The experimental results here used as benchmark refer to two different sandwich panels with aluminium face-sheets, each of them was subjected to 5 hypervelocity impact tests with aluminium projectiles at speed from 6 to 7 km/s and impact angle equal to 0° and 45°.

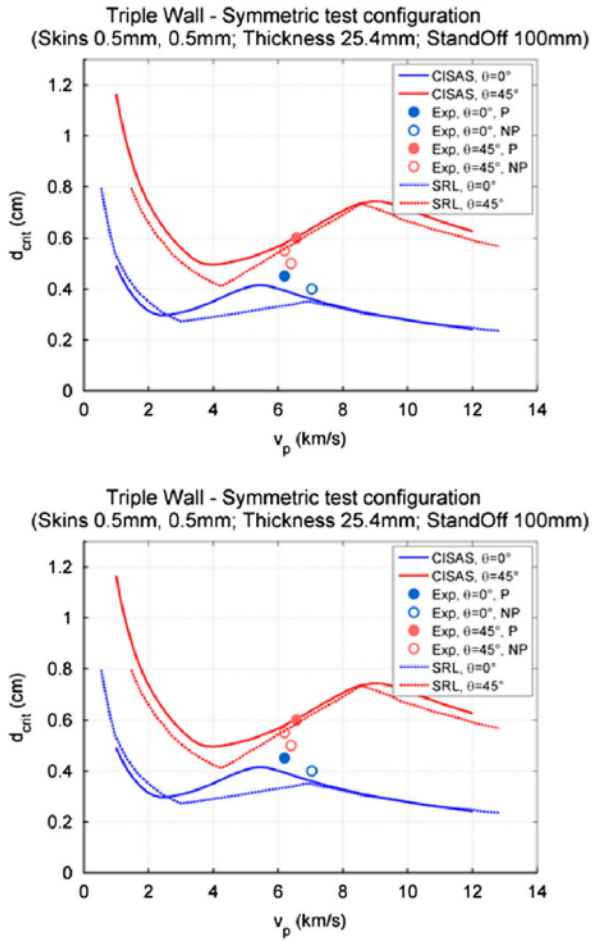

Fig. 11.1-3 Triple wall structure ballistic limit for the symmetric (left) and asymmetric (right) honeycomb configuration: difference between CISAS debris cloud model ad SRL equation.

Fig. 11.1-3 shows the comparison between test result, predictions obtained with the debris cloud model (CISAS, continuous lines) and the SRL equations (dotted lines). It is visible that the CISAS and SRL curves are very similar, even though the transition points predicted by the debris cloud model for θ=0° are at lower velocity compared to SRL (in particular the curves maxima are at ~5 km/s instead of 7 km/s). This discrepancy is related to the fact that maxima of SRL are a-priori fixed to 7 km/s, while the CISAS model calculates this velocity value automatically. Considering that the impact dataset currently available for triple wall structures is still much limited compared to those of other shielding configurations (e.g. Whipple Shields), it seems reasonable that such an inconsistency deserves further investigation through impact experiments. Nevertheless, it is evident that the proposed debris cloud model is very effective in representing the test results, and the differences with the SRL equations remain small at every velocity regime (the maximum difference never exceeds 25% and occurs between 4 and 5 km/s for both configurations).

11.1.1.2 Cloud propagation algorithm: Modified View Factors (MVF)

In the proposed procedure, there is the need of calculating what part of secondary debris clouds is intercepted by each spacecraft internal component. Such part depends on the internal equipment geometry and layout, and also on the debris cloud axis orientation and spread angle. These two pieces of information are combined together using the so-called Modified View Factors (MVF).

By definition, the i-th Modified View Factor from the spacecraft external surface “ext” to the k-th internal face is the fraction $MVF(i)_{ext \rightarrow k}$ of the i-th debris cloud originated from “ext” which directly impinges on the k-th face.

In principle, MVF could be calculated with a dedicated anisotropic ray-tracing algorithm, which fires rays only within the debris cloud cone. However, in order to limit the algorithm complexity to a “simplified” framework, an original analytic procedure has been developed to avoid ray-tracing (Fig. 11.1-4). This simplified procedure employs Geometric View Factors (GVF) used for thermal calculations and then applies to them a correction which accounts for the debris cloud axis orientation and spread angle. This correction is requested since GVF are obtained for surfaces which emit rays along every direction in the half space containing the target, and hence they are not adequate to simulate the flux of secondary fragments produced by HVI, which is contained in the debris cloud cone.

<u>Modified View Factors calculation and shadowing algorithm</u>

The Modified View Factor (MVF) approach represents a way to evaluate the fraction of a debris cloud which is intercepted by any target surface. Since the accurate calculation of such fraction is a computationally complex task, the algorithm here described provides an approximate but fast analytic tool for MVF evaluation. The algorithm (Francesconi et al, 2014) consists on three main steps (Fig. 11.1-4):

- Evaluation of the Geometric View Factor between the spacecraft external (emitting) surface and the selected internal component’s face (target surface). The Geometric View Factor (GVF) is an important quantity widely used in optics and in thermo-physics for the evaluation of radiation heat fluxes between distinct surfaces. In physical terms, the GVF is the portion of the flux emanated by surface 1 which directly reaches surface 2, if surface 1 emits in an isotropic and uniform manner.

- Representation of the target as a fictitious surface which delimits an equivalent cone covering the same solid angle as the target surface. Consider the projection of the target surface on the unit sphere with origin on the geometrical centre of the emitting surface; the equivalent cone approximates this projection with a circle on the unit sphere (Fig. 11.1-4 b).
- Calculation of the MVF as the intersection A_{int} between the circles resulting from the projection of the GVF equivalent cone (circle 1) and the debris cloud cone (circle 2) on the unit sphere, normalized by the area of circle 2 (Fig. 11.1-4 d).

The MVF method is valid for two surfaces which are in direct view each other. If other surfaces are interposed between them, there may be a partial or total shadowing, which reduces the MVF accordingly. To take into account this possibility, a special shadowing algorithm has been developed based on a “second-level application” (to MVF instead of GVF) of the same simplified procedure already used for MVF calculation: the shadowing algorithm provides suitable corrections to MVF that were earlier calculated (with no consideration to shadowing) between “stand-alone” couples of surfaces. Further details on the shadowing algorithm are reported in (Francesconi et al, 2014).

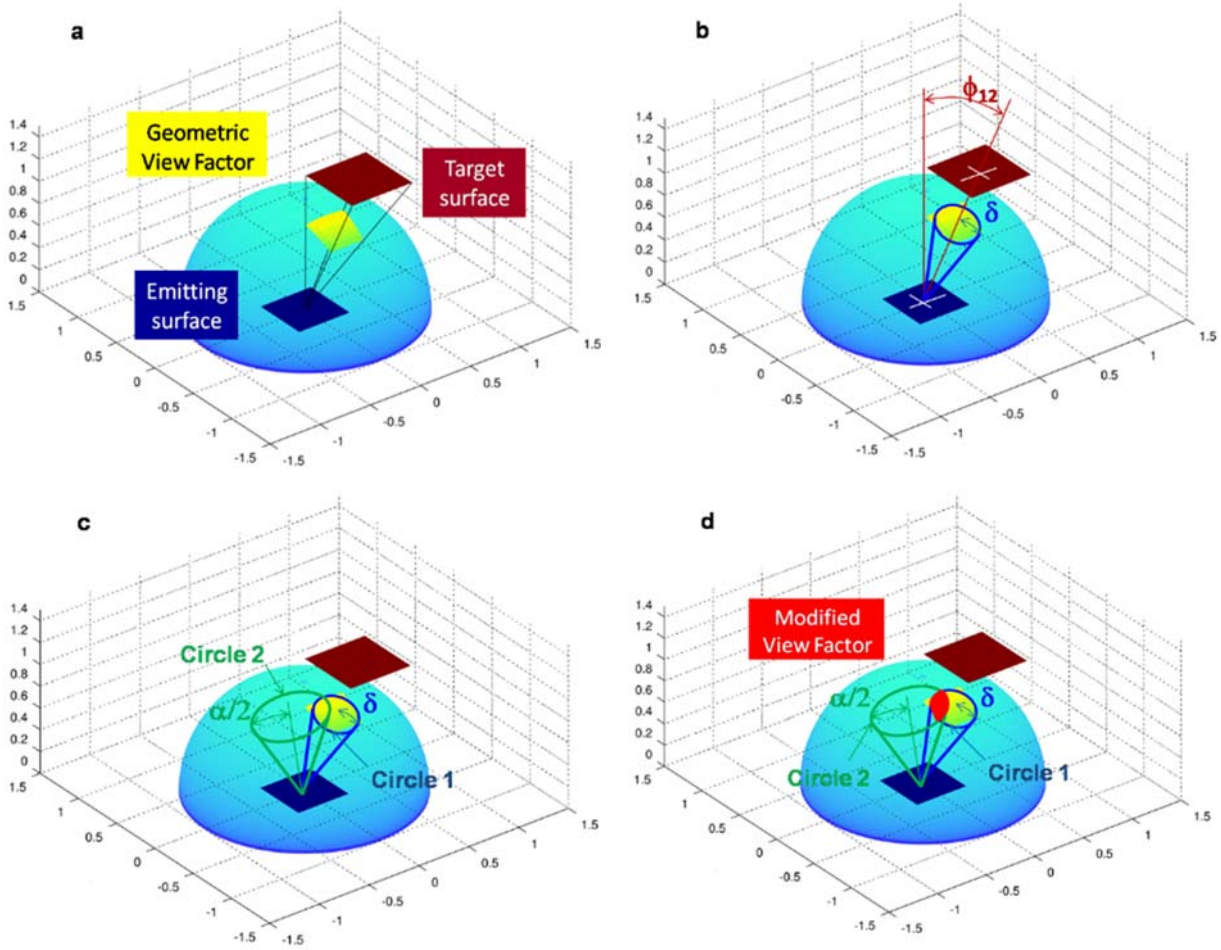

Fig. 11.1-4 Main steps of the simplified algorithm for MVF calculation

Validation results showed that the MVF simplified algorithm is fairly accurate (mean error of 1.5%) when compared to a common ray-tracing procedure, except for rectangular targets

with high aspect ratio (mean error up to 23%). However, in this case MVF are always overestimated and hence the algorithm is conservative. It can be therefore concluded that the simplified MVF approach provides highly accurate results in most practical situations, being a valid alternative to ray-tracing in early design phases.

11.1.1.3 Risk assessment procedure

The main steps of the Risk Assessment procedure outlined in the introductive section are detailed hereafter. Apart from the debris cloud modelling and propagation using MVF, the Risk Assessment procedure is standard from the conceptual point of view and involves the following seven consequential steps:

a. Creation and reading of an input file containing 3D geometric information on the spacecraft external and internal components, materials information and flags for surfaces "activation" (i.e. inclusion in the set of faces for which the procedure is applied). As regards geometry, a main body reference frame is selected (e.g. the one in which the environmental meteoroid and debris flux is provided) and all the spacecraft active faces are located in this reference frame through the Cartesian coordinates of their geometric centres and three rotations around the coordinate axes; the unit normal to each face is also calculated. Furthermore, all the applicable transformation matrixes are calculated to pass from the main reference frame to local reference frames on the active surfaces.
b. Reading the STENVI meteoroids and debris flux files and creation of the Impact Flux vector for each external surface. Considering the whole spacecraft, the Impact Flux is a matrix *IF(i,j)*, where the first index refers to the *i*-th class in which the flux is split (providing information on the number of impacts of debris in given size, velocity, impact elevation and impact azimuth bins) and the second index refers to the *j*-th external surface.
c. Computation of the portion of the Impact Flux which perforates the spacecraft hull and penetrates inside the vehicle. This is done by applying the modified Christiansen's Ballistic Limit Equation for sandwich panels (Sibeaud et al, 2008), using the impact angle determined with エラー! 参照元が見つかりません。. 11.1-2. The Penetration Flux *PF(i,j)* is therefore a subset of the Impact Flux, including only the classes whose combination of impact parameters results in the external surface's perforation.
d. Debris cloud modelling for each element of the *PF(i,j)* matrix. This step has been discussed in detail in the dedicated sub-section.
e. Calculation of the Modified View Factors $MVF(i,j)_k$ towards all the active internal faces (denoted by index *k*), for each element of the *PF(i,j)* matrix. This step has been discussed in detail in dedicated sub-section.
f. Calculation of the fraction $PF(i,j)_k$ of the penetration flux which directly hits the *k*-th active face:

$$PF(i,j)_k = PF(i,j) \cdot MVF(i,j)_k \qquad (11.1\text{-}8)$$

g. Evaluation of the damage Δ(i,j)k on all the internal active faces, resulting from each element of PF(i,j)k. Internal faces are assumed to be simple plates of given thickness tk. Damage can be related to different mechanisms (e.g. cratering, perforation, etc.),

provided that a suitable damage equation is available for the selected damage definition. If we assume that damage corresponds to internal face perforation, the following equation can be used:

$$P_{\infty} = k_{\infty} \rho^{1/6} M^{0.352} \left(v \cos \vartheta \right)^{2/3} \qquad (11.1\text{-}9)$$

Where P_{∞} is the depth of the crater on the plate, ρ is the debris density in g/cm3, M is the debris cloud mass distribution in g, v is the debris cloud velocity distribution in km/s, k_{∞}=0.42 for Aluminium alloys and k_{∞}=0.25 for steel. For each element of $PF(i,j)_k$, the perforation of the k-th internal face is reached if $P_{\infty k} = t_k/2$ and, in this case, the probability of perforation is equal to $PF^*(i,j)_k$, where the "star" indicates that $PF(i,j)_k$ has to be limited to the classes which cause $P_{\infty k}$ to exceed $t_k/2$. Hence, the cumulative perforation probability for the k-th internal face is:

$$\Delta_k = \sum_j \sum_i PF^* \left(i, j \right)_k \qquad (11.1\text{-}10)$$

11.2 Risk Assessment Tool / EMI

11.2.1 PIRAT

The Particle Impact Risk and Vulnerability Assessment Tool (PIRAT) was specifically developed to assess the effects on equipment within the interior of typical satellite structure. To this purpose, a dedicated damage equation, the Schäfer-Ryan-Lambert (SRL) BLE was developed during an ESA study [11-7][11-8]. The SRL ballistic limit equation computes the critical diameter necessary to produce a component failure (via penetration or detached spall from the inner side of the component cover plate) based on the material characteristics and spacing of the structure panel and the equipment cover plate, as well as the characteristics of the impacting particle.

The Particle and Impact Risk and vulnerability Assessment Tool PIRAT [11-9] uses the debris fluxes from either MASTER 2009 or ORDEM 3.0 to predict the localized particle fluxes encountered by the spacecraft. Afterwards, the effects of the individual particle fluxes are evaluated deterministically. The areas of components that are susceptible to particle impacts are determined using a geometric projected area approach. In this way, the exposed areas of components are calculated based on the relative impact trajectories of individual debris particles with respect to the S/C orientation, considering shadowing effects of internal S/C equipment. The SRL equation (and other BLEs) is used to assess physical damage effects and the aggregate time-dependent vulnerability of each component is determined using Poisson statistics. Using a Boolean logic model of the S/C functional architecture, the associated functional degradation resulting from component failures can be determined.

As an example, [11-10], in Fig. 11.2-1, the incident flux on external components and structure panels is shown on a face-by-face basis on a satellite on a linear scale (left and center). The failure probability for each of the analyzed satellite equipment during the mission duration is shown on the right image.

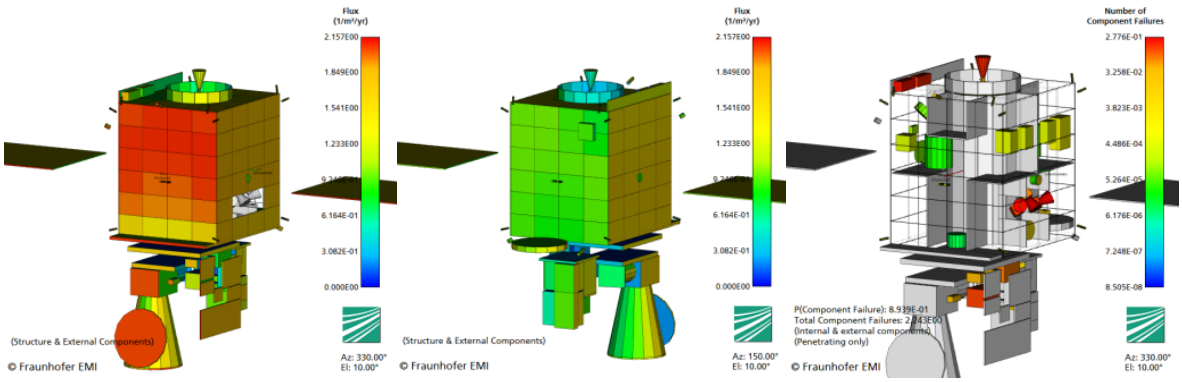

Fig. 11.2-1 Risk and vulnerability assessment of a generic LEO satellite computed with MASTER 2009

11.3 References

[11-1] Christiansen E.L (1993). Design and performance equations for advanced meteoroid and debris shields. Int. J. Impact Engng 14, pp.145-156

[11-2] Cour-Palais B (1969). Meteoroid Protection by Multiwall Structures, AIAA Paper No. 69-372

[11-3] Francesconi A, Giacomuzzo C, Feltrin F, Antonello A, Savioli L (2015). An engineering model to describe fragments clouds propagating inside spacecraft in consequence of space debris impact on sandwich panel structures. Acta Astronautica 116, 222-228.

[11-4] Francesconi A, Rondini D, Chanteperdrix G, Giacomuzzo C, Olivieri L, Theroude C (2014). An analytical method for the propagation towards internal components of debris clouds originated by space debris impacts on spacecraft walls. In Proc: 65th IAC Congress, Toronto, Canada.

[11-5] Piekutowski A.J. (1996) Formation and description of debris clouds produced by hypervelocity impact. NASA contractor report 4707

[11-6] Sibeaud, J-M., L. Thamie, C. Puillet. (2008). Hypervelocity impact on honeycomb target structures: Experiments and modeling. International Journal of Impact Engineering 35.12: 1799-1807.

[11-7] Schäfer, F. K., Ryan S., Lambert M., and Putzar R. (2008). Ballistic limit equation for equipment placed behind satellite structure walls. International Journal of Impact Engineering 35, 1784–1791.

[11-8] Schäfer F., Putzar R., and Lambert M. (2008). Vulnerability of Satellite Equipment to Hypervelocity Impacts. 59th International Astronautical Congress. Glasgow, Scotland, September 29-October 3, 2008.

[11-9] Welty, N., Rudolph, M., Schäfer, F., Apeldoorn J., and Janovsky, R. (2013). Computational methodology to predict satellite system-level effects from impacts of untrackable space debris, Acta Astronautica, Volume 88, Pages 35–43

[11-10] Kempf, S., Schäfer, F., Rudolph, M., Welty, N., Donath, T., Destefanis, R., Grassi, L., Janovsky, R., Evans, L., Winterboer, A. (2013). Risk and vulnerability analysis of satellites due to MM/SD with PIRAT. 6th European Conference on Space Debris, Darmstadt.